MEASUREMENT OF THE DOUBLE SPIN ASYMMETRY IN π^- ELECTROPRODUCTION WITH CLAS

by

Mehmet Bektasoglu
M.S. Old Dominion University (1997)
B.S. Yildiz Technical University, Istanbul, Turkey (1993)

A Dissertation Submitted to the Faculty of
Old Dominion University in Partial Fulfillment of the
Requirement for the Degree of

DOCTOR OF PHILOSOPHY

PHYSICS

OLD DOMINION UNIVERSITY
December 2002

Approved by:

Gail E. Dodge (Director)

Oktay Baysal

Sebastian E. Kuhn

Anatoly Radyushkin

Charles I. Sukenik

ABSTRACT

MEASUREMENT OF THE DOUBLE SPIN ASYMMETRY IN π^- ELECTROPRODUCTION WITH CLAS

Mehmet Bektasoglu
Old Dominion University, 2003
Director: Dr. Gail E. Dodge

The double spin asymmetry σ_{et}/σ_0 has been measured in π^- electro–production using a polarized electron beam and a polarized ND_3 target, and using the Cebaf Large Acceptance Spectrometer (CLAS). The electron beam was polarized using a GaAs–cathode and the target was polarized via Dynamic Nuclear Polarization. The beam polarization was around 70% and the target polarization was between 10 and 20%. The data at 2.5 GeV beam energy and two different magnetic field settings (2250 A and -1500 A) were collected in Hall B at Jefferson Lab, in the Fall of 1998. The $e\pi^-$ channel was selected using the missing mass technique and applying a cut around the proton peak (0.78 GeV^2 $< MM^2 <$ 0.95 GeV^2). The asymmetry $(A_1+\eta A_2)/(1+\epsilon R)$, where both A_1 and A_2 depend on θ^*, has been extracted as a function of the invariant mass W for two Q^2 (four–momentum–transfer–squared) bins (0.08 GeV^2 $< Q^2 <$ 0.4 GeV^2 and 0.4 GeV^2 $< Q^2 <$ 1.2 GeV^2). The results were integrated over the angular acceptance of the channel as well as for a narrower range in θ^* ($0.17 < \cos\theta^* < 1$). The data have been compared to two phenomenological models, MAID and AO.

TABLE OF CONTENTS

LIST OF TABLES

LIST OF FIGURES

CHAPTER 1

INTRODUCTION

1.1 STRONG FORCE

By the end of the 19th century, physicists knew that all matter was made of composite systems, atoms. An atom is composed of a dense nucleus surrounded by an electron cloud. The discovery of the neutron in 1932 by Chadwick proved that nuclei are also composite systems, made of protons and neutrons (nucleons). Nucleons are the lowest mass objects in the particle group called *baryons*, such as Δ, Σ and Ω. Now the question *what holds the nucleus together?* arises. Protons are positively charged particles. Therefore, they should strongly repel each other as they get closer, but instead they stay packed together. This clearly tells us that there must be some other force that is more powerful than the force of electrical repulsion among the protons to keep those elementary particles, the nucleons, together. It is named the *strong* or *nuclear force.* Unlike the electromagnetic force, which is longe-range and extends throughout all space (varying as $1/r^2$), the *strong force* goes to zero with a range of about 1.4 fermi.

1.2 THE DISCOVERY OF PIONS

In the beginning of the 1900's it was known that the electromagnetic force between two electrically charged particles is produced by the exchange of virtual photons. The long-range of this force requires that the exchange field particles (photons) have zero mass. Similarly, in order to describe the nature of the short-range *strong force* mentioned above in terms of the exchange of virtual particles, the Japanese physicist H. Yukawa [1] postulated the existence of the pion in 1935. He also predicted that those nuclear exchange particles would have a mass nearly 300 times that of the electron, or about one sixth the mass of a proton.

A virtual pion that is being exchanged between two nucleons cannot be observed, but real ones can be created and observed if enough energy (several hundred MeV) is given to the nuclear system. Pions are the lightest of the particle group called *mesons* (π, η, ρ, ω etc.), which, together with the baryons mentioned above, are called *hadrons.*

This dissertation follows the style of *The Physical Review*

TABLE I: Some properties of the pions.

Particle	Charge	Isospin	I_z	J^P	Mass (GeV)
π^0	0	1	0	0^{-1}	0.135
π^+	$+1$	1	$+1$	0^{-1}	0.140
π^-	-1	1	-1	0^{-1}	0.140

Pions are found in three different charge states: π^+, π^- and π^0. Charged pions (π^+ and π^-) with the same properties as the predicted nuclear exchange particles were first identified in 1947 [2]. The uncharged pion (π^0) was detected three years later. Some properties of pions are given in Table I.

One of the major motivations in both theoretical and experimental strong interaction physics is to obtain information on the structure of the nucleon and other strongly interacting particles (the hadrons). Gell-Mann and Zweig, in 1964, independently proposed that hadrons are in fact composed of even more elementary constituents, which were called *quarks* by Gell-Mann [3]. Every baryon (*anti*-baryon) is composed of three quarks (*anti*–quarks). Mesons, on the other hand, are made of a quark–antiquark pair. π^+, π^-, and π^0, for instance, are composed of $up(u)$–$antidown(\bar{d})$, $down(d)$–$antiup(\bar{u})$, and a linear combination of $u\bar{u}$ and $d\bar{d}$ quarks, respectively.

Some of the baryons, for instance Δ^{++} and Ω^-, seemed to be inconsistent with the Pauli exclusion principle. This principle originally stated that no two electrons can occupy the same state, but it was realized later that the same principle can be applied to all particles with half-integer spin. In order to solve the dilemma mentioned above, O. W. Greenberg [4] suggested that quarks not only come in three *flavors* up (u), down (d) and *strange* (s)[1] , but each comes in three *colors* (red, green and blue)[2], as well. Quarks are bound into hadrons via the strong interaction, in which the massless *gluons* are the exchange particles that couple to the color charge. The underlying quark-gluon structure of the pion and the proton is described by a fundamental field theory called *quantum chromodynamics* (QCD).

[1] We now know that there are 6 flavors of quarks; up (u), down (d), strange (s), *charm* (c), *bottom* (b) and *top* (t).

[2] The color of a quark, namely its redness, greenness or blueness, has no connection with the physical color of the quark. It only denotes a new property that the quark possesses.

1.3 PION ELECTRO–PRODUCTION

Scattering experiments are an important tool to study the structure of the nucleon or nucleus. In these experiments the object to be studied (the *target*) is bombarded with a beam of particles. If the collision is elastic the target, for instance the nucleon, remains in its ground state and only its kinetic energy changes. If the collision is inelastic, on the other hand, the nucleon is excited into higher energy states by part of the kinetic energy transferred from the beam particle to the nucleon. These excited states of the nucleon are known as the nucleon *resonances*, the $\Delta(1232)$ being the most prominent one.

Pion electro–production is the inelastic collision of an electron with a nucleon (or a nucleus) producing one or more pions. The following are several single pion electro–production reactions:

$$e + p \rightarrow e' + n + \pi^{+} \tag{1}$$

$$e + p \rightarrow e' + p + \pi^{0} \tag{2}$$

$$e + n \rightarrow e' + p + \pi^{-} \tag{3}$$

$$e + n \rightarrow e' + n + \pi^{0} \tag{4}$$

Single pion electro–production, as well as photo–production, is a promising source of information on the pion-nucleus interaction, and also on the structure of the nucleon and its excited states. Therefore, both experimental and theoretical studies started soon after the discovery of the pion, but until recently there had been relatively slow progress due to experimental difficulties. Today, these difficulties are being overcome by the development of high intensity, high duty cycle electron accelerators, such as MAMI (Mainz), BATES (MIT) and recently Jefferson Lab (Newport News), and with the improvement in detection and data processing equipment, which altogether promise data with greatly improved accuracy and kinematic coverage. This field of study, consequently, draws more attention in both experimental and theoretical studies than ever.

One of the main programs in Hall B at Jefferson Lab (formerly known as CEBAF), Newport News, VA, is the study of spin observables. The EG1 run group, part of the experimental program in Hall B, originally consisted of four experiments [5, 6, 7] and [8][3] using a polarized electron and photon beam incident upon polarized ammonia

[3] Despite the fact that this experiment was originally part of EG1, it is no longer in the run group

(NH_3) and deuterated ammonia (ND_3) targets. Particle detection is made possible by the CLAS (CEBAF Large Acceptance Spectrometer). CLAS is a nearly 4π detector and it allows us to detect multi-particle final states for exclusive measurements (pion production) in addition to the inclusive measurements, which only require detection of the scattered electron. A highly polarized electron beam is obtained using the GaAs-cathode technique. The proton and deuteron target materials used in the experiment were polarized using Dynamic Nuclear Polarization. Data for the first part of the EG1 run were taken in the fall of 1998. A second and longer run of the experiment lasted 7 months, from September 2000 to April 2001.

This dissertation describes the first measurement of the *double spin asymmetry* A_{et} in the $en \rightarrow e'\pi^- p$ reaction using the deuteron data taken during the first part of the EG1 run. A_{et} is the ratio of the double polarization (beam and target) cross–section σ_{et} to the unpolarized cross–section σ_0. In chapter 2, the physics motivation and theoretical overview of the experiment are given. The CLAS detector and the polarized target will be described in the third chapter. Chapter four is reserved for the data analysis. Physics results and conclusions are discussed in chapters five and six.

because a different target is required for that measurement.

CHAPTER 2

THEORETICAL OVERVIEW AND MOTIVATION

2.1 INTRODUCTION

Perturbative QCD gives a satisfactory explanation for the interactions between hadrons, at high energies and short distances. However, QCD is nonperturbative in the low energy regime and, therefore, the rich phenomenology of low energy physics cannot be successfully predicted this way.

A low energy approximation to QCD is made by the *Chiral Perturbation Theory* (ChPT) [9, 10], which is an effective field theory of QCD including all interactions among pions, nucleons and delta isobars that are allowed by the QCD symmetries, particularly, (broken) chiral symmetry. Chiral symmetry is the fact that, for instance, the number of *left-handed* quarks is not related to the number of *right-handed* quarks. In perfect chiral symmetry, light flavor u and d quarks, and therefore pions, are massless. Chiral symmetry is explicitly broken due to the finite u and d quark masses and is spontaneously broken in nature leading to *Goldstone bosons*, particles with zero mass and zero spin. The pion appears as a Goldstone particle in the models with vanishing current quark masses. ChPT gives satisfactory results close to the pion threshold, where the non–resonant part of the pion-production cross–section is dominant. This non–resonant part of the cross–section (also known as the *background*) is due to the Born part of the pion production amplitude. In the case of pseudo–scalar (PS) coupling between pions and nucleons, the Born terms consist of s– and u–channel nucleon pole diagrams and t–channel meson exchange processes (see Fig. 1a), and the amplitude is gauge invariant. On the other hand, an additional diagram, the seagull or contact term (right bottom picture in Fig. 1a), is needed in order to maintain gauge invariance for pseudo–vector coupling. The resonant part (Fig. 1b) is due to the internal excitations of the nucleon and can only be calculated with phenomenological models. Such models of hadron structure use parameterizations of experimental results. New data can then be used to test and improve those model predictions.

This project, whose analysis details and results are given in the following sections, describes the first exploratory measurement of the double spin asymmetry in π^- electro–production from polarized neutrons. Deuterium is selected as the target since a pure neutron target is not available. The results are compared with two

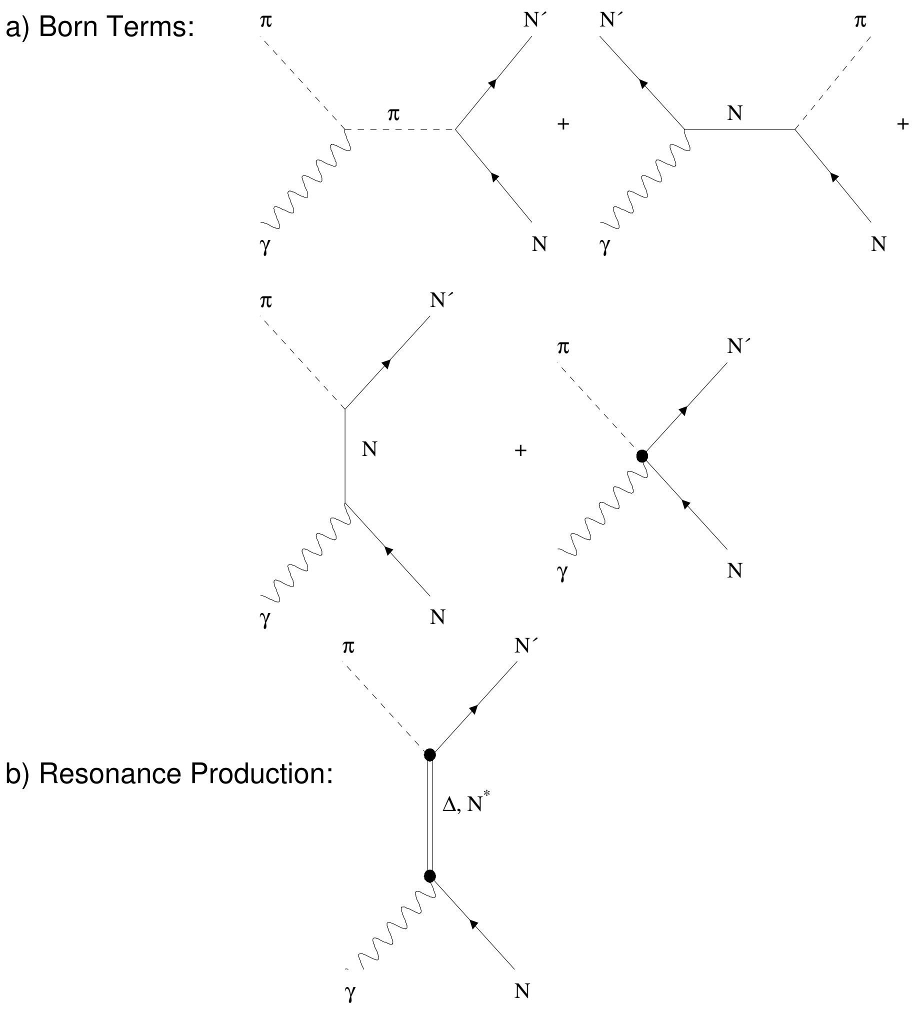

FIG. 1: Diagrammatic structure of the pion photo– (γ) or electro–production ($\gamma \to \gamma_v$). a) Born term contributions. b) Resonance contribution.

phenomenological models MAID and AO.

MAID is a unitary isobar model for pion photo- and electro–production on the nucleon, which contains the Born terms, vector mesons, and nucleon resonances $P_{33}(1232)$, $P_{11}(1440)$, $D_{13}(1520)$, $S_{11}(1535)$, $F_{15}(1680)$ and $D_{33}(1700)$ [11]. In this model, the non–resonance contributions are described using the standard Born terms with a mixed pseudovector–pseudoscalar πNN coupling and vector meson exchange, while the resonance contributions are included taking into account unitarity to obtain the correct phases of the pion photo–production multipoles.

The second model that is widely used is the *Amplitudes and Observables* (AO) model, which makes empirical parameterizations from fits to the existing electro–production data. This model contains Born and non-Born background terms, in addition to the resonances $P_{33}(1232)$, $P_{11}(1440)$, $D_{13}(1520)$, $S_{11}(1535)$, $F_{15}(1680)$, $S_{11}(1650)$, $S_{31}(1620)$, $D_{13}(1700)$, $D_{33}(1700)$, $D_{15}(1675)$, $P_{13}(1720)$, $P_{31}(1910)$, $P_{33}(1920)$, $F_{35}(1905)$ and $F_{37}(1950)$ [12].

In the following sections of this chapter, single pion electro–production is discussed and a brief overview of the three major resonance regions is given.

2.2 SINGLE PION ELECTRO–PRODUCTION

Pion production via electron scattering, pion electro–production, is one of the main sources of information on the structure of the nucleon and nucleon excitations. The electromagnetic interactions of electrons are well-described by *Quantum Electrodynamics* (QED). Therefore, the well-defined leptonic vertex in electron scattering can be separated from the hadronic vertex, the study of which will provide new information. In electron scattering, the momentum transfer to the system varies, and the dependence on this momentum transfer is directly related to the spatial structure of the target system off which the electron is scattered.

Studying electromagnetic excitations of nucleon resonances gives the opportunity to extract information on the three photocoupling amplitudes, $A_{1/2}$, $A_{3/2}$ and $S_{1/2}$, of the $\gamma_v NN^*$ vertex as a function of momentum transfer. The two amplitudes $A_{1/2}$ and $A_{3/2}$ represent the transverse helicity amplitudes while $S_{1/2}$ is the longitudinal amplitude. The subscripts 1/2 and 3/2 refer to the total helicity of the $\gamma_v N$ system. Information on these quantities is important for testing theoretical predictions of the electromagnetic coupling of photons to hadrons.

2.2.1 Inclusive and Exclusive Measurements

Inclusive measurements, in which only the scattered electron is detected, show three broad prominent resonance bumps as a function of invariant mass. The first of those resonances is the $P_{33}(1232)$ (also known as Δ), which is the dominant resonance at low momentum transfer. The second bump includes the $S_{11}(1535)$ and the $D_{13}(1520)$ while the third is mainly $F_{15}(1680)$ (see Fig. 2). Above, in the commonly used notation, the orbital angular momentum l of the final state is represented using the spectroscopic notation S, P, D, F, etc. for $l = 0, 1, 2, 3, ...$ The subscripts represent $2I$ and $2J$, where I is the isospin and J is the total angular momentum of the channel. For instance, the excitation of the $\Delta(1232)$ with the spectroscopic notation P_{33} denotes that it is a resonance in the πN P–state. The indices 33 represent isospin 3/2 and total angular momentum 3/2, respectively.

The broad bumps in Fig. 2 in fact consist of many closely spaced overlapping resonances, which are impossible to distinguish via inclusive measurements. They can be separated according to their spin and isospin assignments by measuring particular reactions such as $\gamma N \to \pi N$ (see Fig. 3), $\gamma N \to \eta N$ or $\gamma N \to \rho N$[1]. Exclusive electro–production experiments, in which one of the hadrons is detected in coincidence with the scattered electron, started in the early 1970's [13].

Charged pions, π^+ and π^-, have a mass of 139.57 MeV while neutral pions have a mass of 134.97 MeV. This mass splitting of about 5 MeV is due to electromagnetic interactions, which break the isospin symmetry between charged and neutral pions. The relatively low mass of the pion makes pion production the lowest-energy reaction to produce an extra hadron. This is one of the reasons why the pion plays such an essential role in strong interaction physics. Another reason is that many nucleon resonances, for instance the $\Delta(1232)$, have large branching ratios in the πN channels. Finally, the pion is the exchange particle in strong interactions among nucleons. For these reasons pion production is one of the primary tools we have for enhancing our understanding of strong interaction physics.

2.2.2 Formalism

The nature of the electromagnetic interaction itself makes electron scattering so useful. The coupling strength is given by the fine–structure constant $\alpha = e^2/\hbar c = 1/137$,

[1] γ can either be real or virtual.

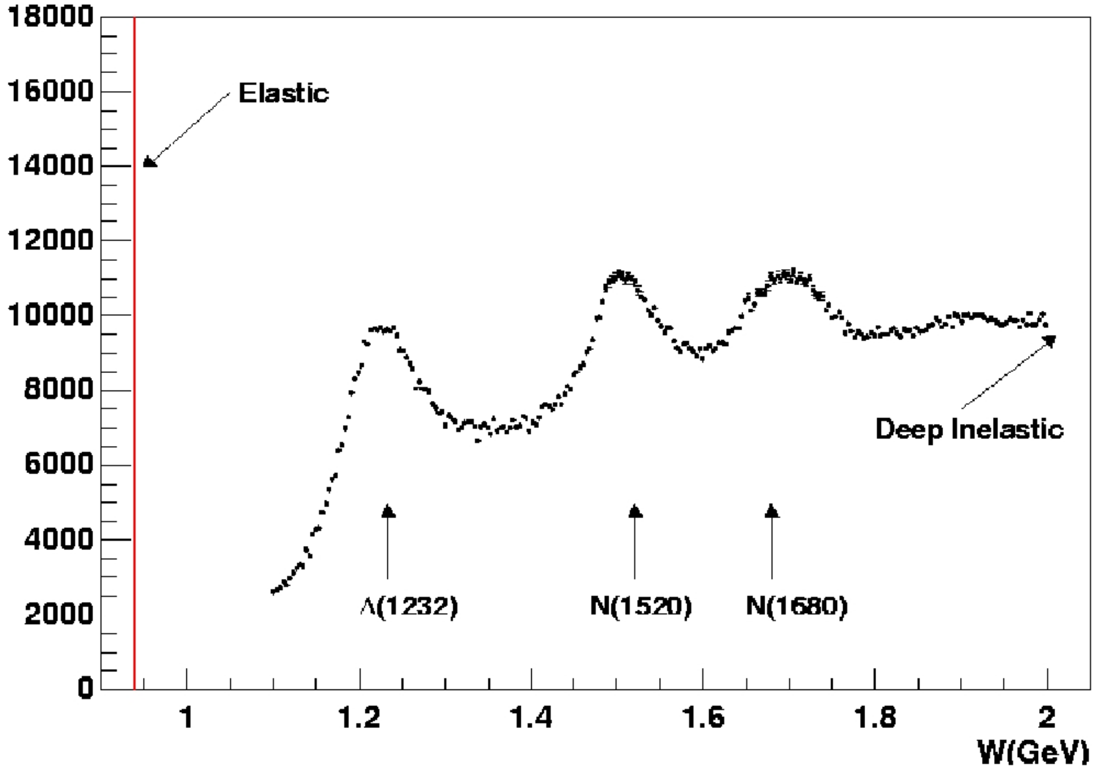

FIG. 2: Inclusive measurements $N(e, e')$ show three broad resonance bumps in the mass region below 2 GeV (data are from CLAS, W is the invariant mass of the $\gamma_v N$ system). These prominent features in fact consist of many closely spaced overlapping resonances which cannot be picked out via inclusive measurements.

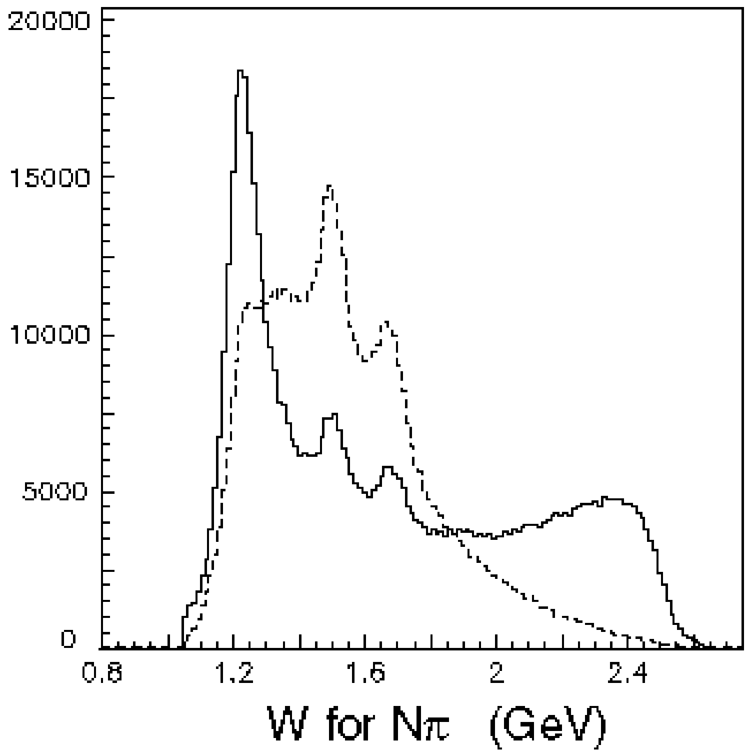

FIG. 3: The closely spaced overlapping resonances mentioned in section 2.2.1 can be separated via exclusive measurements. The figure indicates the sensitivity of the π^0 (solid line) and π^+ (dashed lines) channels to different excitations of the nucleon. The data are from CLAS.

which is introduced at each vertex in an electromagnetic interaction[2]. Because α is much smaller than one, diagrams with more vertices contribute less to the final result. Therefore, only the lowest order processes, in which a single virtual photon is exchanged, need to be considered (except for radiative corrections).

A diagram of such a process, single pion electro–production in the one–photon–exchange approximation (o.p.e.a), is shown in Fig. 4. This process can be considered in two steps: The electron emits a virtual photon, and this photon is absorbed by the target nucleon. Virtual photons can have three possible angular momentum orientations $m = \pm 1, 0$ and can have any mass. Real photons, on the other hand, can only have $m = \pm 1$ and they have zero mass. The photons with $m = \pm 1$ are called transverse photons and their electric and magnetic field vectors are perpendicular to the direction of propagation. In the case of longitudinal virtual photons m is zero and such photons couple to the electric charge of the target nucleon.

In Fig 4, the incident and scattered electrons are denoted by four-momentum $k_i = (\epsilon_i, \mathbf{k_i})$ and $k_f = (\epsilon_f, \mathbf{k_f})$, respectively. The interaction between the electron and the nucleon is described by the exchange of a virtual photon with an energy $\nu = \epsilon_i - \epsilon_f$ and three-momentum $\mathbf{q} = \mathbf{k_i} - \mathbf{k_f}$ (four-momentum $q = (\nu, \mathbf{q})$). The spatial distribution of the nucleon can be explored by varying ν and $\mathbf{q}$ independently. The four-momentum transfer squared is an invariant quantity and is given by

$$Q^2 = -q^2 = \mathbf{q}^2 - \nu^2 = 4\epsilon_i\epsilon_f \sin^2(\theta/2), \tag{5}$$

where θ is the angle between the incident and the scattered electron direction. The mass of the excited hadronic system can be written as

$$W = (m_N^2 + 2m_N\nu - Q^2)^{1/2}, \tag{6}$$

where m_N is the rest mass of the target nucleon. In the case of real photons Q^2 becomes zero. The hadronic system is described by the four-momentum of the initial nucleon $p_i = (E_i, \mathbf{p_i})$ and that of the final nucleon $p_f = (E_f, \mathbf{p_f})$, in addition to the four-momentum of the emitted pion, $p_\pi = (E_\pi, \mathbf{p}_\pi)$.

Kinematic quantities for single pion electro–production are shown in Fig. 5 and the angles θ^* and ϕ^* of the emitted pion in the center of mass (C.M.) system are indicated. Those two angles, together with Q^2 and W, are chosen to describe the hadronic system.

[2]In the remaining sections of this work, unless mentioned otherwise, the Planck constant h, the reduced Planck constant $\hbar \equiv h/2\pi$ and the speed of light in vacuum c will be taken as one.

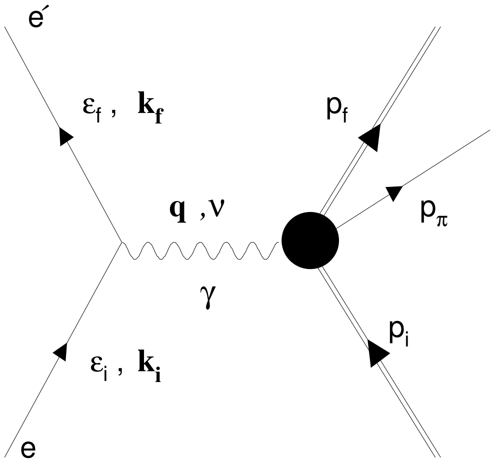

FIG. 4: Diagram for the exclusive pion electro–production process in the one-photon-exchange approximation.

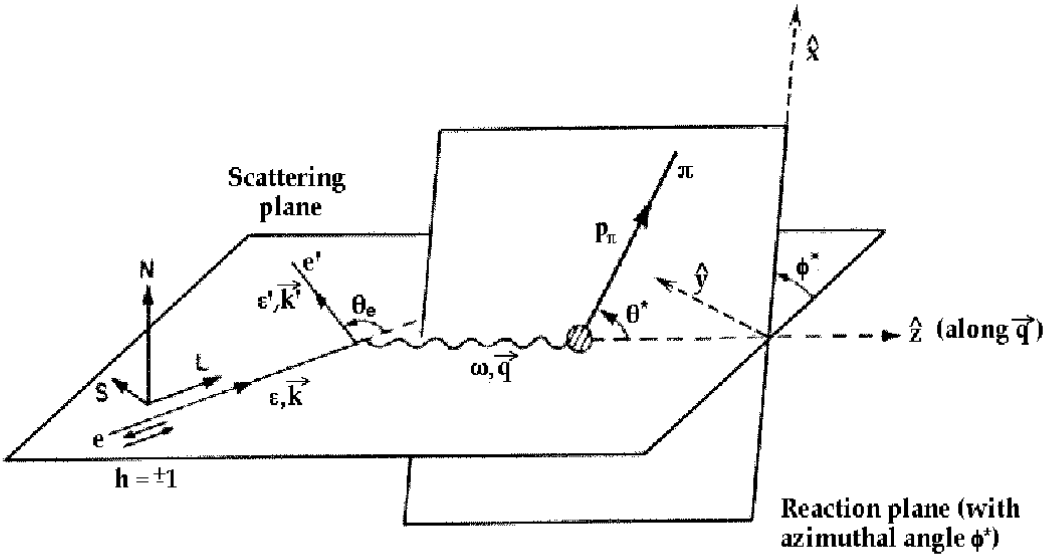

FIG. 5: The exclusive $(e, e'\pi)$ scattering process. The leptonic plane is defined by the initial and final momenta $\mathbf{k_i} = \mathbf{k}$ and $\mathbf{k_f} = \mathbf{k}'$. The direction of the virtual photon and the emitted pion define the hadronic plane. ϕ^* and θ^* are the center of mass angles between the leptonic and the hadronic plane, and between the virtual photon and the emitted pion, respectively. The helicity $h = \pm 1$ represents the directions parallel and anti–parallel to the electron beam direction.

The differential cross section for the exclusive scattering process shown in Fig. 4 in the laboratory frame ($p_i = (m_N, 0)$) may be written as (see for instance Ref. [14])

$$\begin{aligned} d\sigma &= \frac{\epsilon_i}{k_i}\frac{m_e}{\epsilon_i}\frac{m_N}{E_i}\frac{m_e}{\epsilon_f}\frac{d^3\mathbf{k_f}}{(2\pi)^3}\frac{1}{2E_\pi}\frac{d^3\mathbf{p}_\pi}{(2\pi)^3}\frac{m_f}{E_f}\frac{d^3\mathbf{p_f}}{(2\pi)^3}(2\pi)^4\delta^{(4)}(p_i + q - p_\pi - p_f) \\ &\quad \cdot| < p_f, p_\pi|J^\mu|p_i > q^{-2} < k_f|j_\mu|k_i > |^2, \end{aligned} \tag{7}$$

where only a pure electromagnetic process with electron currents j^μ and hadronic system currents J^μ are assumed. Weak neutral currents due to the exchange of the Z^0, the mediators of weak interactions, are excluded. The square of the transition matrix elements of the currents in the equation above is written in terms of the product of two second-rank tensors, the lepton tensor $\eta_{\mu\nu}$ and the hadron tensor $W_{\mu\nu}$. Following the notation of Drechsel and Tiator [14], the lepton tensor can be written as

$$\eta_{\mu\nu} = \sum_{s_f}(\overline{u}(k_f, s_f)e\gamma_\mu u(k_i, s_i))(\overline{u}(k_f, s_f)e\gamma_\nu u(k_i, s_i))^*, \tag{8}$$

where u and $\overline{u}$ are the incoming and outgoing electron Dirac spinors with corresponding four-momentum k_i and k_f, and spins s_i and s_f. The sum is over all spin observables in the final state. The equation above can also be written as

$$\eta_{\mu\nu} = \frac{e^2}{4m_e^2}((k_{f\mu} + k_{i\mu})(k_{f\nu} + k_{i\nu}) + q^2 g_{\mu\nu} + q^2 ih\epsilon_{\mu\nu\alpha\beta}q^{\alpha}(k_f^{\beta} + k_i^{\beta})), \tag{9}$$

where m_e is the electron mass, h is the helicity eigenstate of the longitudinal polarization[3] of the incident electron with $h = \vec{\sigma} \cdot \hat{\mathbf{k}}_{\mathbf{i}} = \pm 1$ ($\vec{\sigma}$ are the Pauli spin matrices), $g_{\mu\nu}$ is the symmetrical metric tensor and $\epsilon_{\mu\nu\alpha\beta}$ is the anti-symmetrical tensor ($\epsilon_{0123} = 1$). There exists gauge invariance since $q^{\mu}\eta_{\mu\nu} = \eta_{\mu\nu}q^{\nu} = 0$.

For the evaluation of the hadronic tensor,

$$W_{\mu\nu} =< p_f, p_{\pi}|J^{\mu}|p_i >< p_f, p_{\pi}|J^{\nu}|p_i >^*, \tag{10}$$

the hadronic matrix element of the electromagnetic current, $< p_f, p_{\pi}|J^{\mu}|p_i >$, is expressed through the C.M. helicity amplitudes for the virtual process $\gamma_v + N \to \pi + N$, where a spin 1 object, the virtual photon, is absorbed by the nucleon with spin 1/2 to produce a spin 1/2 and a spin zero particle in the final state. This can be described in the following way [15]:

$$\epsilon_{\mu}(\lambda) < p_f, p_{\pi}|J^{\mu}|p_i >=< \lambda_f|T|\lambda_i, \lambda_{\gamma} >, \tag{11}$$

where $\epsilon_{\mu}(\lambda)$ is the polarization vector of the virtual photon, λ_i, λ_f and λ_{γ} are the helicities of the incoming nucleon, outgoing nucleon and the virtual photon, respectively. The process gives a total of twelve complex helicity amplitudes, but only six of them are independent due to parity symmetry. The notation H_i ($i = 1$ to 4) is adopted [16] for the four transverse helicity amplitudes, which correspond to $\lambda_{\gamma} = 1$ and to $(\lambda_f, \lambda_i) = (-\frac{1}{2}, -\frac{1}{2}), (-\frac{1}{2}, \frac{1}{2}), (\frac{1}{2}, -\frac{1}{2})$ and $(\frac{1}{2}, \frac{1}{2})$. It is also useful to construct linear combinations of those four complex helicity amplitudes:

$$h_{\pm}^{N} = \frac{1}{\sqrt{2}}(H_4 \pm H_1) \tag{12}$$

and

$$h_{\pm}^{F} = \frac{1}{\sqrt{2}}(H_3 \mp H_2), \tag{13}$$

where $h_{+}^{N,F}$ correspond to incident photons polarized perpendicularly to the scattering plane and $h_{-}^{N,F}$ correspond to photon polarization parallel to the scattering plane. The

[3]At high energies ($\epsilon_i \gg m_e$) the small electron mass precludes experiments with transversally polarized beams.

initials F and N refer to baryon flip and non-flip, respectively. There are also two longitudinal amplitudes,

$$h_0^N =< 1/2|T|1/2, 0 > \tag{14}$$

and

$$h_0^F =< 1/2|T| - 1/2, 0 >, \tag{15}$$

and they can only be accessed via electron scattering.

In the o.p.e.a., the electroproduction cross section can finally be expressed in the form [17, 18]

$$\frac{d\sigma}{d\epsilon_f d\Omega_l d\Omega_\pi} = \Gamma_t \frac{d\sigma}{d\Omega_\pi}, \tag{16}$$

where $d\Omega_l$ is the solid angle of the scattered electron in the lab system, $d\Omega_\pi$ is the solid angle of the pion in the hadronic C.M. system and

$$\Gamma_t = \frac{\alpha}{2\pi^2}\frac{\epsilon_f}{\epsilon_i}\frac{k_\gamma}{Q^2}\frac{1}{1-\epsilon} \tag{17}$$

is the virtual photon flux factor. In this expression, $k_\gamma = (W^2 - m_N^2)/2m_N$ is the equivalent photon energy, the laboratory energy needed by a photon to excite the hadronic system with a C.M. energy W, and ϵ is the degree of transverse virtual photon polarization that can be described through quantities in the lab system as

$$\epsilon = (1 + \frac{2\mathbf{q}^2}{Q^2}\tan^2\frac{1}{2}\theta)^{-1}. \tag{18}$$

The six parity conserving complex amplitudes in eqs. [12]–[15] involve at least eleven independent quantities (also called response functions) that need to be measured for a complete determination of the process. The electro–production cross–section can symbolically be written as

$$\sigma = \sigma_0 + \sigma_e + \sigma_t + \sigma_{et}, \tag{19}$$

where σ_0, σ_e, σ_t, and σ_{et} are the cross–section terms for the case where neither the beam nor the target is polarized, only the electron beam is polarized, only the target nucleon is polarized and both the electron beam and the target nucleon are polarized, respectively.

Experiments involving both unpolarized beam and target can only determine four of the eleven observables mentioned in the previous paragraph. The pion electro–production cross–section in that case is written as [15]

$$\frac{d\sigma}{d\Omega_\pi} = \sigma_T + \epsilon\sigma_L + \epsilon\sigma_{TT}\cos 2\phi^* + \sqrt{\frac{1}{2}\epsilon(1+\epsilon)}\sigma_{LT}\cos\phi^*, \tag{20}$$

where σ_T is the differential cross–section for unpolarized transverse virtual photons[4], the term $\epsilon\sigma_L$ is the differential cross–section due to the longitudinal photons, the third term on the r.h.s of eq. [20] is the modification of the cross–section due to transverse linear polarization of the photons and the last term originates from the interference between longitudinal and transverse components. Those four terms can be expressed in terms of the amplitudes in eqs. [12]–[15]

$$\sigma_T = \frac{|\mathbf{p}_\pi| W}{k_\gamma m_N}\frac{1}{2}(|h_+^N|^2 + |h_+^F|^2 + |h_-^N|^2 + |h_-^F|^2), \tag{21}$$

$$\sigma_L = \frac{|\mathbf{p}_\pi| W}{k_\gamma m_N}(|h_0^N|^2 + |h_0^F|^2), \tag{22}$$

$$\sigma_{TT} = \frac{|\mathbf{p}_\pi| W}{k_\gamma m_N}\frac{1}{2}(|h_-^N|^2 + |h_-^F|^2 - |h_+^N|^2 - |h_+^F|^2), \tag{23}$$

$$\sigma_{LT} = \frac{|\mathbf{p}_\pi| W}{k_\gamma m_N} 2\mathcal{R}e(h_0^N h_-^{N^*} + h_0^F h_-^{F^*}), \tag{24}$$

where $\mathbf{p}_\pi$ is the pion momentum in the C.M. frame [15]. Determination of the remaining response functions, and therefore the complete model–independent determination of single pion electro–production is only possible by using polarized beams and targets.

If only the electron beam is polarized (longitudinally) the cross–section in eq. [19] contains a fifth term

$$\sigma_e = -h_e \frac{|\mathbf{p}_\pi| W}{k_\gamma m_N}\sqrt{2\epsilon(1-\epsilon)}\sin\phi^* \mathcal{I}m(h_0^N h_-^{N^*} + h_0^F h_-^{F^*}), \tag{25}$$

where h_e represents the helicity of the electron. Note that σ_e and σ_{LT} given in eq. [24] are proportional to the imaginary and real part of the same function. If the target is polarized the σ_t term

$$\begin{aligned}\sigma_t = \frac{|\mathbf{p}_\pi| W}{k_\gamma m_N}\{ & P_x[-\sqrt{2\epsilon(1+\epsilon)}\sin\phi^* \mathcal{I}mX_1 - \epsilon\sin 2\phi^* \mathcal{I}mX_2] \\ & -P_y[\mathcal{I}mY_1 + \epsilon\cos 2\phi^* \mathcal{I}mY_2 + 2\epsilon\mathcal{I}mY_3 + \sqrt{2\epsilon(1+\epsilon)}\cos\phi^* \mathcal{I}mY_4] \\ & +P_z[\epsilon\sin 2\phi^* \mathcal{I}mZ_2 + \sqrt{2\epsilon(1+\epsilon)}\sin\phi^* \mathcal{I}mZ_1]\},\end{aligned} \tag{26}$$

is present in eq. [19]. The following abbreviations are used in eq. [26] (Ref. [15]):

$$X_1 = h_0^F h_+^{N^*} + h_0^N h_+^{F^*},$$

[4]In the limit $Q^2 \to 0$, this term approaches the photo–production cross–section by real photons.

$$
\begin{aligned}
X_2 &= h_-^F h_+^{N^*} + h_-^N h_+^{F^*}, \\
Y_1 &= h_+^N h_+^{F^*} + h_-^N h_-^{F^*}, \\
Y_2 &= h_-^N h_-^{F^*} - h_+^N h_+^{F^*}, \\
Y_3 &= h_0^N h_0^{F^*}, \\
Y_4 &= h_0^N h_-^{F^*} - h_0^F h_-^{N^*}, \\
Z_1 &= h_0^N h_+^{N^*} - h_0^F h_+^{F^*}, \\
Z_2 &= h_-^N h_+^{N^*} - h_-^F h_+^{F^*}.
\end{aligned}
$$

Finally, a double polarization term is given by

$$
\begin{aligned}
\sigma_{et} &= -h_e \frac{|\mathbf{p}_\pi| W}{k_\gamma m_N} \{-P_x[\sqrt{2\epsilon(1-\epsilon)}\cos\phi^* \mathcal{R}eX_1 + \sqrt{1-\epsilon^2}\mathcal{R}eX_2] \\
&\quad + P_y \sqrt{2\epsilon(1-\epsilon)}\sin\phi^* \mathcal{R}eY_4 \\
&\quad + P_z[\sqrt{1-\epsilon^2}\mathcal{R}eZ_2 + \sqrt{2\epsilon(1-\epsilon)}\cos\phi^* \mathcal{R}eZ_1]\}.
\end{aligned} \tag{27}
$$

The target polarization is described in the $\{\hat{x}, \hat{y}, \hat{z}\}$ frame, where $\hat{z}$ is along the virtual photon direction, the $\hat{y}$ axis is perpendicular to the hadronic plane and the $\hat{x}$ axis is defined by $\hat{x} = \hat{y}$ x $\hat{z}$ (see Fig. 5). P_x, P_y, and P_z are the projections of the spin vector (in the target rest frame) onto the $\hat{x}, \hat{y}$, and $\hat{z}$ axes, respectively. It should be noted that, using a polarized target, only the imaginary parts of helicity amplitude products are measured, as seen in eq. [26], whereas information on the corresponding real parts can only be accessed by the additional use of polarized leptons.

2.2.3 Polarization Observables

Exclusive pion electro–production comes not only from resonance decays, but from non-resonant processes, as well. Existence of this background contribution (see section 2.1), along with the tails of other resonances, make the complete determination of the multipole components in a transition harder. Development of the new generation of electron accelerators allows a significant improvement in determining resonance amplitudes by the measurements of polarization observables. Exploiting the polarization observables is significant because many of the observables result from interferences between a large and a small amplitude, which makes the observable linear in the small amplitude, and therefore, makes the determination of that observable easier than in an unpolarized measurement where the square of each amplitude contributes to the cross–section.

2.2.4 Definition of Asymmetries

Three independent asymmetries for polarized electron (A_e), polarized target (A_t) and both polarized electron and target (A_{et}), as well as $A_{||}$, are experimentally measured using different sets of data with opposite beam and/or target polarization as:

$$A_e = \frac{\sigma_e}{\sigma_0} = \frac{\sigma(+h_e) - \sigma(-h_e)}{\sigma(+h_e) + \sigma(-h_e)} \tag{28}$$

$$A_t = \frac{\sigma_t}{\sigma_0} = \frac{\sigma(+P_t) - \sigma(-P_t)}{\sigma(+P_t) + \sigma(-P_t)} \tag{29}$$

$$A_{et} = \frac{\sigma_{et}}{\sigma_0} = \frac{\sigma(+h_e, +P_t) + \sigma(-h_e, -P_t) - \sigma(+h_e, -P_t) - \sigma(-h_e, +P_t)}{\sigma(+h_e, +P_t) + \sigma(-h_e, -P_t) + \sigma(+h_e, -P_t) + \sigma(-h_e, +P_t)} \tag{30}$$

$$A_{||} = \frac{\sigma_e + \sigma_{et}}{\sigma_0 + \sigma_t} = \frac{\sigma(+h_e, +P_t) - \sigma(-h_e, +P_t)}{\sigma(+h_e, +P_t) + \sigma(-h_e, +P_t)}, \tag{31}$$

where the target polarization is indicated with the vector $P_t = (P_x, P_y, P_z)$. The x, y and z directions are shown in Fig. 5. For the EG1 experiment, the target polarization is arranged to be parallel to the direction of the electron beam such that

$$P_t = (P_x, P_y, P_z) = P_t(\sin\theta_\gamma \cos\phi^*, -\sin\theta_\gamma \sin\phi^*, \cos\theta_\gamma), \tag{32}$$

where θ_γ is the angle between the target spin and the virtual photon momentum direction.

In experiments with polarization degrees of freedom, the cross–sections for polarization in one direction and in the opposite direction are usually different, producing an asymmetry varying between 1 and -1. In order to measure the new response functions introduced by the polarized electron and target, the angular distribution of the emitted pion needs to be detected or spin asymmetries need to be measured. For the cases where the incident electron is polarized along its direction of motion ($h_e = \pm 1$), a fraction of the electron helicity, $\sqrt{1-\epsilon^2}h_e$, is transferred to the virtual photon [19] where ϵ is the virtual photon polarization defined as

$$\epsilon = (1 + 2(1 + E_\nu^2/Q^2)\tan^2(\theta/2))^{-1}, \tag{33}$$

with ν being the difference between the beam energy and the energy of the scattered electron. If the target is polarized along the direction of the virtual photon, a difference between the absorption strength for virtual photons with opposite helicity occurs. After the virtual photon is absorbed by the target, the final state can either have a total spin 1/2 (if the virtual photon and target are aligned in opposite directions) or 3/2 (if they are aligned in the same direction). The corresponding cross–sections for absorption of a transverse virtual photon are denoted by $\sigma_T^{1/2}(\gamma_v)$ and $\sigma_T^{3/2}(\gamma_v)$, and they are related to the total transverse cross–section σ_T by

$$\sigma_T = \frac{\sigma_T^{1/2}(\gamma_v) + \sigma_T^{3/2}(\gamma_v)}{2}. \tag{34}$$

If one integrates over the pion azimuthal C.M. angle ϕ^*, σ_e and σ_t (see eqs. [25] and [26]) in eq. [31] are zero. In this case the asymmetry $A_{||}$ reduces to A_{et}. Following the formalism of inclusive asymmetries [19], A_{et} can then be expressed as

$$A_{et} = \sqrt{1-\epsilon^2}\cos\theta_\gamma \frac{A_1 + \eta A_2}{1+\epsilon R}, \tag{35}$$

where $\eta = \tan\theta_\gamma\sqrt{2\epsilon/(1+\epsilon)}$, R is the longitudinal–transverse cross–section ratio σ_L/σ_T, A_1 is the virtual photon asymmetry defined as

$$A_1(\gamma_v) = \frac{\sigma_T^{1/2}(\gamma_v) - \sigma_T^{3/2}(\gamma_v)}{\sigma_T^{1/2}(\gamma_v) + \sigma_T^{3/2}(\gamma_v)}, \tag{36}$$

and A_2 is a longitudinal–transverse interference term, σ_{LT}/σ_T. In eq. [35], unlike for the inclusive asymmetries, A_1 and A_2 are functions of θ^*.

For a detailed comparison of polarization measurements and unpolarized measurements see, for instance, Refs. [20] and [21]. This work focuses on the measurement of the double spin asymmetry A_{et} for π^- electro–production from a polarized deuteron target.

2.3 ELECTRO–EXCITATION OF THE BARYONIC RESONANCES

Study of the electromagnetic excitation of nucleon resonances yields information on the photocoupling amplitudes of the $\gamma_v NN^*$ vertex at varying four–momentum transfers Q^2. In the following section a brief overview of the three major resonance regions is given.

2.3.1 $N \to P_{33}(1232)$ transition

The $P_{33}(1232)$ or Delta resonance is the lowest mass state and the most dominant one of all the baryonic resonances at low momentum transfer. It is the only resonance that does not strongly overlap with other excited states and it strongly decays by single pion emission. The Δ was extensively studied experimentally during the 1960's and 70's at DESY [22] and NINA [23].

Three possible electromagnetic multipoles, a magnetic dipole M_{1+} and the electric and scalar quadrupoles E_{1+} and S_{1+}, may contribute to the $N \to \Delta$ transition. In the notation above, the subscripts $l\pm$ denote the orbital angular momentum l of the final state and the total spin $j = |l \pm 1/2|$. In quark models based on SU(6) symmetry, the Δ has all three quarks in an $s-$state and the $N \to \Delta$ transition is induced by the spin-flip of a single quark [25]. In this context, only $M1$ is non–zero, corresponding to a pure magnetic dipole transition, and thus $E_{1+}/M_{1+} = 0$. Non–zero values of E_{1+} and S_{1+} multiples are possible by $d-$state ($l = 2$) admixtures [24] in the ground and/or excited state. The size of E_{1+}/M_{1+} is predicted to be small for low to moderately high Q^2 by the quark models that include the one–gluon exchange contribution. At very high Q^2, helicity conservation predicts [26] that E_{1+}/M_{1+} approaches unity, while S_{1+}/M_{1+} approaches zero. Two simplifying assumptions are made in order to extract the quadrupole amplitudes from the measured θ^* and ϕ angular distributions. The two assumptions are that only $s-$ and $p-$waves are important in the πN system, and that only the dominant M_{1+} multipole, together with its interferences with other multipoles, is kept in the response functions.

Experiments at JLAB [31, 32] are proposed to measure the electric and scalar quadrupole transition more accurately over a large momentum transfer range using polarized electron beams. Cross–section measurements give information about the real part of the interference terms $\mathcal{R}e(E_{1+}M^*_{1+})$ or $\mathcal{R}e(S_{1+}M^*_{1+})$. The imaginary part of those interference terms, $\mathcal{I}m(E_{1+}M^*_{1+})$ and $\mathcal{I}m(S_{1+}M^*_{1+})$, can be accessed through single spin asymmetry measurements.

2.3.2 The Second Resonance Region

In the inclusive cross section, three resonant states, the $P_{11}(1440)$, the $D_{13}(1520)$ and $S_{11}(1535)$, contribute to the observed enhancement around $W = 1.5$ GeV. Baryons are classified into bands that have the same radial quantum numbers. In SU(6) quark models, the $P_{11}(1440)$ or Roper resonance is associated with a state in the $(56, 0^+_2)$ supermultiplet, while $D_{13}(1520)$ and $S_{11}(1535)$ are both members of the $(70, 1^-_1)$ supermultiplet, and therefore, their spatial wavefunctions are expected to be identical [33]. In the notation above, for instance in $(56, 0^+_2)$, 56 is the dimensionality of the SU(6) representation, 0 is the total quark angular momentum, + is the total parity, and 2 is the band number. The $S_{11}(1535)$ state has a very large decay width to the ηN, which is not the subject of this thesis but has recently been studied at JLAB [34].

In the total $\gamma p \to X$ cross section, where $Q^2 = 0$, the Roper resonance shows a strong electromagnetic coupling of $A_{1/2} = (70 \pm 5) \cdot 10^{-3}$ GeV$^{-1/2}$, which gives rise to a noticeable shoulder on the $D_{13}(1520)$–$S_{11}(1535)$ states [35]. On the other hand, the shoulder hardly exists in electro–production, where $Q^2 > 0$. This behaviour of the Roper resonance has recently attracted much theoretical and experimental attention. All analyses result in a consistent non-zero value for the transverse amplitude at the real photon point. A very rapid drop of $A_{1/2}$ is observed to a value consistent with zero at $Q^2 > 0.5$ GeV^2 (see, for instance, Ref. [33]). Both the non–relativistic [36] and relativized [37] quark models predict an increasing strength with increasing Q^2 relative to the $\Delta(1232)$. However, the latter predicts a fairly small value, which is inconsistent with the data, at the real photon point. At high Q^2 the non-relativistic quark model predicts

$$\frac{A^P_{1/2}(P_{11}(1440))}{A^P_{1/2}(P_{33}(1232))} \sim \vec{Q}^2, \tag{37}$$

so that the Roper should be the most dominant resonance at high Q^2.

Quark models predict a large $S_{1/2}$ amplitude, whereas the experimental results are consistent with zero [35]. The best description of the Q^2 dependence of the Roper resonance is provided by the model that describes the Roper as a gluonic partner of the nucleon [38]. It predicts a correct neutron/proton ratio of the $A_{1/2}$ amplitude to be $-2/3$, which agrees with the quark model estimates and the experimental results. It is clear that more data, especially at low Q^2, are needed for a better understanding of the situation [39].

The electromagnetic transition to the $D_{13}(1520)$ state is often investigated by measuring the helicity asymmetry A_1 which probes the helicity structure of the transition. This asymmetry is predicted by Capstick's quark model [41]. The prediction is that, the asymmetry should switch from -1 at the photon point, corresponding to 3/2 dominance, to $A_1 \sim 1$ for large Q^2, corresponding to helicity 1/2 dominance. Neutron and proton have different sensitivity to different model assumptions [40], and compared to protons, the zero crossing of the helicity for the neutron is predicted to appear at higher Q^2 [33]. The proposed experiments at JLAB will provide significantly improved accuracy on the proton, along with the first detailed electro–production results on the neutron [39].

2.3.3 Helicity Structure of the F_{15}(1680)

The $F_{15}(1680)$ is among a number of well known states, such as the $S_{11}(1650)$, $D_{15}(1675)$, $S_{31}(1620)$ etc., which appear in the third enhancement of the inclusive cross–section. In SU(6), the $F_{15}(1680)$ is a member of the $(56, 2_2^+)$ supermultiplet, whereas other states in the third resonance region are associated with the $(70, 1_1^-)$ supermultiplet. At $Q^2 = 0$ this transition is dominated by helicity 3/2 and $A_{1/2}(F_{15}, Q^2 = 0) \sim 0$, with a corresponding helicity asymmetry of ~ -1 [45], while for $Q^2 > 0$ the theoretical predictions show a rapid switch from helicity 3/2 to helicity 1/2 dominance, similar to the $D_{13}(1520)$ state. The data [43] support this prediction.

The goal of our work is to provide completely new information on the neutron resonances. The deuteron target includes protons as well as neutrons. However, by requiring only a π^-, electron and proton in the final state we are sensitive only to the neutron in the deuteron. With polarized deuterons and a polarized electron beam, we can, in principle, determine all of the helicity amplitudes contributing to eq. [19]. In reality one needs excellent statistics and a full angular coverage of π^- events in θ^* and ϕ^* to accomplish that feat. Here we report the first measurement of the double spin asymmetry for two Q^2 bins; 0.08 GeV$^2 < Q^2 <$ 0.4 GeV^2 and 0.4 GeV$^2 < Q^2 <$ 1.2 GeV^2. The details of the experiment are presented in the next chapter.

CHAPTER 3

THE EXPERIMENT

Single pion electro–production is one of our main sources of information on the structure of baryon resonances. However, most of the previous experiments have been limited to the measurement of the unpolarized cross–section due to the technological difficulties. Nowadays, those difficulties have been overcome with the development of modern high duty factor polarized electron accelerator facilities and polarized targets. With the development of the polarized electron beam at SLAC, we were able to use deep inelastic scattering (DIS) to measure the spin content of the proton carried by the quarks for the first time [46]. Meanwhile, polarization observables with real polarized photon beams and polarized proton or deuteron targets are already being measured in several laboratories around the world.

This work focuses on the analysis of data taken at the Jefferson Laboratory (JLab), using the polarized electron beam and a polarized target. The first section of this chapter is reserved for a brief description of JLab's electron accelerator. A detailed representation of the CEBAF Large Acceptance Spectrometer (CLAS) in Hall B is given in the second section. Detector calibration, event trigger and tracking, and the EG1 data set are briefly discussed in the following four sections. The description of the CLAS polarized target used for this experiment is given in the last section.

3.1 THE ACCELERATOR

The JLab's accelerator provides a high luminosity, high duty cycle (100%) continuous electron beam driven by superconducting RF cavities. A schematic view of the accelerator site is shown in Fig. 6. The polarized electron beam, produced by photoemission from a strained GaAs photocathode, has been available since 1998. In the photoemission process, circularly polarized laser light is transformed into the polarization of the emitted electrons. The beam is injected at an energy of 45 MeV into the first of the two parallel linacs, which are connected by a set of five recirculating arcs. The beam gains an additional energy of nominally 400 MeV in each linac, 800 MeV for each pass (up to five passes). The three experimental end stations, Halls A, B and C, can simultaneously share this highly polarized beam, using the same or a

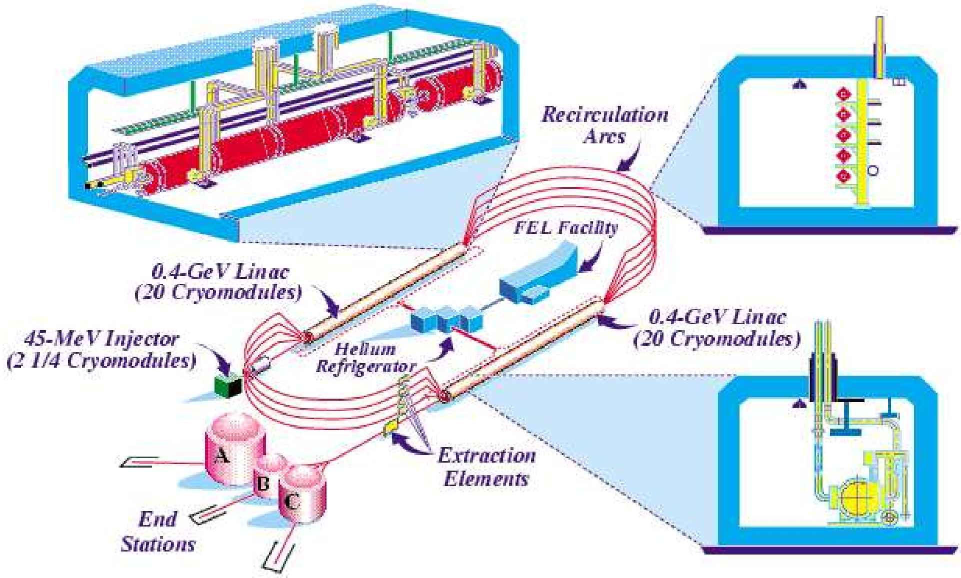

FIG. 6: The JLAB accelerator site.

different multiple of one pass energy for each of the experimental areas[1]. The electron beam arrives at each of the three targets in bunches with ~ 2 ns delay between each subsequent bunch. The beam currents can vary from 100 pA to 100 μA and can be different in each hall. The steering and focus of the beam is controlled by dipole and quadrupole magnets. The polarization of the beam during this experiment was flipped every second with a pseudo–random sequence, which means that the helicity is randomly chosen for the first of two seconds but is always followed by the opposite helicity.

Elastic scattering of incident electrons from free target electrons is called Møller scattering, which is a common technique to measure the high energy electron beam polarization. In Hall B, the home for the EG1 experiment, the polarization of the beam is measured by a Møller polarimeter [47] at the entrance to the Hall. The polarized electron target for the Møller polarimeter is provided by a magnetized iron foil. The beam polarization measured during the EG1 run period was $\sim 70\%$.

For the EG1 experiment, the beam was moved across the target surface in a spiral pattern (rastering) mainly in order to avoid any local depolarization or heating due to a non-uniform exposure of the polarized target to the beam [5]. Data for this work

[1]Two halls cannot have the same beam energy unless it is five pass

were collected at beam energies 2.949 GeV, 2.562 GeV, and 2.565 GeV. The beam current was varied from 0.5 nA to 4 nA, depending on the experimental conditions.

The rest of this chapter describes the CEBAF Large Acceptance Spectrometer (CLAS) in Hall B and the polarized target used for the experiment.

3.2 THE CLAS

Hall B, the smallest of the three experimental end stations, has been equipped with the CLAS. The detection of multiple particles in the final state is possible by this nearly 4π spectrometer. The CLAS is built around six superconducting coils, which are used to produce a toroidal magnetic field and which divide the detection system azimuthally into six independent tracking areas, called sectors. The beam moves along the axis of the coils (see Fig. 7). Throughout this work, the polar angle θ is defined as the angle made with the direction of the beam, while ϕ is the azimuthal angle around it. The magnetic field produced by the CLAS toroidal magnets is (mostly) perpendicular to the particle trajectory and bends charged particles towards or away from the beam axis leaving an essentially unchanged azimuthal angle. The $\int \mathbf{B} \times d\mathbf{l}$ varies from 0.5 Tesla·m for tracks beyond $\theta = 90°$ to 2 Tesla·m for high momentum tracks at the most forward angles [49]. The target is inserted in a field free region in the center of the CLAS.

The spectrometer consists of three regions of drift chambers (DC) to determine the trajectories of the charged particles, Cerenkov counters (CC) to distinguish electrons from pions, scintillation counters (SC) for the time of flight measurements, electromagnetic shower calorimeters (EC) to identify electrons and neutrals and large angle electromagnetic calorimeters (two sectors only). A cross–section drawing of the CLAS detector is shown in Fig. 8.

3.2.1 Drift Chambers

The drift chambers (DC) are used to determine the momentum of the charged particles [48, 49]. The CLAS consists of a total of 18 drift chambers (see Fig. 9) designed in three regions, each with six sectors.

Region 1 is the innermost of the three regions of the CLAS and located inside the torus magnetic coils, where the magnetic field is low. The detectors in this region track all charged particles prior to their entry into the toroidal magnetic field. The

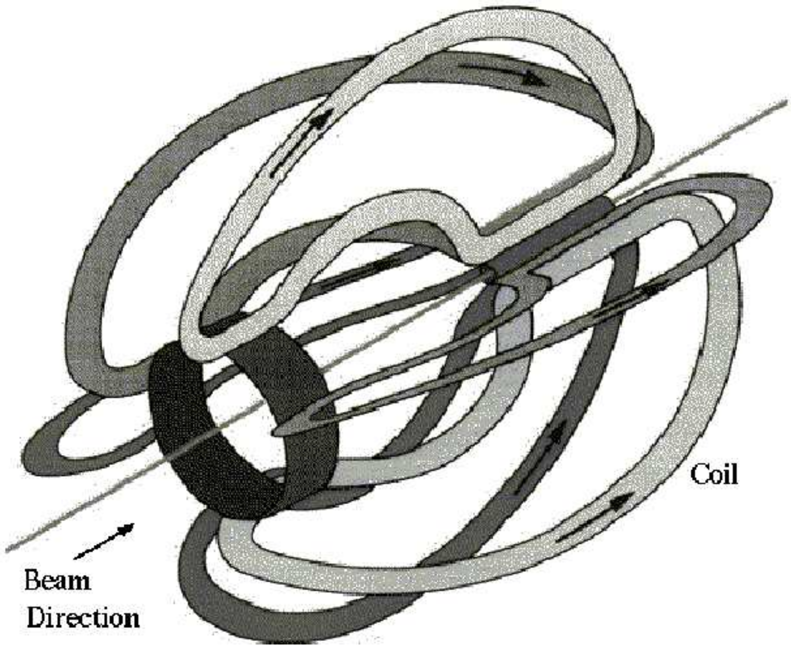

FIG. 7: The toroidal CLAS magnet.

Region 2 drift chambers are located between the torus coils in the high magnetic field region. A maximum magnetic field of 2 Tesla is in the azimuthal direction around the beam line in this region. Region 3 is located outside the magnet coils, where the magnetic field is low.

Each of the three regions of drift chambers consists of two superlayers, *stereo*, and *axial*. These superlayers consist of hexagonal drift cells (see Fig. 10) made of a *sense* wire in the center and six *field* wires surrounding it. The sense wires consist of 20 μm diameter gold–plated tungsten, while the field wires are made of 140 μm diameter gold–plated aluminum. The wires are strung in the azimuthal (ϕ) direction, which is perpendicular to the plane of the bent particle trajectory. The region 2 and 3 drift chambers each contain 12 sense–wire layers (6 per superlayer), while the region 1 drift chambers have only 10 layers (4+6) due to the lack of space. The drift chambers can detect charged particles over a polar range from $8°$ to $142°$.

The chambers are filled with a gas mixture of 90% Ar and 10% CO_2. This mixture was chosen since it has a quite high saturated drift velocity (>4 cm/μs), and it has an operating voltage plateau of several hundred volts before a breakdown [49]. The gas is maintained in an electric field such that when a charged particle first passes

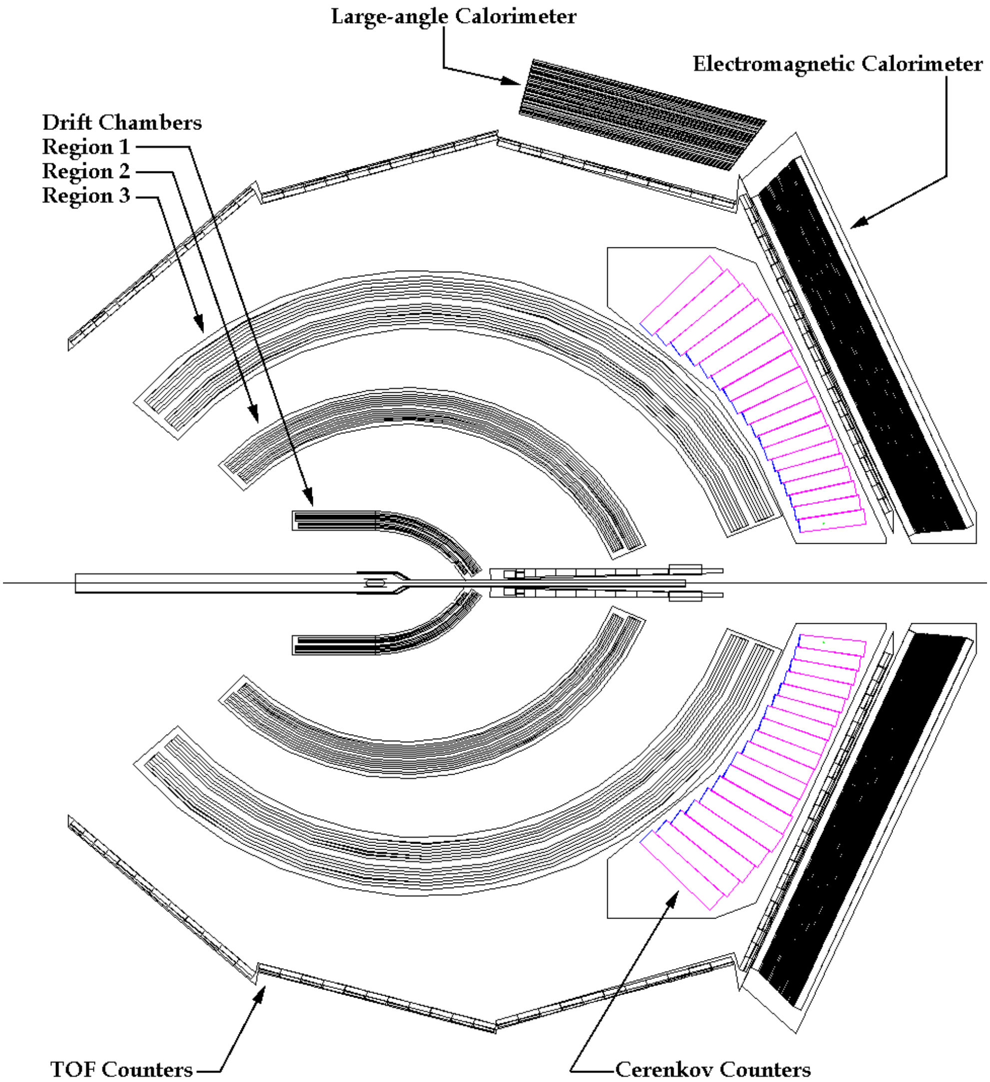

FIG. 8: A cross–section drawing of the CLAS with each detector element indicated.

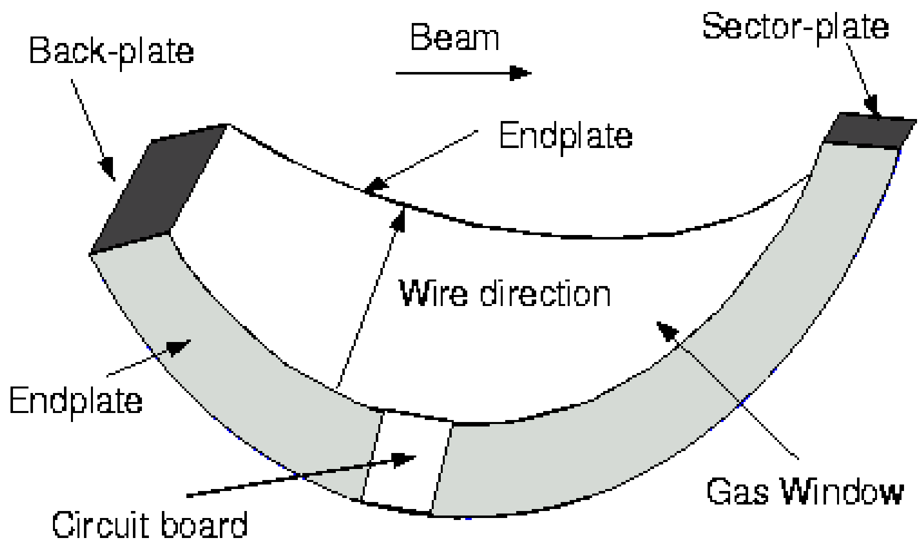

FIG. 9: A schematic view of a drift chamber. In CLAS, a total of 18 drift chambers are designed in three regions, each with six sectors.

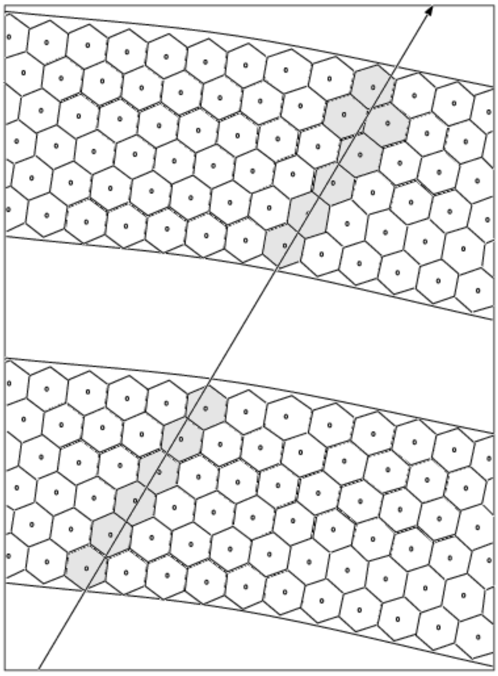

FIG. 10: A representative view of part of a drift chamber with a track passing through the six layers of hexagonal cells in each superlayer.

through this gas mixture, the gas is ionized and the produced electrons drift towards the sense wires (anodes), while the ions drift in opposite direction towards the field wires (cathodes). Meanwhile, the fast signal from the Time–of–Flight scintillators initiates a timer. When the electrons drifting towards the sense wires arrive at their destination, a signal is created at the anode and stops the timer to yield the drift time. The drift times are then converted into drift distances by using a pre–determined table and the final track parameters are determined by fitting these track positions in each cell.

3.2.2 Čerenkov Counters

When a charged particle passes through a medium with a velocity greater than the velocity of light in that medium, a visible electromagnetic radiation, Čerenkov light, is emitted. This process occurs at a threshold given by $\beta = 1/n$, where n is the refraction index of the medium. Čerenkov counters are constructed based on the exploitation of this physical effect.

Čerenkov counters in CLAS are used in order to distinguish electrons from other charged particles, mostly negative pions. They are positioned between the region 3 drift chambers and the time–of–flight (TOF) counters and cover a range of polar angles from 8° to 45°. Perfluorobutane (C_4F_{10}) is chosen as the radiator gas since it has a high refraction index ($n = 1.00153$), resulting in a high photon yield [50]. This refraction index is also corresponding to a threshold for particle energy equivalent to

$$E = \frac{m}{\sqrt{1-\beta^2}} = \frac{n}{\sqrt{n^2-1}}m = 18.1m, \tag{38}$$

where m is the rest mass of the particle in MeV. The equation above yields a threshold of 9 MeV for electrons and an acceptably high threshold for pions (~ 2.5 GeV).

Charged particle trajectories take place approximately in planes of constant azimuthal angle ϕ because of the approximately toroidal configuration of the magnetic field [50]. This property suggests that the light collection optics of the Čerenkov counters in CLAS be designed to focus the light in the ϕ direction. Each of the six sectors, therefore, is divided into 18 regions of polar angle (θ), and each θ segment is divided into two modules about the symmetry plane bisecting each sector, resulting in a total of 216 light collection modules (see Fig. 11).

3.2.3 Electromagnetic Calorimeters

The forward region ($8° < \theta < 45°$) of each sector in CLAS is equipped with a lead–scintillator electromagnetic sampling calorimeter (EC) in order to provide the primary electron trigger for CLAS, to reject pions, and to detect neutrals. Pion rejection for momenta below 2.8 GeV is mainly provided by the CC threshold. At higher momenta, on the other hand, pions must be identified by comparing the energy deposited in the EC with the particle momentum obtained from the curvature of the trajectories in the magnetic field, and from differences in the energy deposition pattern in the EC. A good particle identification relies also on matching EC hits with the hits in the SC and CC detectors, and with the projection of the drift chamber tracks onto the EC plane [51].

The calorimeter is made of alternating layers of scintillator strips and lead sheets. The lead:scintillator thickness ratio is 0.2, which requires 40 cm of scintillator and 8 cm of lead per module. Approximately 1/3 of the energy in a shower is deposited in the scintillator [51]. The lead–scintillator sandwich is contained within a volume with the shape of an equilateral triangle in order to match the hexagonal geometry of the

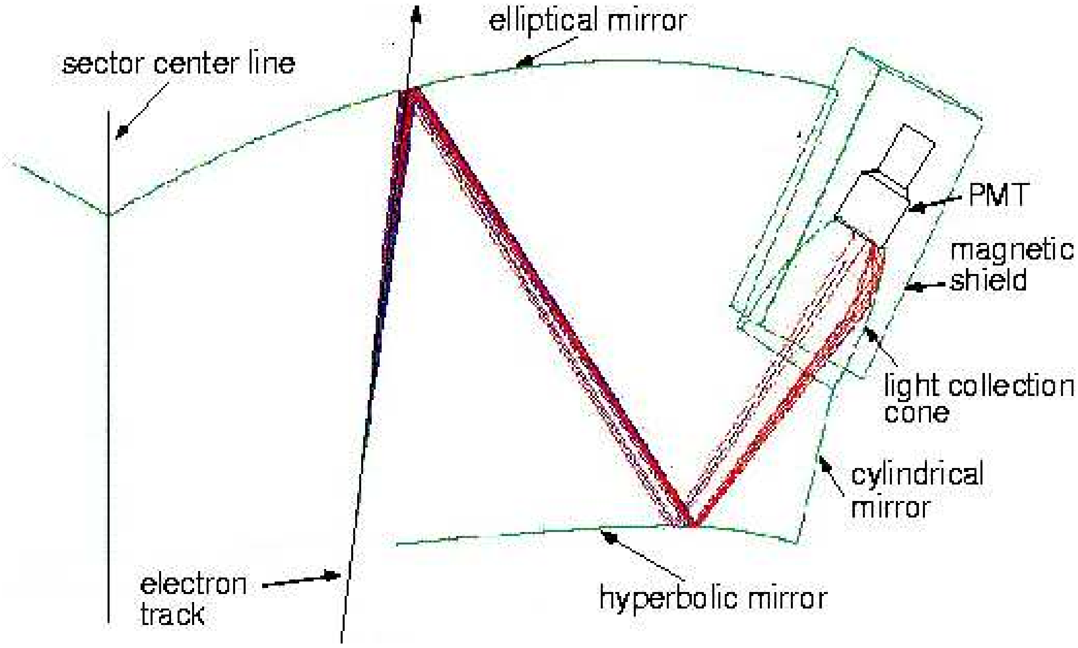

FIG. 11: Optical arrangement of one of the Čerenkov detector modules in CLAS with the optical and light collection components shown.

CLAS. The sandwich is composed of 39 layers, each of which consists of 10 mm thick scintillator followed by a 2.2 mm thick lead sheet. Each scintillator layer is made of 36 strips parallel to one side of the triangle. In each successive layer, the strip orientation is rotated by 120°, resulting in three orientations (*views*) u, v and w (see Fig. 12), each containing 13 layers, which provide information on the location of energy deposition. The first five layers of each view make the *inner* and the remaining eight layers make the *outer* stack. Each module requires 36(strips)×3(views)×2(stacks) = 216 photomultiplier tubes (PMTs), a total of 1296 PMTs for the six modules of EC in CLAS.

The scintillator light is transmitted to the PMTs via a fiber–optic light readout system. The PMT signals are then sent to ADC and TDC boards.

In addition to the forward angle ECs, a limited large-angle coverage is provided by the Large Angle Calorimeters (LAC) in sectors one and two. The two calorimeters cover a θ range of 45°–70°. The LACs, similar to the forward angle ECs, are made of 33 layers, each consisting of 2 mm thick lead foil and 1.5 cm thick plastic scintillators. For detailed information on the LACs see Ref. [52].

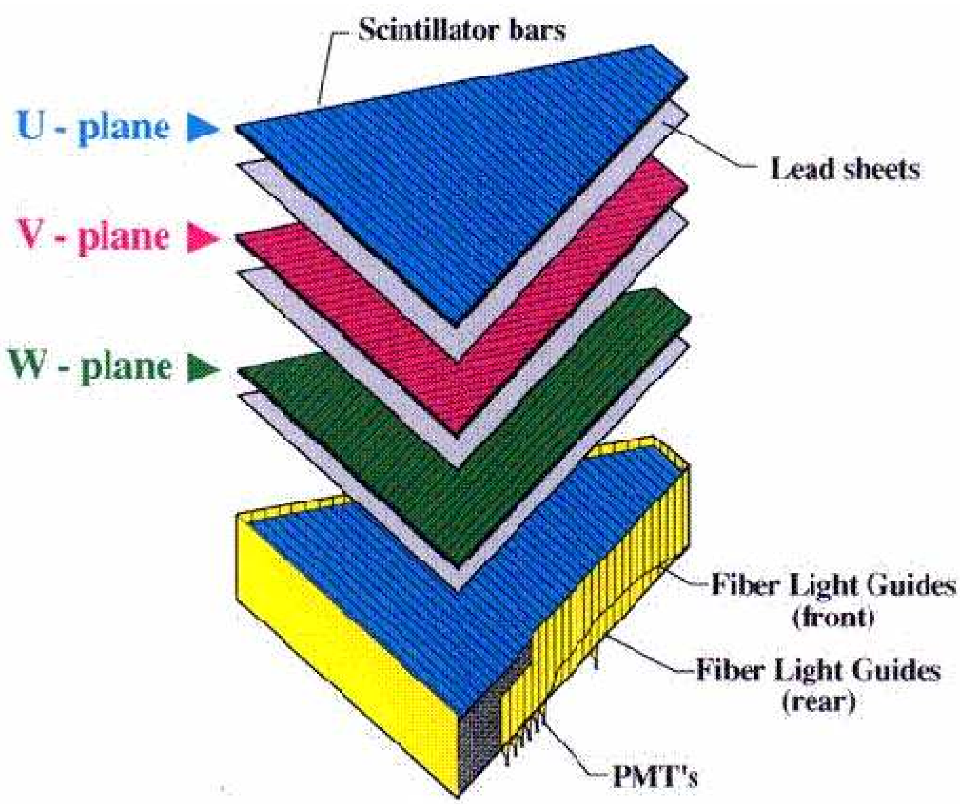

FIG. 12: An exploded view of one of the six CLAS electromagnetic calorimeter modules, with three views indicated.

3.2.4 Time of Flight Scintillators

In CLAS, particle identification relies mostly on the combination of measured charged–particle momenta and the time of flight from the target to the time of flight counters (TOF). The time of flight counters, also named scintillation counters (SC), are located between the Čerenkov counters and the electromagnetic calorimeters. They are used to measure the time for a particle to travel from the point of interaction at the target to the outer part of the detector where the TOF counters are located. The vertex time is determined by the accelerator RF. For electron beam experiments, the RF beam bucket which contains the electron causing the event is determined by identifying the final state electron (with a combination of EC and CC information), and tracing the $\beta = 1$ particle back to the interaction point.

The TOF system in CLAS covers an area of 206 m^2 and is composed of 5.08 cm thick, 15 and 22 cm wide scintillation counters, covering a range of θ between 8° and 142°. The lengths of the counters vary from 32 cm at the most forward angle to 450 cm at larger angles. Bicron BC–408 was selected as the scintillator material since it yields a single attenuation component of 500 cm and it is possible to fabricate scintillator pieces as long as 450 cm [53] (see Fig. 13).

The system has been designed to optimize the time resolution, which varies from about 80 ps for the short counters to 160 ps for the longer ones. This resolution is needed to allow separation of pions and kaons up to 2 GeV. The flight time variations between fast (*e.g.*, electrons) and slow particles (protons with momenta below 300 MeV) limit the timing in the trigger hardware, and for precise timing information, this requires the momentum and position information obtained from the drift chambers.

3.3 CALIBRATION AND COOKING

In order to convert the *raw* data (hits registered in ADCs and TDCs) into a useful form for physics analysis, each detector element mentioned in the previous sections must be calibrated. The calibration process includes, for instance, time–to–distance calibration for the DCs, energy and timing calibration for the ECs, and time–walk corrections for the TOFs. In order to perform the calibrations, approximately 10% of the data, which is chosen uniformly throughout the complete data for the run period, is selected and processed. A separate calibration process is required for each of the run periods since there may be different running conditions and some modifications

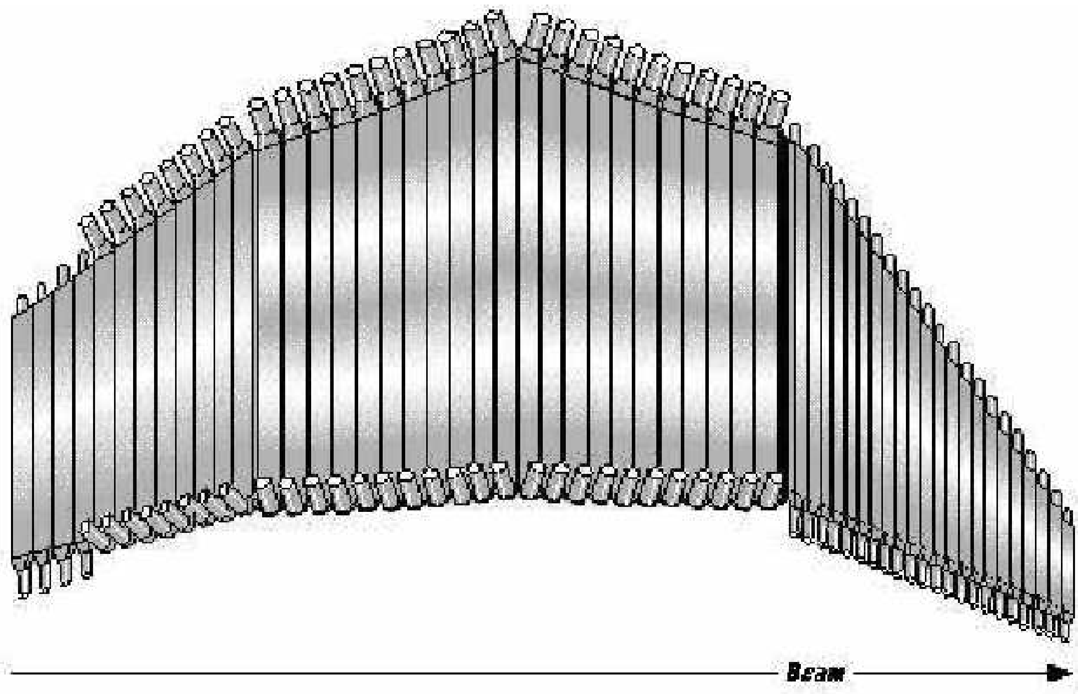

FIG. 13: A schematic view of the scintillation counters in CLAS.

in the hardware during each data taking.

After the calibration for each detector component is completed, the old calibration constants are replaced with the new ones and they are *frozen* to be used by the particular run period for a massive data processing, the *cooking*.

3.4 EVENT TRIGGER AND THE DATA ACQUISITION SYSTEM

The data acquisition system (DAQ) records ADC and TDC information for any signal seen in the various detector components if the event satisfies the trigger condition. For the EG1 experiment, the trigger condition is the detection of a simultaneous hit above a previously determined threshold in both the Čerenkov counters and the electromagnetic calorimeters. The thresholds used during the EG1 run period (150 mV for the EC and 38 mV for the CC) resulted in $\sim 60\%$ of the events at 2.5 GeV including an electron. The remaining events, which are thrown away during the event reconstruction process, are due to noise or due to fast hadrons that produce a signal in the CC. The DAQ rate during the experiment was ~ 2 kHz.

3.5 TRACKING AND START TIME RECONSTRUCTION

Every detector element has a corresponding reconstruction package. The reconstructed event data are stored in the *BOS* format, which is a program system written in standard Fortran–77, for the dynamic management and for the input/output of data sets [54]. In this section the most complicated part of the reconstruction, the tracking code, and the event start reconstruction are discussed.

For a large angle spectrometer like CLAS, charged particle tracking is crucial for the reconstruction software. The track (position and angle) of a charged particle at the target is reconstructed using the information provided by the drift chambers and the TOF. Tracking is performed in two stages. In the first stage, individual tracks are fit only to hit–wire positions, which is known as *hit–based* tracking. The track segments in different superlayers are collected and then linked together to form a track (candidate) across the three regions within one sector. Based on the hit pattern, preliminary momentum and charge determination, together with the extrapolation of the track to the interaction vertex and outer detector elements (CC, TOF, and EC), is possible.

In the second tracking stage, flight time information of the particle from the target to the outer scintillators is used to correct the measured drift times. The drift time is given as

$$t_{drift} = t_{start} + t_0 - t_{TDC} - t_{flight} - t_{prop} - t_{walk}, \tag{39}$$

where t_{start} is the event start time, t_0 is the fixed time delay for the wire, t_{TDC} is the raw TDC time, t_{flight} is the particle flight time from the target to the hit position, t_{prop} is the signal propagation time along the wire, and lastly, t_{walk} is a *time–walk* correction, which is made for short drift times due to different ionizations for slow and fast particles [49].

The corrected drift time is then converted into the drift distance from a sense wire to the particle's path for each hit in the drift chamber using a pre–determined table (see section 3.2.1). Eventually, in order to find the final track parameters, the corrected track positions in each drift cell are fit in a procedure known as *time–based* tracking.

Each circle around the sense wire in Fig. 14 represents the distance–of–closest–approach (DOCA), which is calculated by the time–to–distance functions parameterized during the drift chamber calibration.

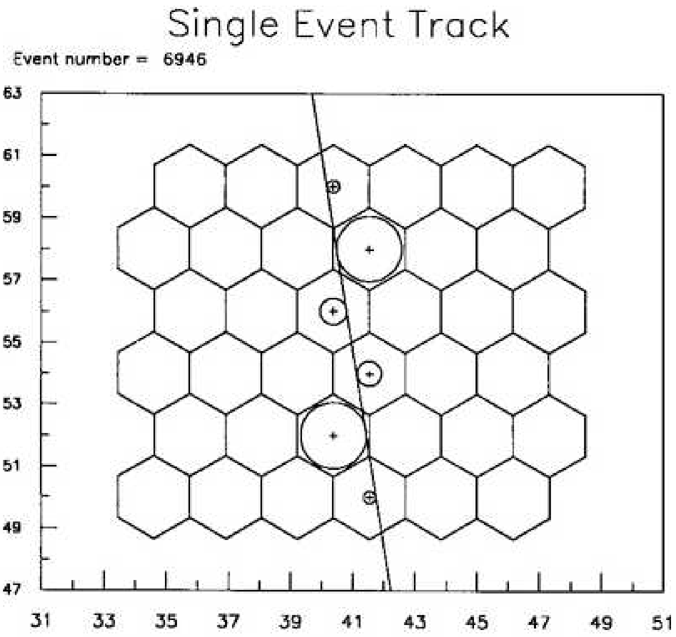

FIG. 14: A single track in a superlayer.Circles around the sense wires indicate the distance–of–closest–approach (DOCA).

There is no direct measurement of the event start time for the electron scattering experiments in CLAS, but it can be reconstructed from the measured flight time of the scattered electron and the path length as determined by the DCs. The scattered electron is identified using the electromagnetic calorimeters (section 3.2.3) and the Čerenkov counters (section 3.2.2). The signals in the TOF counters (section 3.2.4) corresponding to the electron and the electron path calculated by the tracking code are used to obtain the start time

$$t_{start} = t_{tof} - \frac{l}{\beta c}, \tag{40}$$

where t_{tof} is the time obtained from the electron signal in the SC, l is the length of the electron path from the interaction vertex to the scintillators, and c is the speed of light. Since electrons are highly relativistic, $\beta = v/c$, where v is the particle (electron) speed, is equal to 1. The TOF system resolution varies between 80 ps and 160 ps, which affects the start time determination. The electron beam arrives at the target in bunches with $\sim$ 2 ns delay between each subsequent bunch. In the case of perfect time of flight resolution, the start time given by eq. [40] should correspond to the arrival time of one of those electron bunches. However, the time of flight resolution is not perfect and therefore, a correction term should be introduced to eq. [40] as shown in the expression

$$t_{start} = t_{tof} - \frac{l}{\beta c} + t_{RF} \tag{41}$$

where t_{RF} is the time difference between the reconstructed start time and arrival time of the closest bunch.

3.6 EG1 DATA

The EG1 experiment, as previously mentioned, consists of two run periods, EG1a and EG1b, which ran in the fall of 1998 and from September 2000 to April 2001, respectively. In this work the ND_3 data collected during the EG1a experiment are analyzed. A list of all the data including the NH_3, Carbon (C) and Helium (He) runs is given in Table II. Data on the C and He targets are used for background subtraction.

The runs with the positive torus current are named *inbending* runs since the torus field bends the negative particles towards the beam line. Similarly, the negative particles are bent away from the beam line for the so–called *outbending* runs with negative torus polarity. The inbending and outbending runs have different Q^2 and W coverage. As indicated in Fig. 15, the Q^2 range provided by the inbending runs starts from ~ 0.25 GeV^2 and its tail extends slightly over 1.5 GeV^2, while the outbending runs yield the lower Q^2 region.

3.7 POLARIZED TARGET

The first experiments using polarized targets at Saclay [55], at low energy, and at the Lawrence Berkeley Radiation Laboratory (LBNL) [56], at high energy, were performed in the early 1960s.

Today, highly polarized targets with resistance to radiation damage are available thanks to developments in target materials, refrigerators and magnets. In the following sub–sections the polarization mechanism and the polarized target used for the EG1 experiment will be described.

TABLE II: Run summary of the EG1a run period. In this work only the ND_3 runs are analyzed. The positive torus current values represent the magnet polarity that bends the negative particles towards the beam line, while the negative torus current bends them away from the beam line.

Beam Energy (GeV)	Target Type	Torus Current (A)	Target Polarization
2.562	ND_3	-1500	> 0
2.494	ND_3	-1500	> 0
2.565	ND_3	$+2250$	> 0
2.494	ND_3	$+2250$	> 0
2.494	ND_3	$+2250$	< 0
2.562	NH_3	-1500	> 0
2.562	NH_3	-1500	< 0
2.562	NH_3	-1930	> 0
2.565	NH_3	$+1500$	> 0
2.565	NH_3	$+1500$	< 0
2.565	NH_3	$+2250$	> 0
2.565	NH_3	$+2250$	< 0
4.278	NH_3	-2250	> 0
4.278	NH_3	-2250	< 0
4.239	NH_3	$+1930$	> 0
4.278	NH_3	$+1930$	< 0
4.068	NH_3	$+1930$	> 0
4.068	NH_3	$+2250$	> 0
4.278	NH_3	$+2250$	< 0
4.278	NH_3	$+2250$	> 0
4.278	NH_3	$+2250$	< 0
2.562	C	-1500	0
2.565	C	$+2250$	0
2.565	He	$+2250$	0

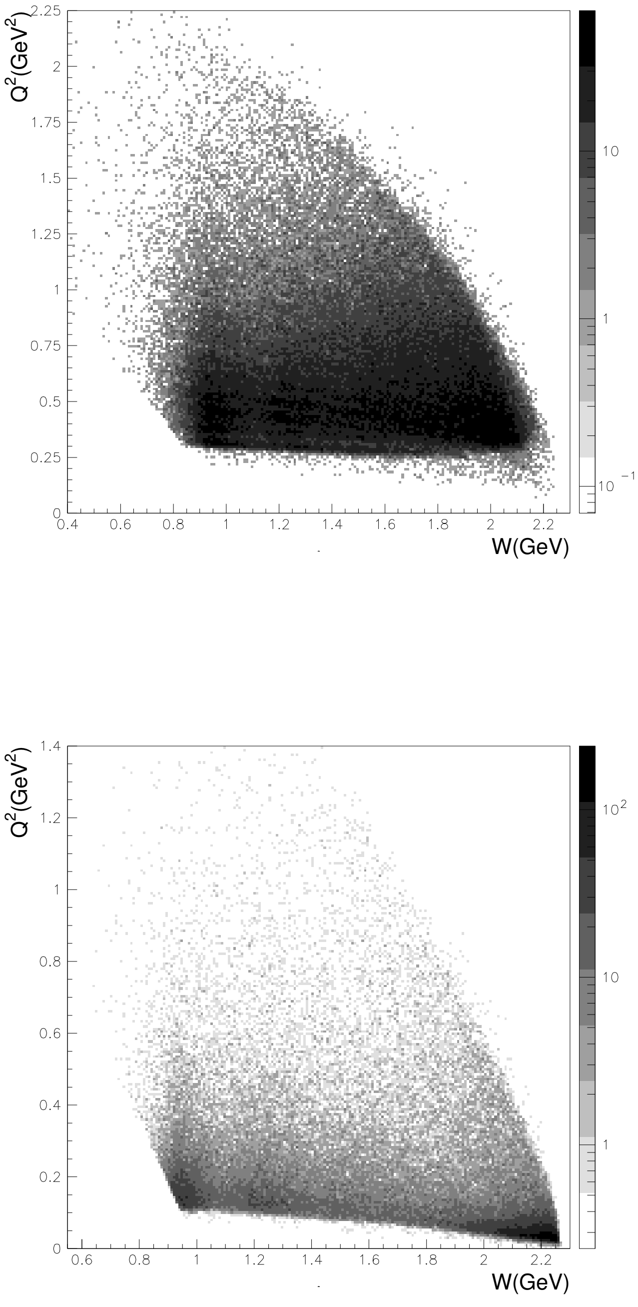

FIG. 15: Q^2 versus W distribution for the inbending (top) and the outbending (bottom) runs.

3.7.1 Polarization Mechanisms

Spin polarization of particles, such as the electron or the nucleon, involves the interactions of their magnetic moment μ with an external magnetic field $\mathbf{B}$. This interaction, the Zeeman effect, produces a set of $2I+1$ sublevels, where $I = 1/2$ for protons and 1 for deuterons. At thermal equilibrium (TE), the Boltzmann law describes the population of two magnetic sublevels as

$$N_1 = N_2 \mathrm{exp}(\frac{-\Delta E}{k_B T}), \tag{42}$$

where $\Delta E = -(\mu/I)B(m_1 - m_2)$, T is the temperature of the system, k_B is the Boltzmann constant, and $N_{1,2}$ are the number of nuclei in the magnetic sublevels. The polarization of a spin–1/2 system is characterized by the average value of the particle spin and it is denoted by

$$P(1/2) = \frac{N_{1/2} - N_{-1/2}}{N_{1/2} + N_{-1/2}}, \tag{43}$$

while the vector polarization of a spin–1 system is given by

$$P(1) = \frac{N_1 - N_{-1}}{N_1 + N_0 + N_{-1}} \tag{44}$$

where, in all cases, N_x represents the number of particles with magnetic quantum number $m_I = x$. The polarization of protons $P(1/2)$ and deuterons $P(1)$ at thermal equilibrium can then be written as

$$P(1/2) = \tanh(\frac{\mu\mathbf{B}}{k_B T}), \qquad P(1) = \frac{4\tanh(\frac{\mu\mathbf{B}}{2k_B T})}{3 + \tanh^2(\frac{\mu\mathbf{B}}{2k_B T})}. \tag{45}$$

Electrons have a large magnetic moment ($\mu_e = 660\mu_p$) and therefore, in a magnetic field of 2.5 Tesla and at a temperature of 1 K, they reach a polarization of 92% and even higher (over 99% at $T = 0.5$ K). However, under the same conditions ($B = 2.5$ T and $T = 1$ K) only a polarization of 0.25% for protons and 0.05% for deuterons can be achieved due to the very small magnetic moments of the protons and the deuterons [57]. Those values of polarization are clearly very small and are not very useful for nuclear and particle physics experiments.

Higher nucleon polarization can be achieved by using an extremely high magnetic field and a very low temperature such that the ratio $\mathbf{B}/T$ is a maximum. The highest $\mathbf{B}/T$ ratio ever reached is 1700 Tesla$\cdot$ K^{-1}, which corresponds to a magnetic field of 17 Tesla and a temperature of 10 mK [58] and gives 94% proton polarization. On the other hand, the disadvantages of this technique in electron scattering experiments are the negative effects of the high magnetic field on detector operation and difficulty in having very low temperatures in such experiments. Dynamic nuclear polarization (DNP), which was used for the EG1 experiment, is a more complex but more successful technique to enhance the nucleon polarizations for electron scattering experiments.

The main idea of DNP is to transfer the high electron polarization at low temperature ($\sim$ 1 K) and high magnetic field ($\sim$ 5 Tesla) to the nuclei using a microwave field. This method requires a high concentration of polarizable nucleons lightly doped with paramagnetic centers, such as free electrons, which are introduced either by chemical or radiation methods to provide unpaired electron spins. In the theoretical description, the hamiltonian describing the system has a perturbation term due to the spin–spin interaction between the nucleon and the unpaired electron spins, and new eigenstates of the system are given by a linear combination of the *free* hamiltonian eigenstates as shown in Fig. 16. Applying an RF field with a frequency equal to the sum ($\omega_e + \omega_p$) or difference ($\omega_e - \omega_p$) of the Larmor frequencies of the two interacting systems (ω_e = 140 GHz and ω_p = 213 MHz at 5 Tesla) induces transitions in which both spins are flipped. This way the high electron polarization can be transferred to the proton. Since the relaxation time (the time for the spin to flip back to the lower energy state) for the nucleon or deuteron spin is much longer than for the electron spin, after the double spin transition the electron decays back to its original state and will be used for a second transition, while the nucleon will remain in its new state much longer. The relaxation time for the electron is $\sim$ 1 ms, while it is $\sim 10 - 100$s minutes for the proton. Using this technique a polarization of 80–90% for protons and 30–40% for deuterons can be achieved.

The main problem with the DNP is finding a suitable combination of hydrogen– or deuterium–rich material and a paramagnetic dopant with unparied or quasi–free electrons. Molecular hydrogen and deuterium would be ideal as proton and deuteron (neutron) targets, but at low temperatures, those *clean* samples convert to the magnetically inert para–state, with spin zero, and therefore, are unpolarizable. For this reason, polarized target materials with paramagnetic centers introduced are used for the DNP. A list of such materials can be found, for instance, in Ref. [57].

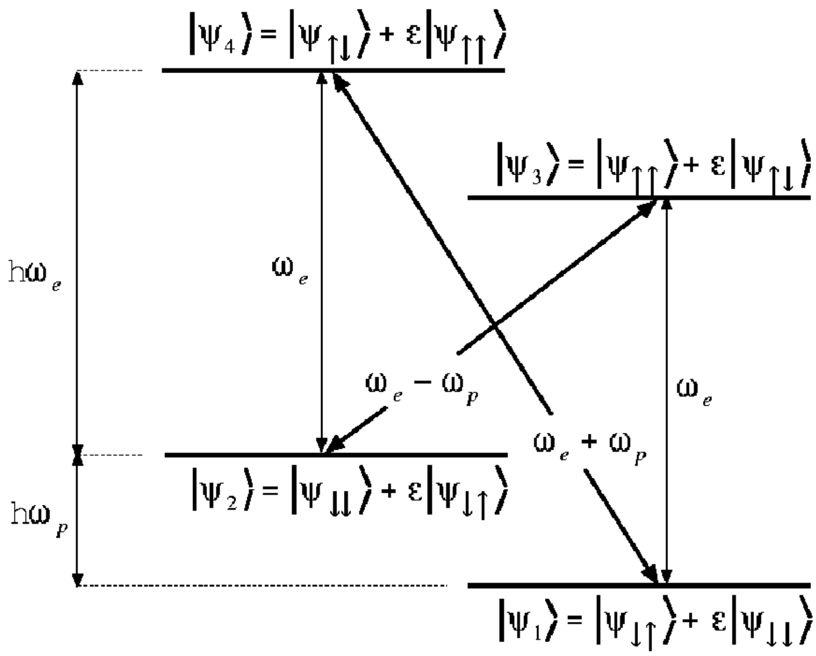

FIG. 16: Energy level diagram of an electron and proton pair. The first arrow on the left in each subscript indicates the electron spin, while the second one denotes the proton spin. The transitions from $|\Psi_1>$ to $|\Psi_4>$ and from $|\Psi_2>$ to $|\Psi_3>$ are possible by the microwaves of frequencies $\omega_e + \omega_p$ and $\omega_e - \omega_p$ [59].

3.7.2 The CLAS Polarized Target

In order to build a polarized target for the CLAS, several constraints had to be taken into account. Among them are the limited space available in the center of the CLAS for the target insertion, the local heating produced by the electron beam and corresponding radiation damage on the target material, and the necessity of large scattering windows for the outgoing particles. A drawing of the polarized target used for the EG1 experiment is shown in Fig. 17.

Two sets of superconducting magnet coils, which provide a 5 Tesla magnetic field parallel or anti–parallel to the direction of the beam, are azimuthally centered on the beam axis and the target chamber is located in the center of the two coils. The liquid helium bath is supplied by the refrigerator angled at 30° to the beam axis. The target cells maintained in the helium are inserted into this region via a vertical tube.

This configuration of the magnet is useful for many reasons. Firstly, the magnetic field at the axis is completely longitudinal, and hence, the incident electrons are not

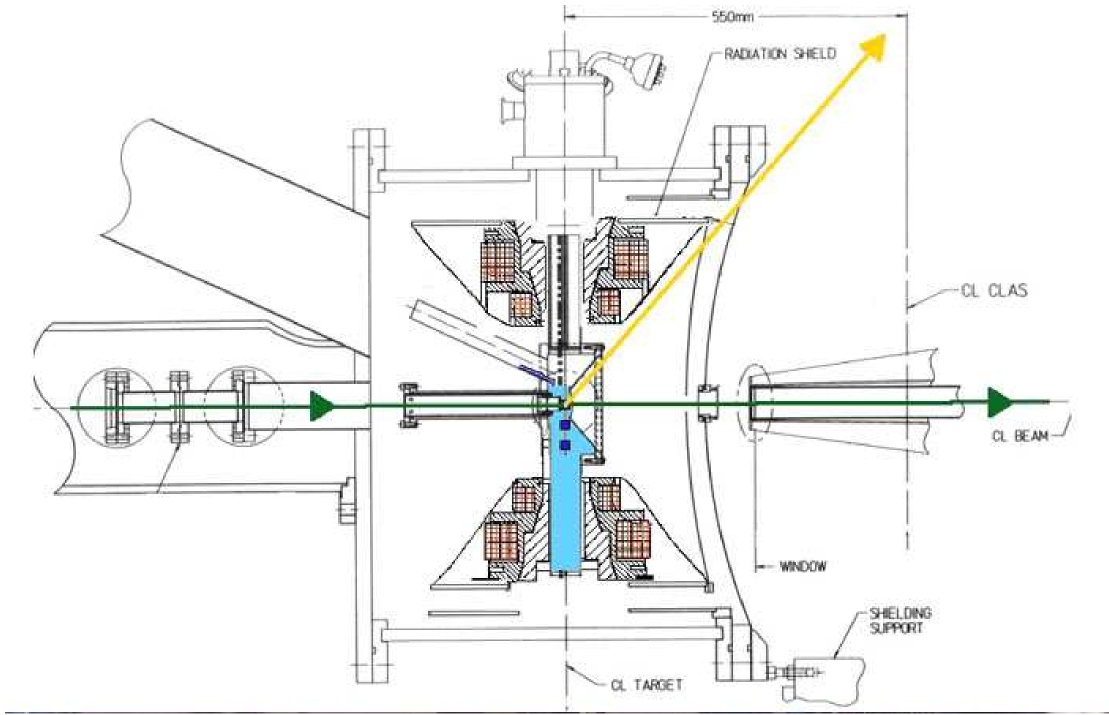

FIG. 17: A cross–section view of the EG1 polarized target along the beam direction. Beam direction is shown with a horizontal arrow at the center of the drawing. The two magnet coils are azimuthally placed around the beam and indicated with hatched squares around the target central line (abbreviated as CL).

deflected by the magnetic field. Secondly, a uniform field at the target region is produced, which is needed for the proper functioning of the DNP process. Lastly, the magnet protects the drift chambers from the low energy electrons produced by Møller scattering inside the first region drift chambers by deflecting them towards the forward hole where no detector element exists. The magnet system is cooled down using liquid helium at 4.2 K. Some characteristics of the 5 Tesla magnet are shown in Table. III.

A cylindrical hole of 200 mm in diameter located in the center of the magnet houses the target material. The target sample is inserted into this bore, which is called *banjo* due to its shape, through a stainless–steel tube. The banjo is filled with liquid helium and cooled down to ~ 1 K by a ^{4}He evaporation refrigerator. During this process, liquid ^{4}He is transferred from the magnet buffer dewar to a separator pot where the liquid and vapor phases are separated by a sintered copper plate. The pressure in the separator is around 600 mbar, and therefore, the helium is pre–cooled

TABLE III: Some characteristics of the 5 Tesla superconducting magnet.

Maximum central magnetic field	5.1 Tesla
Current for full field	123.646 A
Field/Current	0.04125 Tesla/A
Central bore diameter	200 mm
Nominal inductance	61.7 H

to $\sim$ 3.5 K. The cold vapor is pumped out and used to cool the radiation shields, while the liquid phase is collected at the bottom of the pot, where it flows into a heat exchanger and finally fills the target holder via two needle valves. The incoming warm liquid is cooled when the outgoing cold vapor exhanges heat. The temperature in the banjo is reduced to $\sim$ 1 K by pumping on the helium vapor.

In order to enhance the target polarization using DNP, a microwave field of $\omega_e+\omega_p$ or $\omega_e-\omega_p$ needs to be provided to the system. This field is driven to the target material by a system of rectangular and circular wave guides and the target irradiation is performed by a trumpet connected to the end of this wave guide system.

The target polarization is measured by the nuclear magnetic resonance (NMR) method, using a Q–meter technique [60]. The polarization P is given by [61]

$$P \sim \int_0^\infty d(\omega)\chi''(\omega) \tag{46}$$

where ω is the angular frequency of the applied rf field and $\chi''(\omega)$ is the absorptive part of the complex nuclear susceptibility, $\chi(\omega) = \chi'(\omega) - i\chi''(\omega)$, which is non–zero only in a small range of frequencies around the Larmor frequency of the nucleon or the deuteron.

The whole or part of the polarized target material is contained in a coil of inductance L_C and a resistance r_C. The coil is then connected to a capacitor C and a damping resistance R to form a series LRC circuit. The target material modifies the inductance L_C. The change in the inductance causes a change in the circuit impedance. If the circuit is driven by a frequency synthesizer V_0, which sweeps the rf frequency ω through the Larmor resonance, the target material either absorbs or emits energy, which causes an inductance change in the coil, and consequently an impedance change in the circuit. If the current is kept constant, this impedance change is proportional to a complex voltage $V(\omega,\chi)$ whose real part is selected by a phase sensitive detector (PSD). The voltage is a superposition of the signal proportional to χ and the so–called Q–curve, $V_Q = V(\omega,\chi = 0)$, which is measured by setting the magnetic field such that $\chi''(\omega) = 0$ and χ' is negligible for the entire frequency scan. Then, the two signals are subtracted to result in $S(\omega) \sim \chi''(\omega)$ and the polarization is approximated by

$$P = \mathcal{K} \int_{\omega_l}^{\omega_u} d(\omega) S(\omega) \tag{47}$$

where $\mathcal{K}$ is a constant to be determined by a thermal equilibrium (TE) calibration of the system, and ω_l and ω_u are the lower and upper limits, respectively, of a small frequency range around the Larmor frequency of the target material.

In the EG1 experiment, polarized deuterons ($^{15}ND_3$), along with polarized protons ($^{15}NH_3$), made of frozen ammonia beads were used as the target material. A method of extracting the Q–curve from deuteron NMR signals is discussed in Ref. [62]. We used a rough analysis of the Q–curve on–line to monitor the deuteron polarization during the experiment. However, more reliable values for the deuteron polarization were extracted from the elastic scattering data. This method will be described in section 4.8.5.

The central bore of the magnet, filled with liquid helium, houses an aluminum insert containing four target cells (see Fig. 18). The cells, 1 cm thick and 1.5 cm in diameter, are made of 0.2 mm thick plastic material that has a good resistance to radiation damage and has no polarizable molecules that can negatively affect the NMR measurement. The two upper cells contain the NH_3 and ND_3 targets, while one of the remaining two cells contains a 2.2 mm thick graphite disk for background measurements. The last cell, which is also used for background measurements, is only filled with the 1 K liquid helium that surrounds each target. During operation, the insert could be moved in the vertical direction by a remotely controlled stepping motor and the selected target cell (any of the four) could be placed on the beam axis. The NMR coils were wrapped around the NH_3 and the ND_3 targets. Sensors were placed in different locations on the insert to measure the temperature in that region.

The CLAS polarized target was located ~ 60 cm upstream from the CLAS center, which allowed the detection of electrons scattering at small angles. This consequently provides a better coverage at low Q^2. All the target components, including the magnet, the microwave system, the helium supply, and the NMR system were remotely controlled via an Epics interface (for the cryogenic part) and a Labview–based system (for the magnet, NMR and microwave controls).

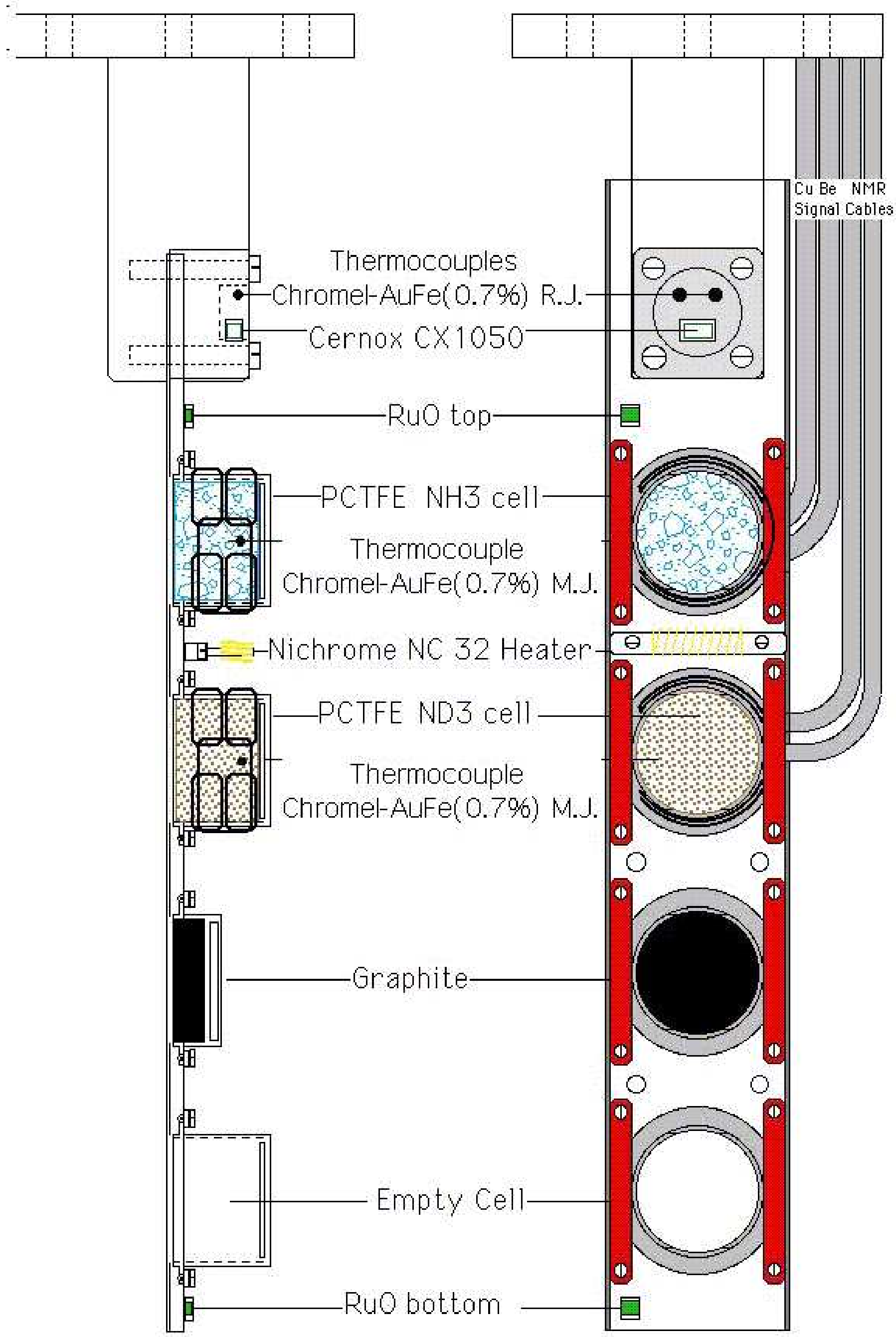

FIG. 18: Side and front view of the target stick. The four target cells, NH_3, ND_3, ^{12}C and empty, were placed on the insert from top to bottom, respectively.

CHAPTER 4

DATA ANALYSIS

The raw CLAS data (ADC and TDC values for each detector that had a hit) are stored on tape to be processed and converted into meaningful physics quantities via RECSIS (CLAS reconstruction software). Before a massive processing, a sample of about 10% of the whole data, selected uniformly throughout the entire data, is processed in order to perform a calibration of each detector component. This is needed for each run period to take into account any modification due to different running conditions or any change in the detector response. Full data processing, so–called *cooking*, starts after obtaining satisfactory results from the calibration of each detector element. Online monitoring is done during the processing to check the quality of the data and the results are summarized in a database.

4.1 PARTICLE IDENTIFICATION

The detection of charged or neutral particles is possible with the CLAS detector using one or more detector components. Even though the candidates for these particles are determined during the reconstruction process, a much finer determination can be made at the level of physics analysis by introducing additional constraints, which are called *cuts*. In the following, the cuts used for electron and π^- identification are discussed.

4.1.1 Electron Identification

In the CLAS Simple Event Builder (SEB), which is part of the RECSIS data analysis framework, the minimal requirements for a hit and track to be an electron candidate are having a negative track and shower in the electromagnetic calorimeters [63]. For EG1, a hit in the Čerenkov counter and the electromagnetic calorimeter in coincidence was required for the trigger. However, the EC and CC hits may not have been caused by the same particle and even low energy pions will sometimes cause a signal in the CC. The events that do not include an electron candidate are rejected during the reconstruction process. In some cases, electron identification may fail due to the negatively charged pions being misidentified as electrons. In order to minimize the

Sector no	ϕ range	a
1	–30 to 30	0.265
2	30 to 90	0.265
3	90 to 150	0.265
4	150 to 180 & –180 to –150	0.265
5	–150 to –90	0.297
6	–90 to –30	0.275

TABLE IV: Sector dependent values of the constant a.

misidentification, more strict cuts on EC and CC signals need to be applied.

When electrons interact with the EC material, they produce showers and release energy in the calorimeters. The fraction of this electromagnetic shower energy which is deposited in the scintillators, and is thus detectable, is called the sampling fraction (see Fig. 19). The sampling fraction depends on the details of the Pb/Scintillator sandwich mentioned in section 3.2.3 and has a value of ~ 0.27 for the CLAS calorimeters. Pions, on the other hand, are minimum ionizing and tend to deposit the same energy in the calorimeter regardless of the pion momentum. A safe region where the total deposited energy and kinetic energy proportionality is maintained and the leaks due to the hits close to the calorimeter edge are excluded is defined as

$$a(-0.05 + P + 0.3\sqrt{P}) > E_{total} > a(-0.05 + P - 0.3\sqrt{P}), \tag{48}$$

where E_{total} is the total energy deposited in the calorimeter, a is a sector–dependent constant and P is the momentum of the particle. The plot at the bottom in Fig. 19 shows the electron candidate events after the cut mentioned is applied. The definition of each sector in terms of the azimuthal angle ϕ and the values of the constant a for each sector are given in Table IV.

The energy deposited in the inner and outer stack of the EC are named E_{inner} and E_{outer}, respectively. Contamination by minimum–ionizing particles, such as pions, can be viewed in the E_{total} vs. E_{inner} plot at E_{inner} below 50 MeV as shown in the top plot of Fig. 20. The plot at the bottom in the same figure shows the same distribution with the cuts $E_{inner} > 50$ MeV and $E_{total} > E_{inner}$ applied.

The signals in the Čerenkov counters (see section. 3.2.2) are also used to distinguish electrons from pions. A distribution of the number of photo–electrons produced

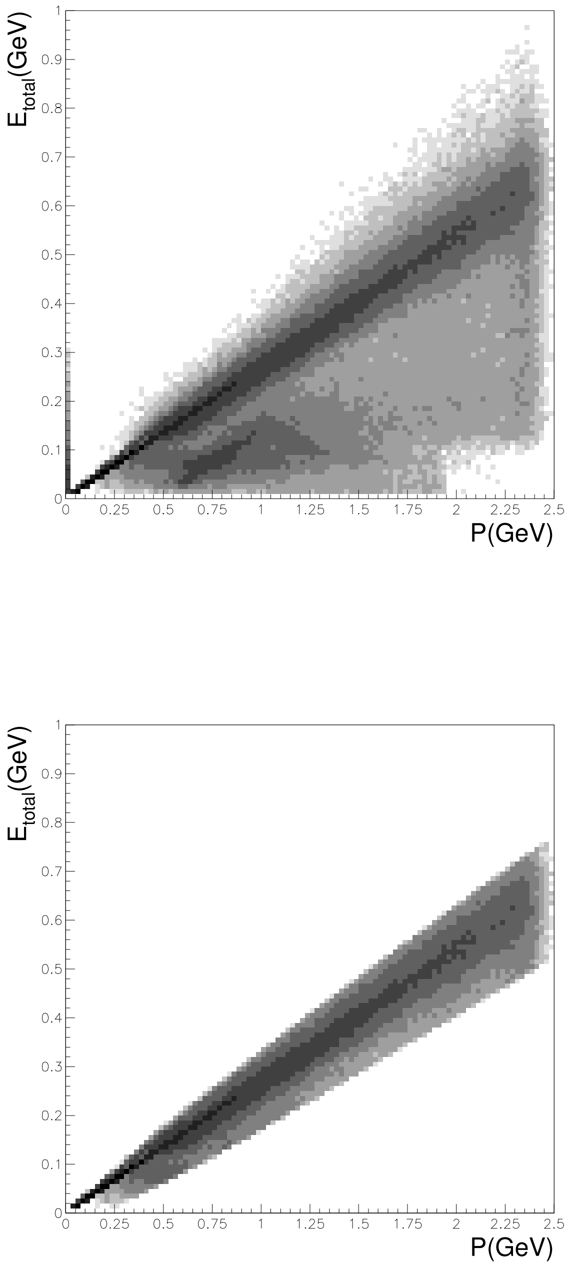

FIG. 19: The total energy E_{total} deposited in the EC is plotted versus the particle momentum P before and after the electron cut is applied.

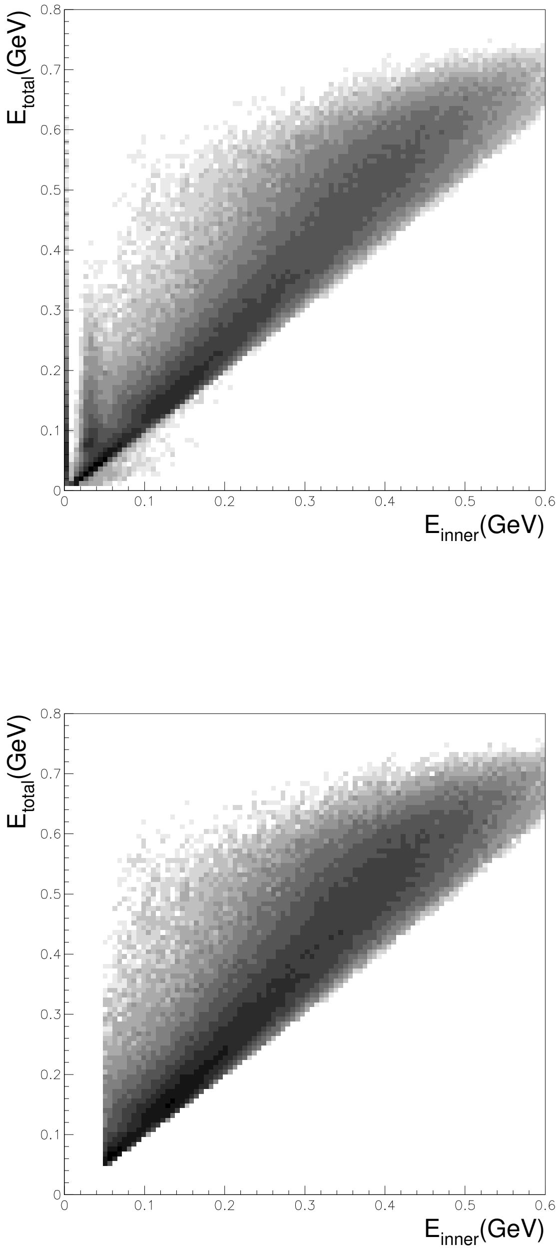

FIG. 20: The total energy E_{total} deposited in the EC versus energy deposited in the inner EC stack (E_{total} versus P cut is not included). The contamination due to the minimum–ionizing particles is minimized with the cut applied (bottom).

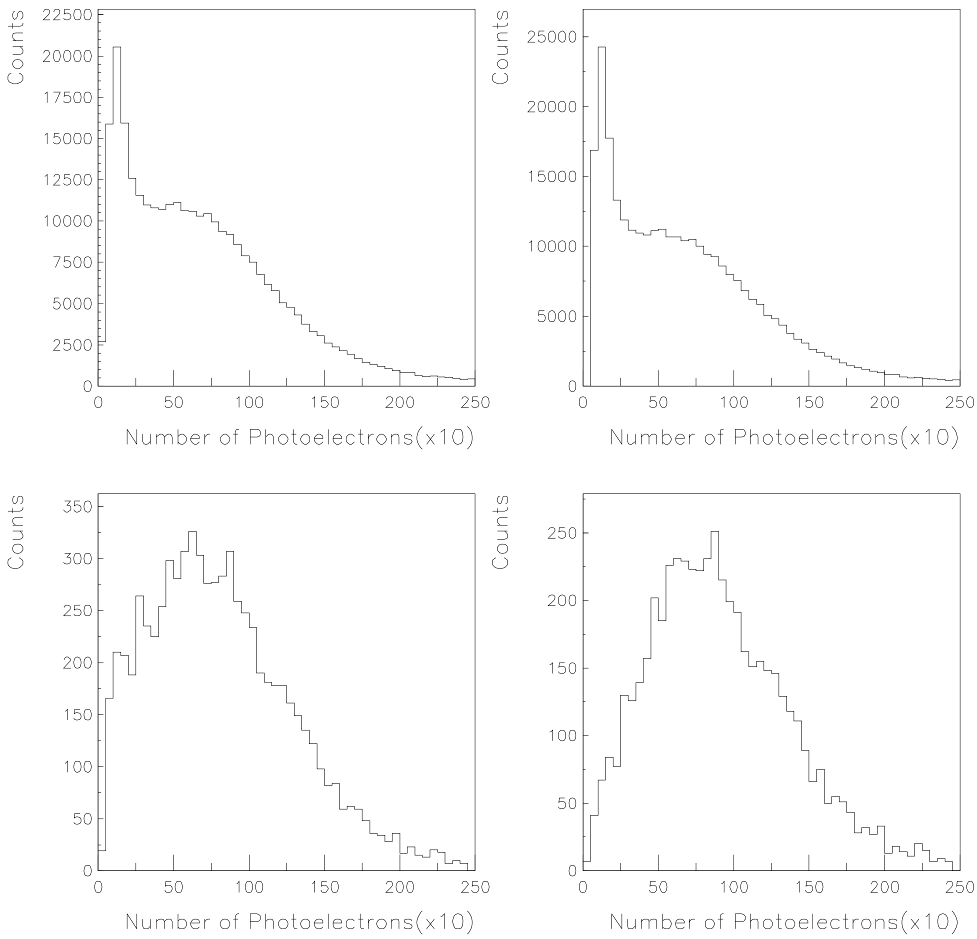

FIG. 21: A distribution of the number of photo–electrons (nphe) produced by the Čerenkov light for all electrons (SEB particle identifier = 11) before (top–left) and after (top–right) the nphe cut is applied. The bottom–left and bottom–right plots illustrate the nphe distribution for the $en \to e'\pi^- p$ channel with the loose and tight fiducial cuts applied, respectively (these plots do not include previously mentioned E_{total} vs. P and E_{total} vs. E_{inner} cuts).

by the Čerenkov light is shown in the top–left plot in Fig. 21. The peak at ~ 1 photo–electron is mainly due to the bad collection of the Čerenkov light by the Čerenkov PMTs, which shows up as fringes in the θ versus ϕ distribution for the electrons. The peak can mostly be eliminated by requiring the number of photo–electrons (nphe) to be greater than ~ 2. However, by applying that cut some electrons are also lost. Since the reaction being studied, $en \to e'\pi^- p$, requires the detection of another negative particle, the π^-, along with an electron, therefore decreasing the probability of any further pion contamination, the minimum number of photo–electrons required can be reduced to 0.5 for the present work. The applied nphe cut only eliminates a small fraction of the peak (see top–right plot in Fig. 21). The remaining peak is then eliminated by applying a set of $fiducial$ cuts (see section 4.2), where any low efficiency region due to the holes in the detector system or the fringes created by the Čerenkov counters is excluded. The bottom–left and bottom–right plots in Fig. 21 indicate the distribution of the number of photo–electrons for the $en \to e'\pi^- p$ channel with the application of *loose* and *tight* fiducial cuts, respectively (see section 4.2). The peak at ~ 1 photo–electron clearly disappears.

4.1.2 π^- Identification

In SEB, charged particles are identified using the SC time and the track momentum provided by the drift chambers. EC timing is used when there is no SC hit involved. The time and momentum information is used to calculate the β of the particle

$$\beta = \frac{l}{tc}, \tag{49}$$

where l is the path length from the target to the SC, t is the time of flight to that point and c is the speed of light. After β for the charged particle is calculated according to eq. [49], the particle identification (PID) is performed based on the selection of the particle whose mass yields the closest β calculated as

$$\beta = \frac{P_{track}}{\sqrt{P_{track}^2 + m_{particle}^2}}. \tag{50}$$

In this equation, P_{track} is the momentum and $m_{particle}$ is the mass of the particle (see Table V for a list of particles and their identifiers.)

The neutral particles given in the table, such as photons and neutrons, are defined by the hits in the electromagnetic calorimeters that did not have corresponding hits

TABLE V: List of particles included in the SEB.

Particle	SEB Identifier	Mass (GeV)
electron	11	0.0005
positron	-11	0.0005
photon	22	0.0
π^+	211	0.1396
π^-	-211	0.1396
k^+	321	0.494
k^-	-321	0.494
proton	2212	0.9383
neutron	2112	0.9396
deuteron	45	1.8756
^{3}He	49	2.8092
^{4}He	47	3.7274

in the CC and SC. Since they have no charge, they are not affected by the torus magnetic field, and therefore, their path length is simply the distance between the vertex and the EC hit position. Hits with a β equal to 1 within 5% are assumed to be photons; a neutron otherwise. For the particles with a momentum below 1.5 GeV, the electromagnetic calorimeters have a good resolution for photon–neutron discrimination.

A correct identification of the π^- in this analysis is as important as the identification of the electrons mentioned in the previous section since the π^- is also detected along with the e^-. The top plot in Fig. 22 shows the β versus momentum distribution for the π^- using -211 as the particle identifier in SEB. In this case, some pions are misidentified as negatively charged kaons (k^-) usually because of a bad paddle timing calibration and they are left out. For this reason, in this study, instead of using PID $= -211$ to select pions, a cut excluding all the positively charged (PID $= -11$,211,321,2212), neutral (PID =22,2112) and relatively heavy particle candidates (PID = 45,47,49), along with the electrons (PID= 11), was made to identify pions. The plot at the bottom in Fig. 22 shows the β versus momentum distribution with the mentioned cut applied. The band around $\beta = 0.9$ shows the saved π^- candidates.

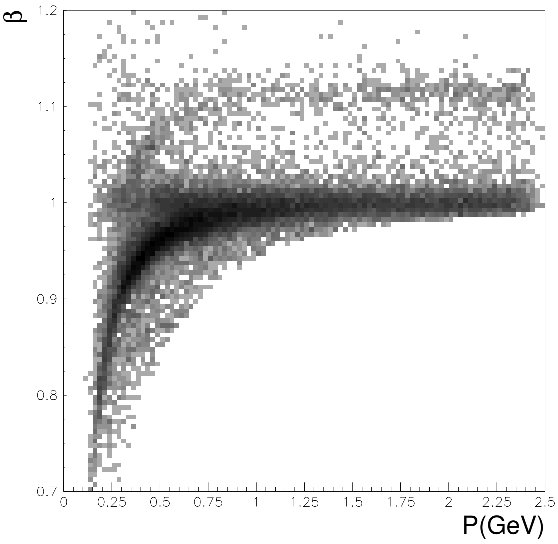

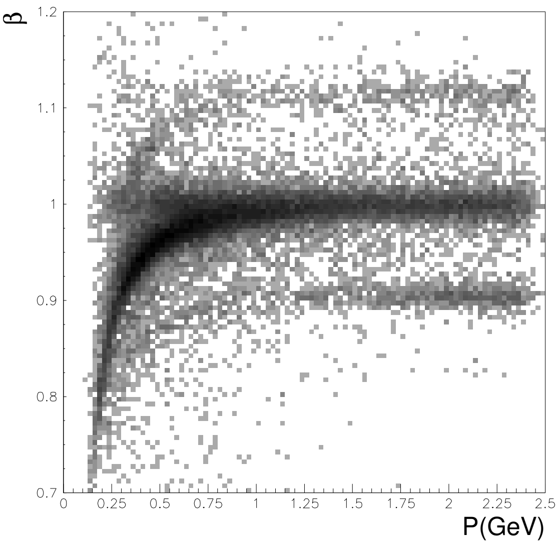

FIG. 22: β versus momentum distribution for π^- using PID $= -211$ (top) and using the cut mentioned in the text (bottom). The bands around $\beta = 1.1$ and 0.9 are due to bad paddle timing calibration.

4.2 FIDUCIAL CUTS

CLAS is not a perfect 4π detector. It has gaps and low efficiency regions that have to be taken into account for a careful analysis. The six superconducting magnetic coils, the beam entrance and exit holes, the edges of the Čerenkov counters and the dead drift–chamber wires are among the main reasons for zero or low efficiency regions. The ϕ versus θ distribution at the reaction vertex in Fig. 23 illustrates these inefficient regions of the detector as fringes or depletions.

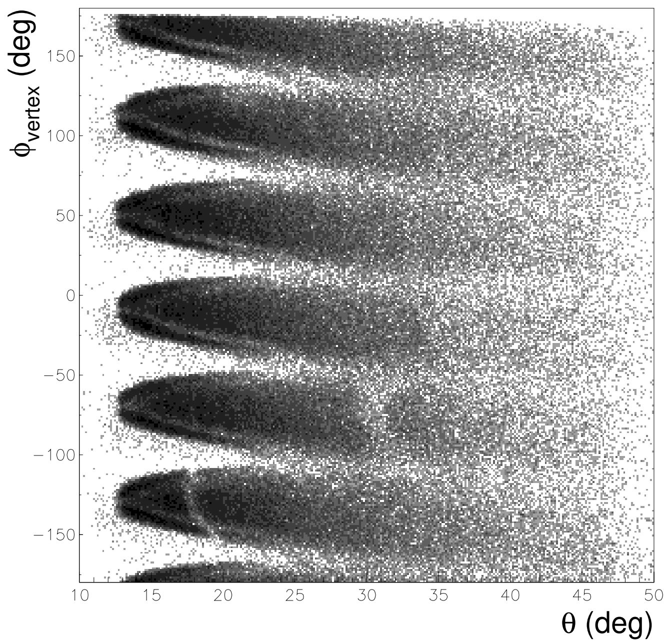

FIG. 23: Electron ϕ_{vertex} versus θ distribution for the inbending runs. ϕ_{vertex} changes with increasing θ due to the shift in ϕ caused by the presence of the polarized target magnetic field.

For the unpolarized targets, there only exists the toroidal magnetic field to act upon the charged particles passing through the region 2 drift chambers (see section 3.2.1). In case of the polarized target used for the EG1 experiment, on the other hand, the polarized target produces an additional magnetic field along the direction of the beam. The magnetic field lines loop around opposite the beam direction outside

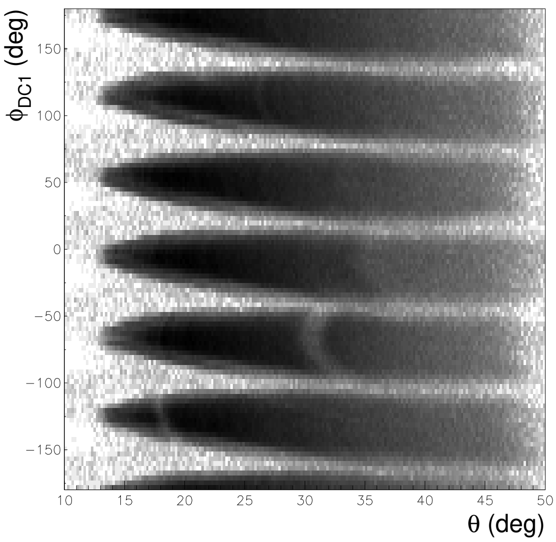

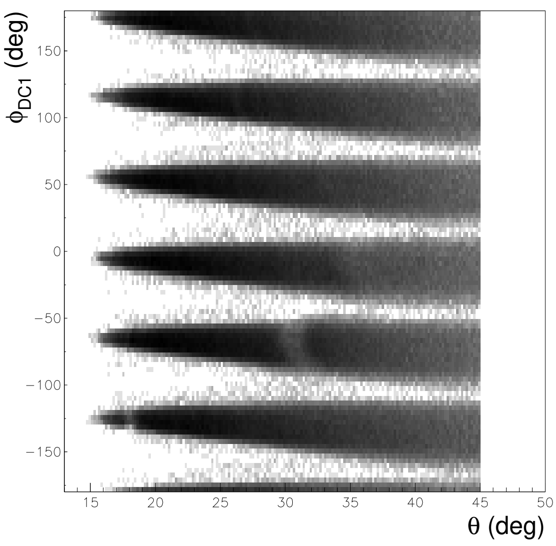

FIG. 24: Electron ϕ_{DC1} versus θ_{DC1} distribution for the inbending runs before (top) and after (bottom) the fiducial cuts are applied.

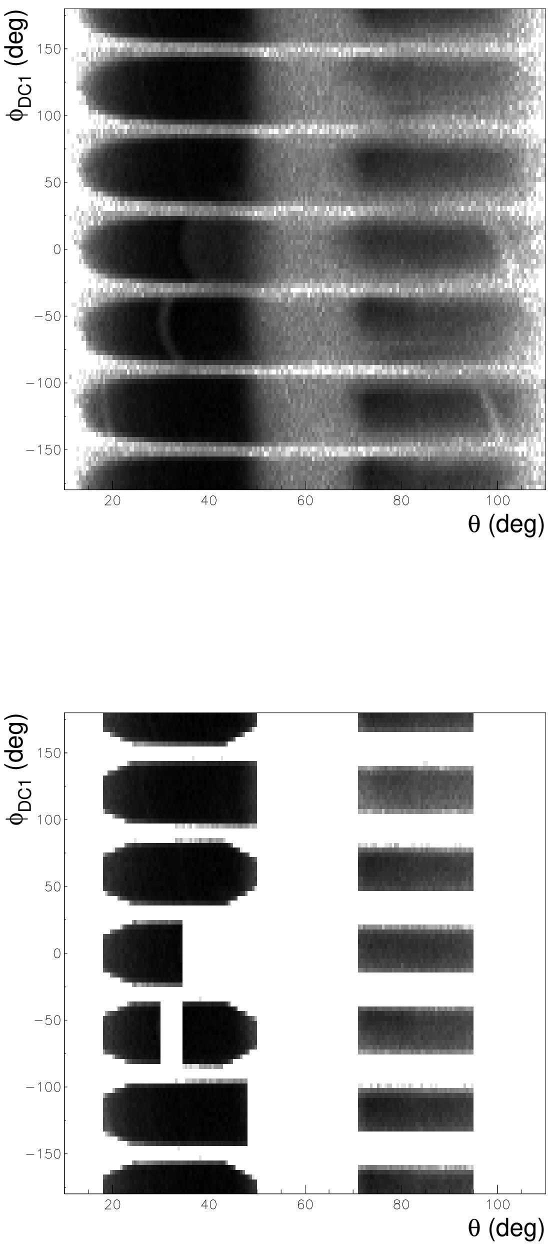

FIG. 25: Pion ϕ_{DC1} versus θ_{DC1} distribution for the inbending runs before (top) and after (bottom) the fiducial cuts are applied.

of the target region. This field produces a shift between the ϕ at the target (ϕ_{vertex}) and at the first drift chamber layer DC1 (ϕ_{DC1}). The ϕ_{vertex} versus θ_{vertex} distribution in Fig. 23 illustrates the fact that the shift is more pronounced with increasing θ. This behaviour is not seen at DC1. Therefore, ϕ_{DC1} is a good selection for study of the fiducial cuts.

Selection of the safe regions with close to 100% efficiency is performed by applying a set of fiducial cuts for each sector of the CLAS using the angles ϕ and θ at DC1. Two types of electron fiducial cuts, loose and tight, are applied to the data. These cuts are determined by fixing the momentum and θ of the particle and accepting the regions with a constant ϕ distribution. The loose cuts are less strict than the tight ones and allow some of the fringes at the edges of the Čerenkov counters. Therefore, in order to have better statistics, the final asymmetries are obtained using the loose electron fiducial cuts. Fig. 24 indicates the ϕ_{DC1} versus θ distribution before (top) and after (bottom) the tight fiducial cuts are applied.

Fiducial cuts for the negative pions have also been studied. The low efficiency regions of the drift chambers, dead TOF paddles and the polarized target coils were excluded in the pion fiducial cuts. Fig. 25 indicates ϕ_{DC1} versus θ_{DC1} distributions for the pions before and after the application of these cuts.

4.3 TARGET POSITION CORRECTION AND VERTEX CUT

In order to use only events in which electron scattered from the target, a cut is made on the z–coordinate of the vertex to minimize the contribution from electrons scattered from the non–target materials, such as the target entrance and exit windows. Because the beam is offset slightly from the symmetry axis of CLAS, the reconstructed vertex has a ϕ dependent distortion which can be seen in the top plot in Fig. 26. This shift is corrected, as shown at the bottom plot in the same figure, by introducing the function

$$A \cdot \mathrm{cotan}(\theta)\sin(\phi - \phi_0) \tag{51}$$

to the reconstructed vertex value. Here, A is the distance (in mm) between the beam and detector symmetry axes and ϕ_0 is the angle between the plane that is made by the beam and detector symmetry axes and the horizontal plane. Having corrected the vertex, a cut is made choosing the events within the vertex range of -61 and -50 cm as shown in Fig. 27. With this cut the window contributions at ~ -45 and

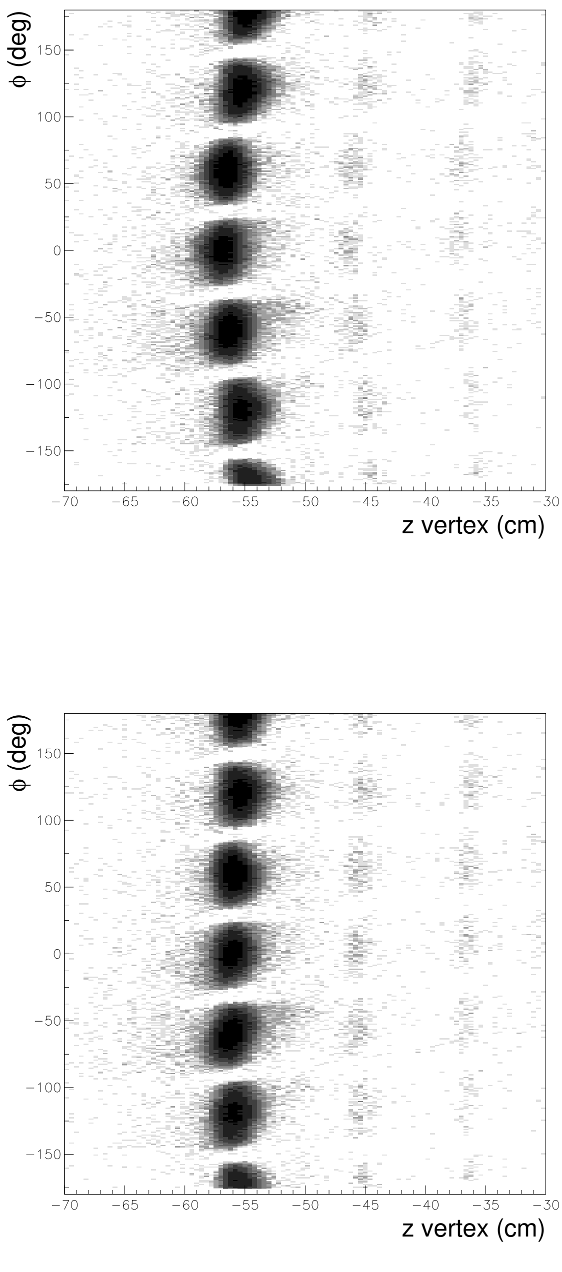

FIG. 26: ϕ versus z component of the vertex indicates a shift in reconstructed vertex (top). The plot at the bottom shows the same distribution with the corrected vertex. The shadows at ~ -45 and ~ -35 cm are due to the cryostat windows.

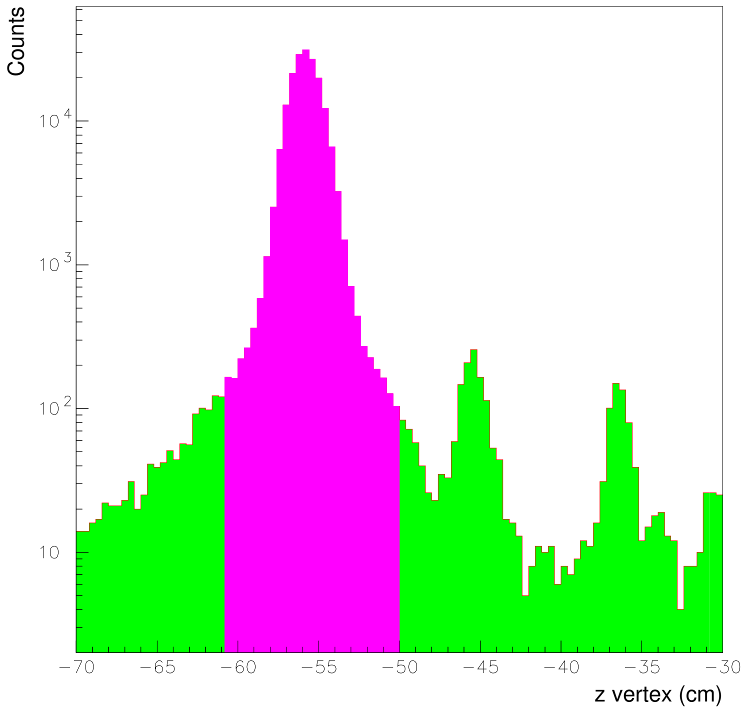

FIG. 27: Z component of the vertex. A cut between –61 and –50 cm is indicated. The cryostat windows are also clearly visible at ~ -45 and ~ -35 cm.

~ -35 cm are clearly excluded.

4.4 ACCEPTANCE CORRECTION

Even though, in general, the detector acceptance does not affect the inclusive asymmetries since it cancels out, a correction for the acceptance is required for exclusive asymmetries, integrated over kinematic quantities such as ϕ^*, since the numerator and denominator have different ϕ^* dependence. The integration is needed to increase the statistics.

The acceptance is calculated within the fiducial regions determined by the cuts mentioned in section 4.2. Single pion electro–production cross–sections and asymmetries are usually reported as a function of center–of–mass kinematic variables W, Q^2, θ^*, and ϕ^*. However, each event can be described by lab system quantities p_e, θ_e, θ_π and $\phi_\pi - \phi_e$, which are the electron momentum and polar angle, the pion polar angle, and the difference between the pion and electron azimuthal angles, respectively. The pion momentum p_π is a function of the other quantities. Only the electron azimuthal angle ϕ_e remains as a free variable. The acceptance is calculated by varying ϕ_e and determining for what fraction of the 2π phase space both the scattered electron and the emitted pion remain within the region defined by the fiducial cuts. See also Ref. [68] for more details about the acceptance calculation.

Fig. 28 indicates the acceptance for the outbending (top) and the inbending runs (bottom) within the fiducial regions. Each event is divided by its acceptance (acc) before asymmetries are constructed. The uncertainty in the number of counts in each bin was calculated as $\frac{\sqrt{N}}{acc}$. For the inbending runs, an acceptance cut $acc \geq 0.05$ was applied.

4.5 ELECTRON MOMENTUM CORRECTIONS

The electron momentum, as well as other charged particle momenta, is calculated using the reconstructed track from the drift chambers and the torus magnetic field. The quality of the reconstruction can be checked by studying the elastic peak in the W spectrum. Because of the non–perfect description of the drift chamber position in the tracking code and small differences between the actual torus magnetic field and the constants in the database, the electron momentum is miscalculated and this causes the elastic peak to appear in the wrong position compared to the theoretical value ($W_{elastic} = 0.939$ GeV). The correction is performed adjusting the reconstructed electron momentum by the following expression [68]:

$$p_{corrected} = p_{measured}(a + b\phi + c\phi^2)\frac{d\theta - e}{f\theta - g}, \tag{52}$$

where a, b, c, d, e, f and g are the parameters fitted to the data using the correct W elastic peak position as a constraint.

The results shown in Fig. 29 were obtained using the 2.565 GeV beam and 2250 A torus current. The plots indicate the W spectra with (left plot) and without the nitrogen contribution (right plot) obtained by using the reconstructed (line) and the

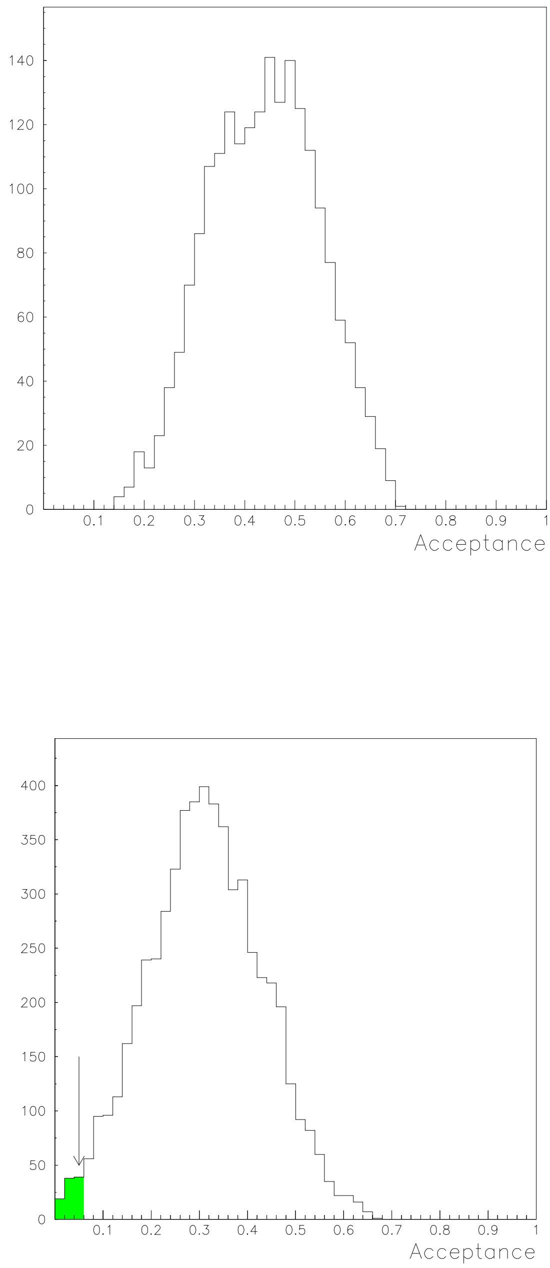

FIG. 28: Acceptance for the outbending (top) and inbending runs (bottom). The shaded region in the bottom plot indicates the events rejected by the acceptance cut ($acc \geq 0.05$).

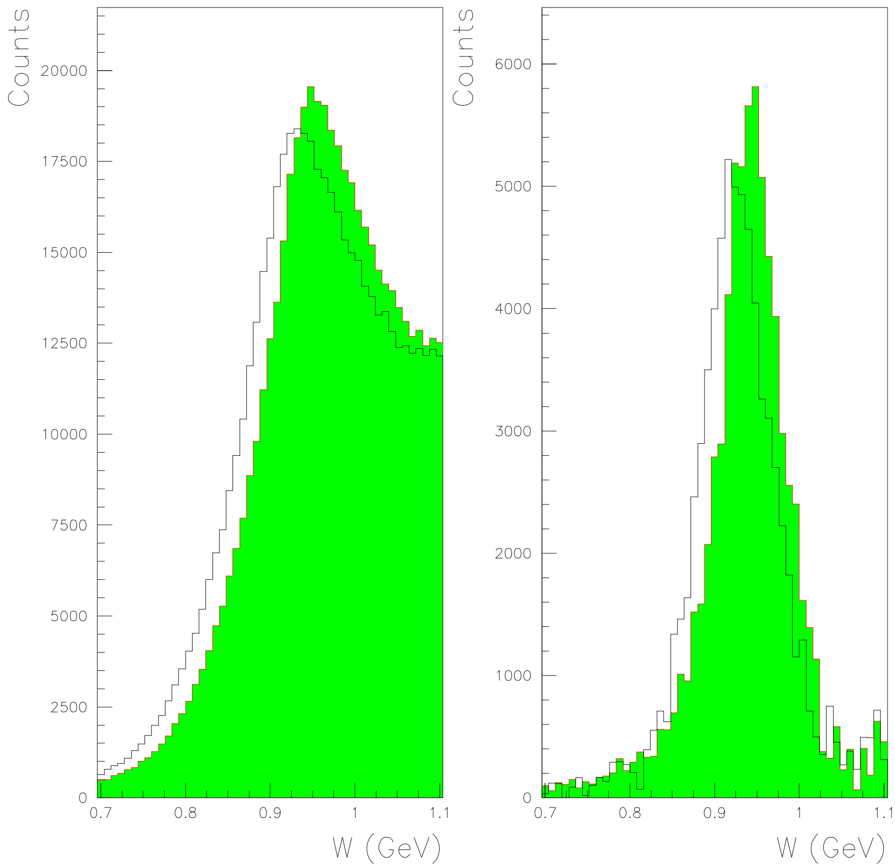

FIG. 29: W distributions before (line histogram) and after (filled histogram) the electron momentum corrections are applied. The plot on the left includes the nitrogen background contribution, which is excluded on the right–hand plot. The elastic peak becomes narrower and is positioned at its expected value ($W = 0.939$ GeV) after the momentum corrections are applied.

corrected (shaded) electron momenta. By using corrected electron momenta, the elastic peak becomes narrower and moves to its expected position. The correction decreases with increasing electron polar angle.

4.6 RUN QUALITY CHECKS

The data given in Table II are grouped into *runs*, most of which contain roughly 10 million events. Each run is broken into several files on disk. During the cooking process all the files were monitored (histograms were checked for problems) to obtain a preliminary selection of the good runs. However, some of those selected runs or files that survived the event reconstruction still contain problems caused by detector or data acquisition errors during the data taking process. The detection and elimination of these data is important especially for asymmetry measurements. The runs with low polarization, for instance, need to be eliminated because the asymmetry obtained from those runs will be consistent with zero and will not have a positive contribution to the final result.

A means of identifying these problematic runs is to monitor the number of electrons normalized to the accumulated charge (measured by the Faraday Cup) for each run in every data set. In this work, the Faraday Cup normalized number of pions and $e^-\pi^-$ coincidence events were also monitored for each run. Fig. 30 indicates such quality checks for the ND_3 data set with 2.565 GeV beam energy and 2250 A torus current. In this example, Run 15276 and 15278 are eliminated since they have a significantly different number of electrons, pions and $e^-\pi^-$ coincidences compared to the average numbers for the remaining runs in the same data set. Even though the monitored numbers for Run 15277 are quite close to the average, this run is excluded since it has a very low polarization that was not noticed during the preselection of the good runs.

4.7 EVALUATION OF THE TARGET THICKNESS

The polarized ammonia target sample is placed in the center of the magnet bore and is maintained in an approximately 1 K liquid helium bath as mentioned in section 3.7.2. The carbon target is used to estimate the nitrogen contribution by matching the carbon and ammonia missing mass squared spectra (see section 4.8.1) below 0.8 GeV. However, the carbon target is thinner than the ammonia target (see Table VI for

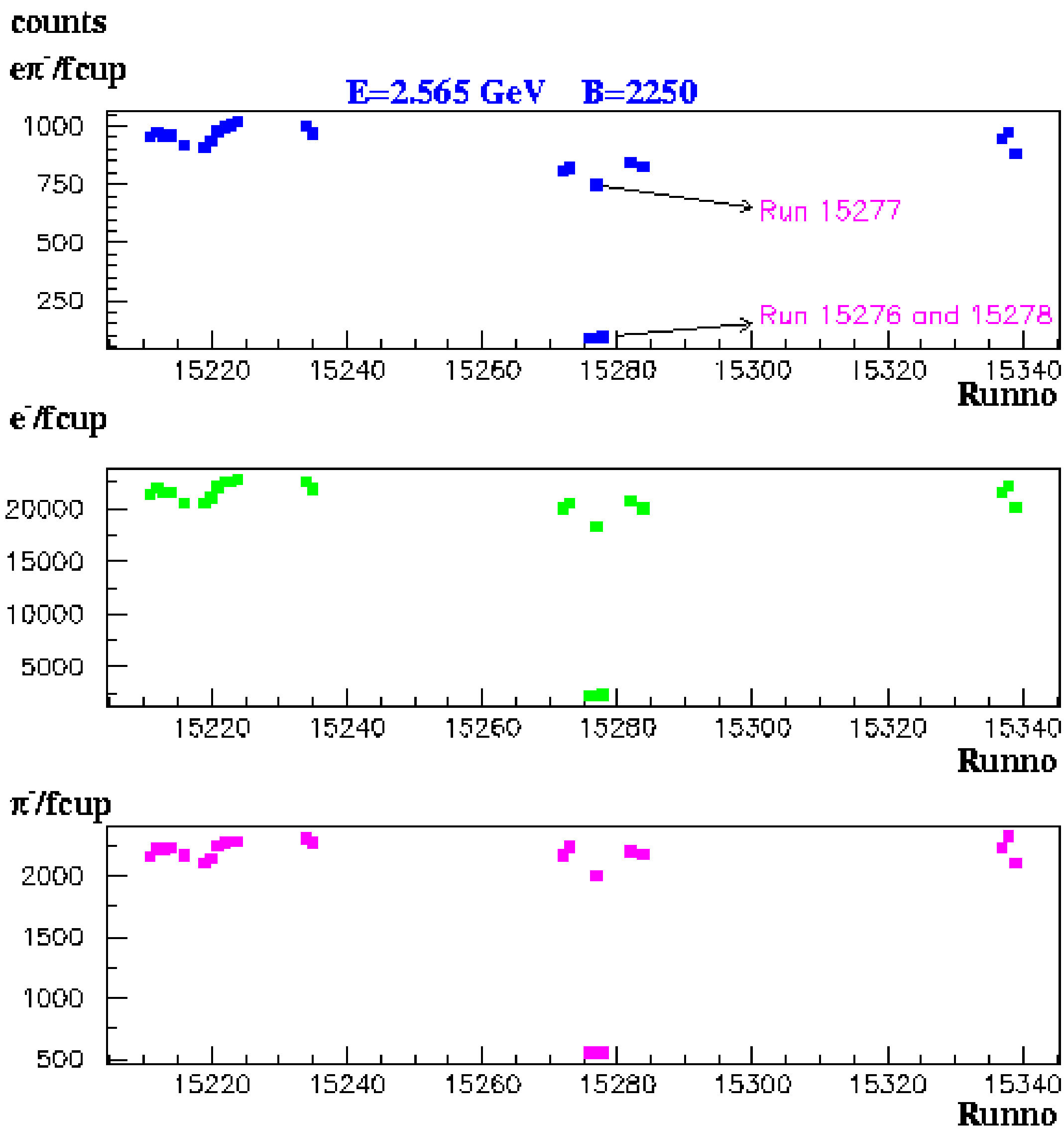

FIG. 30: Quality checks for the data set with 2.565 GeV beam energy and 2250 A torus current. Since the monitored numbers for Run 15276 and Run 15278 are clearly below the average, those two runs are excluded. Run 15277 is excluded due to very low target polarization.

some characteristics of the target and the background materials[1] used for the EG1 experiment. For this reason, there is significantly more helium in the carbon target than in the ammonia target. Therefore, an accurate background subtraction can be performed by taking the extra amount of helium into account, which is possible using the data taken on the helium (empty) target. This is possible with the knowledge of the thickness of each target component (ammonia, window foils and helium).

The thickness of the windows, the carbon, and the sum of the ND_3 and the helium are known. Even though the density of the ND_3 is known [64], the precise thickness of the ND_3 target is not known since it is in the form of frozen crystals or chunks which have an unknown packing fraction. Therefore, the separate thickness of the ND_3 and the helium need to be calculated. In the following, the thickness of the ND_3 material is evaluated from the ND_3 and carbon target runs.

The number of counts in the inclusive ND_3 spectrum can be written as

$$\begin{aligned} \mathrm{ND_3} &= \frac{N_\mathrm{A}}{e}[\frac{\rho_{\mathrm{ND_3}} X_{\mathrm{ND_3}} \sigma_{\mathrm{ND_3}}}{A_{\mathrm{ND_3}}} + \frac{\rho_{\mathrm{He}}(l - X_{\mathrm{ND_3}})\sigma_{\mathrm{He}}}{A_{\mathrm{He}}} \\ &+ \frac{\rho_{\mathrm{Al}} X_{\mathrm{Al}} \sigma_{\mathrm{Al}}}{A_{\mathrm{Al}}} + \frac{\rho_{\mathrm{K}} X_{\mathrm{K}} \sigma_{\mathrm{K}}}{A_{\mathrm{K}}}], \end{aligned} \tag{53}$$

where N_A is the Avogadro number, e is the electron charge, $l = 1.5$ cm is the distance between the entrance and the exit windows, ρ_i and X_i ($i = \mathrm{ND_3}$, He, K or Al) are the density and the thickness of the material type i, respectively, A_i is the mass number and σ_i is the inclusive cross section for the type i nucleus. The inclusive carbon (C) spectrum can similarly be written as

$$\begin{aligned} \mathrm{N_C} &= \frac{N_A}{e}[\frac{\rho_{\mathrm{C}} X_{\mathrm{C}} \sigma_{\mathrm{C}}}{A_{\mathrm{C}}} + \frac{\rho_{\mathrm{He}}(l - X_{\mathrm{C}})\sigma_{\mathrm{He}}}{A_{\mathrm{He}}} \\ &+ \frac{\rho_{\mathrm{Al}} X_{\mathrm{Al}} \sigma_{\mathrm{Al}}}{A_{\mathrm{Al}}} + \frac{\rho_{\mathrm{K}} X_{\mathrm{K}} \sigma_{\mathrm{K}}}{A_{\mathrm{K}}}]. \end{aligned} \tag{54}$$

All the cross sections can be roughly written in terms of the proton cross section σ_p as

$$\frac{\sigma_{\mathrm{He}}}{A_{\mathrm{He}}} = \frac{\sigma_{\mathrm{Al}}}{A_{\mathrm{Al}}} = \frac{\sigma_{\mathrm{K}}}{A_{\mathrm{K}}} = \frac{\sigma_{\mathrm{C}}}{A_{\mathrm{C}}} = \frac{\sigma_p(1+Z)}{2} \tag{55}$$

and

$$\frac{\sigma_{\mathrm{ND_3}}}{A_{\mathrm{ND_3}}} = \frac{10\sigma_p + 11\sigma_n}{21} = \frac{\sigma_p(10+11Z)}{21}, \tag{56}$$

[1]Also see Table XIV in Appendix B for the characteristics of the materials in the beamline.

TABLE VI: Some characteristics of the target and the background materials.

Material	Density (g/cm^3)	$\rho_i X_i$(mg/cm^2)
Al windows	2.7	56.7
Kapton foils	1.42	7.25
Carbon	2.18	495
Helium	0.145	217.5
Ammonia	1.056	

where σ_n is the neutron cross–section and Z is the σ_n/σ_p ratio above the elastic peak ($W > 1.2$ GeV). Eqs. [53] and [54] can now be combined and solved for the $\mathrm{ND_3}$ target thickness

$$\begin{aligned} X_{\mathrm{ND_3}} \quad = \quad & \frac{1}{[\frac{\rho_{\mathrm{ND_3}}(10+11Z)}{21} - \rho_{\mathrm{He}}]} \\ & \cdot\{\frac{N_{\mathrm{ND_3}}}{N_{\mathrm{C}}}[\rho_{\mathrm{C}}X_{\mathrm{C}} + \rho_{\mathrm{He}}(l - X_{\mathrm{C}}) + \rho_{\mathrm{Al}}X_{\mathrm{Al}} + \rho_{\mathrm{K}}X_{\mathrm{K}}] \\ & -[\rho_{Al}X_{Al} + \rho_K X_K + l\rho_{He}]\}. \end{aligned} \tag{57}$$

The cross–section ratio Z for various Q^2 and W^2 bins are calculated using a model [65] and given in Table XII, in Appendix B. The $\mathrm{ND_3}$ target thickness for the 2.565 GeV inbending data is then evaluated for 10 W bins above W= 1.3 GeV using eq. [57] (see Table XIII in Appendix B). A linear fit in this region gives 0.586 cm for $X_{\mathrm{ND_3}}$. This value changes every time the target material is replaced.

4.8 SPIN ASYMMETRIES AND EXTRACTION OF THE DOUBLE SPIN ASYMMETRY

The cross–section of pion electro–production using polarized beam and target can be written as

$$\sigma = \sigma_0 + P_e\sigma_e + P_t\sigma_t + P_eP_t\sigma_{et} \tag{58}$$

where σ_0, σ_e, σ_t, and σ_{et} are the cross–sections for the unpolarized measurements, electron polarization, target polarization and the double spin (both electron and target polarization) measurements, respectively. The quantities P_e and P_t represent the longitudinal beam and the longitudinal target polarization. Measurement of the last three cross–sections on the r.h.s of eq. [58] clearly requires the presence of a polarized beam and/or polarized target. They can be measured model independently by using different combination of the data sets with parallel (↑) and anti–parallel (↓) beam and target helicities:

$$A_e = \frac{\sigma_e}{\sigma_0} = \frac{1}{P_e}\frac{(N_{\uparrow\uparrow} - N_{\downarrow\uparrow}) + (N_{\uparrow\downarrow} - N_{\downarrow\downarrow})}{(N_{\uparrow\uparrow} + N_{\downarrow\uparrow}) + (N_{\uparrow\downarrow} + N_{\downarrow\downarrow})} \quad (59)$$

$$A_t = \frac{\sigma_t}{\sigma_0} = \frac{1}{(df)P_t}\frac{(N_{\uparrow\uparrow} + N_{\downarrow\uparrow}) - (N_{\uparrow\downarrow} + N_{\downarrow\downarrow})}{(N_{\uparrow\uparrow} + N_{\downarrow\uparrow}) + (N_{\uparrow\downarrow} + N_{\downarrow\downarrow})} \quad (60)$$

$$A_{et} = -\frac{\sigma_{et}}{\sigma_0} = \frac{1}{(df)P_eP_t}\frac{(N_{\downarrow\uparrow} - N_{\uparrow\uparrow}) + (N_{\uparrow\downarrow} - N_{\downarrow\downarrow})}{(N_{\uparrow\uparrow} + N_{\downarrow\uparrow}) + (N_{\uparrow\downarrow} + N_{\downarrow\downarrow})} \quad (61)$$

where $N_{\uparrow\uparrow}$, for instance, indicates the number of events when both the beam (the first arrow) and the target spin (the second arrow) are orientated in the same direction. The factor *df* represents the dilution factor, which is the percentage of the events produced by the polarized deuterons in the ND_3 target. Evaluation of the dilution factor will be discussed in section 4.8.4.

The beam polarization is flipped every second with a pseudo–random sequence such that a helicity pattern (see Fig. 31) is formed by pairs of electron bunches

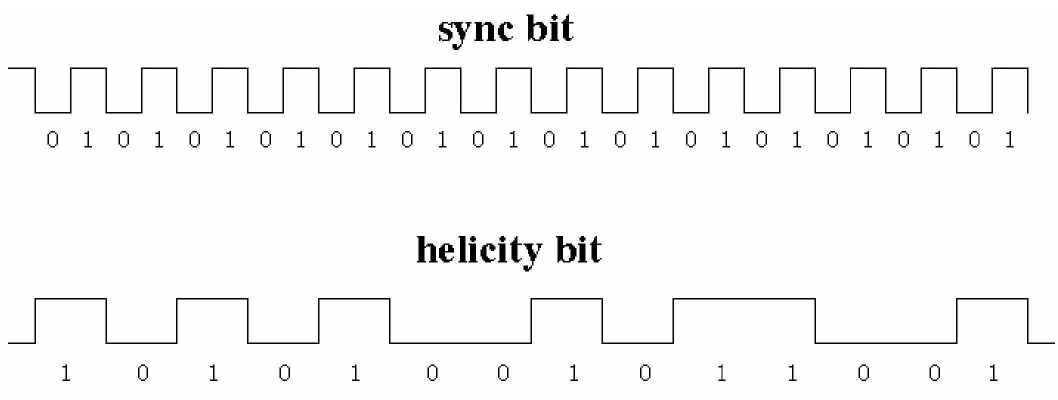

FIG. 31: Helicity structure of the beam. The helicity pattern is formed by the pairs of electron buckets with opposite helicity. Every *new word* is followed by a complementary state. The sync has a twice frequency of the helicity signal.

(*buckets*) with opposite helicity states. The *sync* pulse with a frequency of twice the helicity identifies the time of the helicity flip. The sequence can once in awhile be broken and unpaired or unknown helicity states can be produced. These states are rejected using a program, HelP [66]. Rejection of problematic helicity states is always done in pairs. After the elimination of these states, there still exists a charge asymmetry that causes a false asymmetry, because the electron current is actually slightly different for different helicity states. One way of observing this charge asymmetry is by studying the inclusive carbon data. Since the carbon target is unpolarized, any asymmetry in the inclusive carbon spectra for opposite electron helicities is due to the false asymmetry. This method is discussed in Ref. [68] and an asymmetry of the order of $\sim 0.3\%$ for inbending data is observed. Another way of investigating the beam charge asymmetry is by comparing the accumulated charge in the Faraday Cup for the positive (FC^+) and negative helicity states (FC^-). The result is consistent with the result of the method mentioned in Ref. [68]. This false asymmetry is then corrected by a proper normalization of the number of counts in each helicity state to the corresponding FC counts (FC^+ or FC^-).

Although the beam polarization is changed every second during the EG1 experiment, the ND_3 target polarization was reversed only once with the 2.494 GeV beam energy, but since a very small amount of data were collected at this configuration, these data were not analyzed for this work. Therefore, with the available data one can only measure the asymmetry

$$\frac{1}{(df)P_eP_t}\frac{N_{\downarrow\uparrow}-N_{\uparrow\uparrow}}{N_{\downarrow\uparrow}+N_{\uparrow\uparrow}}, \tag{62}$$

which can be written in terms of the cross–sections in eq. [58] as

$$-\frac{\sigma_e+\sigma_{et}}{\sigma_0+\sigma_t}. \tag{63}$$

If one integrates over all ϕ^*, the σ_e and σ_t terms average to zero. However, we do not have a full ϕ^* acceptance. A calculation using AO in which the cross–sections were integrated over our experimental acceptance has shown that σ_e and σ_t are negligibly small (since the ϕ^* distribution is approximately symmetric around 180°). For this reason, it is possible to make the following approximation:

$$A_{et} = -\frac{\sigma_{et}}{\sigma_0} \sim \frac{1}{(df)P_eP_t}\frac{N_{\downarrow\uparrow}-N_{\uparrow\uparrow}}{N_{\downarrow\uparrow}+N_{\uparrow\uparrow}}. \tag{64}$$

In order to measure this quantity, $e\pi^-$ events in which the beam helicity and target polarization are parallel ($N_{\uparrow\uparrow}$), or anti–parallel ($N_{\downarrow\uparrow}$) were integrated (for each Q^2 and W bin) over our ϕ^* acceptance, and their difference was divided by their sum. The regions with zero acceptance were not included in the integration since we have no data there. The result, corrected for the dilution factor (df) and the product of the beam and target polarization (P_eP_t), yields A_{et} (approximately), which can also be expressed in terms of the asymmetries A_1 and A_2 (see section 2.2.4):

$$A_{et} = \sqrt{1-\epsilon^2}\cos\theta_\gamma \frac{A_1 + \eta A_2}{1+\epsilon R}(\theta^*). \tag{65}$$

In the remaining sections of this chapter the intermediate steps to obtain the double spin asymmetry A_{et} will be discussed. The results are given in terms of the asymmetry

$$\frac{A_1 + \eta A_2}{1+\epsilon R}, \tag{66}$$

which is extracted by dividing the expression given in eq. [64] by a factor $\sqrt{1-\epsilon^2}\cos\theta_\gamma$.

4.8.1 Missing Mass Technique

The CLAS detector (see section 3.2) in Hall B is capable of measuring multi–particle final states. We can therefore use the missing mass (MM) technique to identify the reaction $ed \to e'p\pi^- p$.

We first attempted to study π^- production from the deuteron by looking for the events in which the final state π^- and p were identified in coincidence with the scattered electron. An example of such a reconstructed event in CLAS is shown in Fig. 32. Even though the calculated missing mass distribution peaks at the proton mass (0.938 GeV), this channel has very few events since some protons hit the polarized target magnet coils and cannot be detected. Therefore, we used events in which the scattered electron is identified in coincidence with a π^- emitted from the target. We calculated the MM based on the assumption that the proton in the deuteron is a *spectator* and the electron interacts only with the neutron. Applying energy and momentum conservation and using the notation in Fig. 4, the squared mass of the missing particle (MM_X^2) is calculated for the reaction $en \to e'\pi^- X$ as

$$MM_X^2 = (p_i + k_i - k_f - p_\pi)^2 \tag{67}$$

where k_i and k_f are the four–momenta of the incident and scattered electron, p_i and p_π are the four–momenta of the target neutron and the emitted π^-, respectively.

The MM^2 distribution obtained from the ND_3 data is indicated in Fig. 33. The proton peak at $MM^2 = 0.88$ GeV^2 is observed on top of a large background. The background is due to the contribution from the nitrogen and helium events. A separation of the proton peak from the multi–pion contribution at higher missing mass,

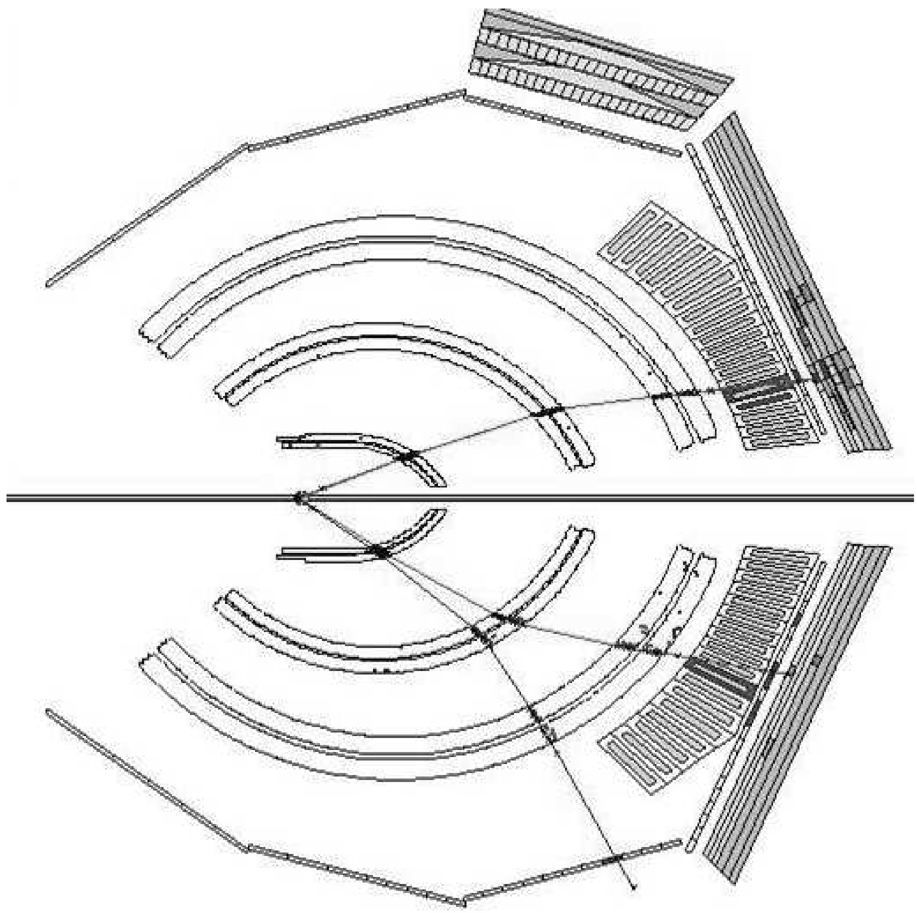

FIG. 32: A reconstructed event in CLAS with an electron (the track above the central line, beamline), π^- (the track below the beamline, bent upwards) and proton candidate (bent away from the beamline).

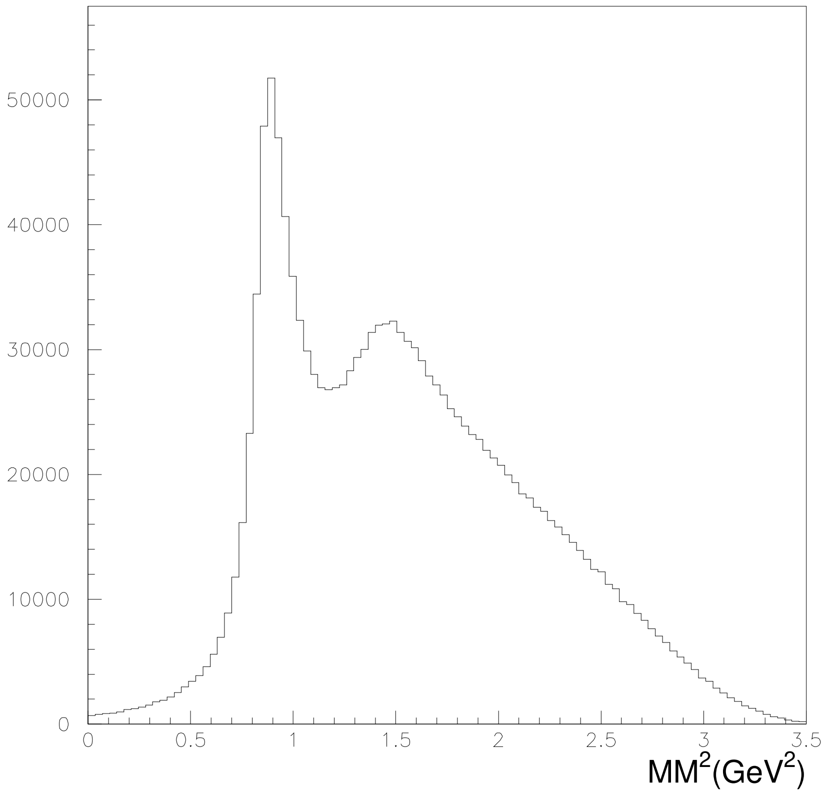

FIG. 33: Missing mass distribution of the $e\pi^-$ channel obtained from the ND_3 target. The proton peak is observed on a large background due to the nitrogen and helium in the target.

beyond the proton peak, is possible by the subtraction of this background, which will be discussed in the next section.

4.8.2 Nitrogen Background Subtraction

The missing mass distribution in Fig. 33 for the ND_3 target includes a large background, which must be removed from the deuteron events for a proper selection of the $e\pi^-$ channel. The majority of the background events originate from the nitrogen[2], which has a very small polarization caused entirely by the unpaired proton. For this reason, data on the carbon (^{12}C) target were collected to estimate the nitrogen (^{15}N) contribution. ^{12}C, with its six protons and six neutrons, was chosen to simulate ^{15}N since it is a neighbor in the periodic table of the elements and it is not polarizable.

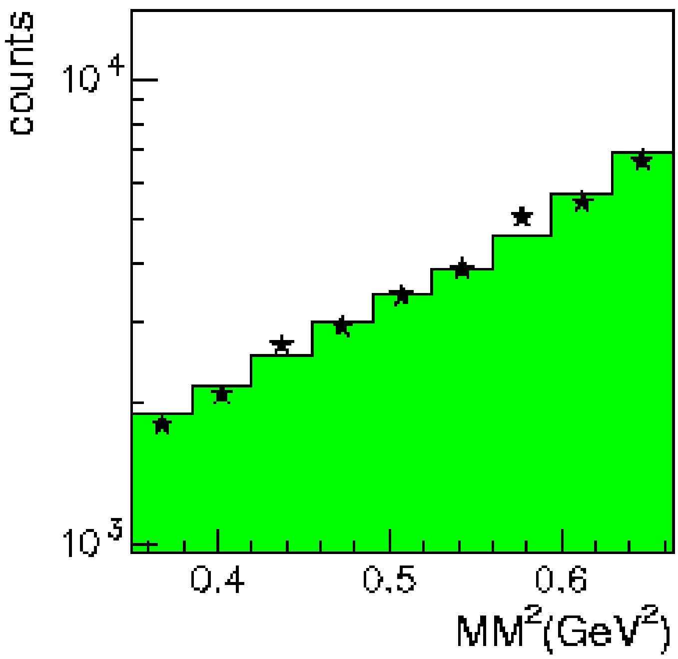

FIG. 34: MM^2 distribution of the ND_3 (shaded histogram) and the normalized ^{12}C distribution (stars) in the region below the proton peak and above 0.6 GeV.

The subtraction is performed with the assumption that the tail of the missing mass spectrum below 0.8 GeV contains only the ^{15}N contribution, not the polarized deuterons. Therefore, the MM^2 spectrum from the ^{12}C target is normalized to that of the ND_3 in the region 0.36 GeV^2 $< MM^2 <$ 0.64 GeV^2 (see Fig. 34), corresponding

[2]Discussion of the helium contribution is left for section 4.8.3

to 0.6 GeV $< MM <$ 0.8 GeV. The lower limit of 0.6 GeV is set by the fact that below this point the two spectra do not match. The left plot in Fig. 35 indicates the

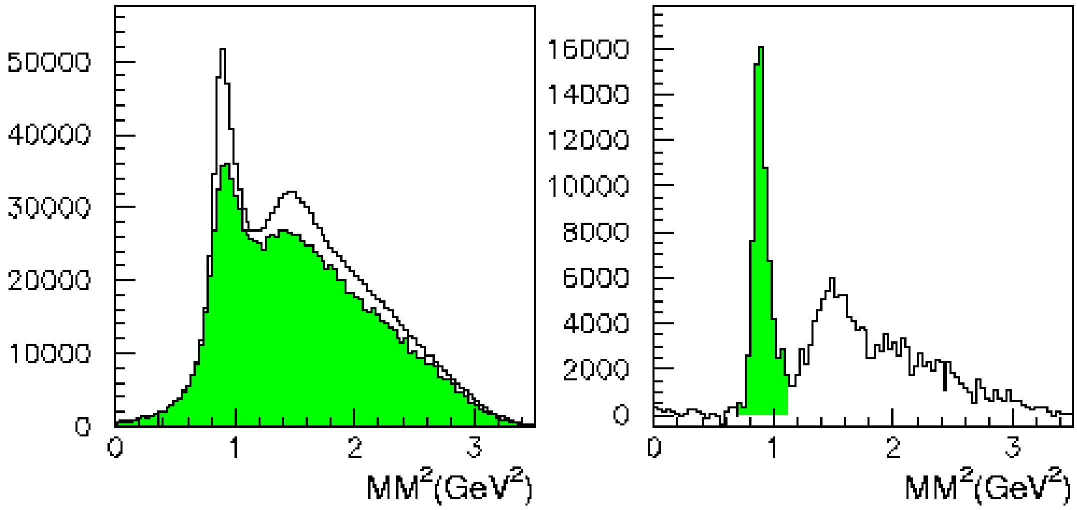

FIG. 35: Missing mass distribution of the ^{12}C data (shaded) superimposed on that of the ND_3 (left plot). A peak is observed at the proton mass after the ^{12}C subtraction (right plot). Multi–pion contribution is also clearly seen above the proton peak.

whole MM^2 distribution for all the Q^2 bins for the normalized ^{12}C (shaded) and ND_3 targets.

Two different methods are used to find the normalization constant f. In the first method, simply the ratio of the number of events in the ND_3 and ^{12}C MM distributions is taken in the region from 0.6 GeV up to 0.8 GeV as explained above. The second method uses the inclusive W spectra for the ND_3 and ^{12}C. In this method the ratio of the number of events in the ND_3 and ^{12}C inclusive spectra is evaluated in the W tail from 0.6 to 0.8 GeV. This ratio then needs to be corrected by a factor

$$\frac{8}{6}\frac{(6+6R_{np})}{(7+8R_{np})} \tag{68}$$

where 8/6 is the ratio of the number of neutrons in ^{15}N and ^{12}C, and R_{np} is the elastic cross–section ratio of neutron to proton. Even though the statistics in the former method (normalization in the MM tail) are worse than in the latter, within error the normalization constants obtained from both methods are consistent with each other especially in the lower Q^2 bins (see Table VII). Because there are no model dependent assumptions involved in the MM subtraction, the normalization constants as determined by the missing mass method are used in this analysis.

TABLE VII: Normalization constants obtained from 2.494 GeV inbending data set using two different methods. The two methods give consistent results within error, especially in the two lower Q^2 bins.

Method	Q^2 (GeV^2)	Normalization constants (f)
MM Tail	$0.3 < Q^2 < 0.5$	16.44±0.48
	$0.5 < Q^2 < 0.9$	16.27±0.45
	$0.9 < Q^2 < 1.5$	13.73±0.57
W Tail + Corrections	$0.3 < Q^2 < 0.5$	16.84±0.11
	$0.5 < Q^2 < 0.9$	16.32±0.11
	$0.9 < Q^2 < 1.5$	17.22±0.19

4.8.3 Helium Contribution to the Background and $\vec{e}\vec{n} \to e'\pi^- p$ Channel Selection

The carbon target used to estimate the nitrogen background contribution has a thickness of 0.227 cm, while the ammonia target is 0.586 cm thick as evaluated in section 4.7. Therefore, the ^{12}C contains more helium than the ND_3. Furthermore, as indicated in Fig. 36, the carbon and helium do not yield the same invariant mass distribution. For these reasons, helium must be accounted for separately as a background component.

A more accurate background spectrum consisting of the correct amount of nitrogen in the ammonia target can be constructed as

$$\text{Background} = \text{carbon} + a\frac{\text{FC}^{carbon}}{\text{FC}^{helium}}\text{helium} \tag{69}$$

where $\text{FC}^{carbon}/\text{FC}^{helium}$ is the correction for the integrated current for carbon and helium, and $a = -0.23$ is evaluated by taking into account the thickness of the various components (foils, helium, etc.,) in each target (ammonia, carbon and helium) [67]. The background subtraction is performed as mentioned in the previous section.

After the background subtraction, a clear peak at the proton mass is observed and the $e\pi^-$ channel is selected by a cut 0.78 GeV^2 $< MM^2 <$ 0.95 GeV^2 around the proton peak (shaded region in Fig. 37). This missing mass cut separates the proton peak from the multi–pion events with only a small contamination. The systematic error associated with the background subtraction, as well as the MM cut, will be discussed in section 5.3.

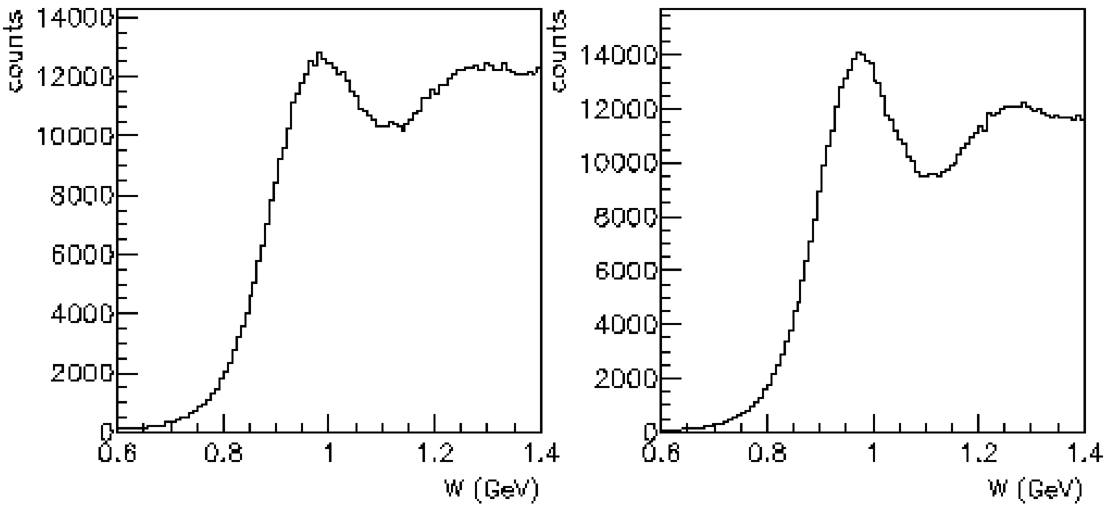

FIG. 36: Invariant mass distribution for the carbon (left plot) and helium target (right plot). Since the shapes of those two spectra are not the same, helium contribution should also be taken into account for the background subtraction.

4.8.4 Dilution Factor

The fraction of events from the polarized deuterons in the ammonia (ND_3) target

$$df = \frac{\mathrm{D}_3}{\mathrm{ND}_3} \tag{70}$$

is defined as the dilution factor, whose evaluation is important for evaluating the double spin asymmetry.

Nitrogen does not have a polarized neutron, so it only affects the denominator of A_{et}. The dilution factor, as a function of W, is evaluated as

$$\frac{\mathrm{ND}_3 - f[^{12}\mathrm{C} + a\frac{\mathrm{FC}^{carbon}}{\mathrm{FC}^{helium}}(^4\mathrm{He})]}{\mathrm{ND}_3} \tag{71}$$

for the $e\pi^-$ channel selected as indicated by the shaded region in Fig. 37. The normalization constant f, and thus the dilution factor, differs depending on whether or not the helium contribution is taken into account for the background subtraction. The effect of this difference on the double spin asymmetry is studied in section 5.3.

Only four sets of data at different energies or/and torus currents are being analyzed for this work. A proper evaluation of the dilution factor for each data set requires the presence of carbon and helium data, in addition to the ND_3, at each setting.

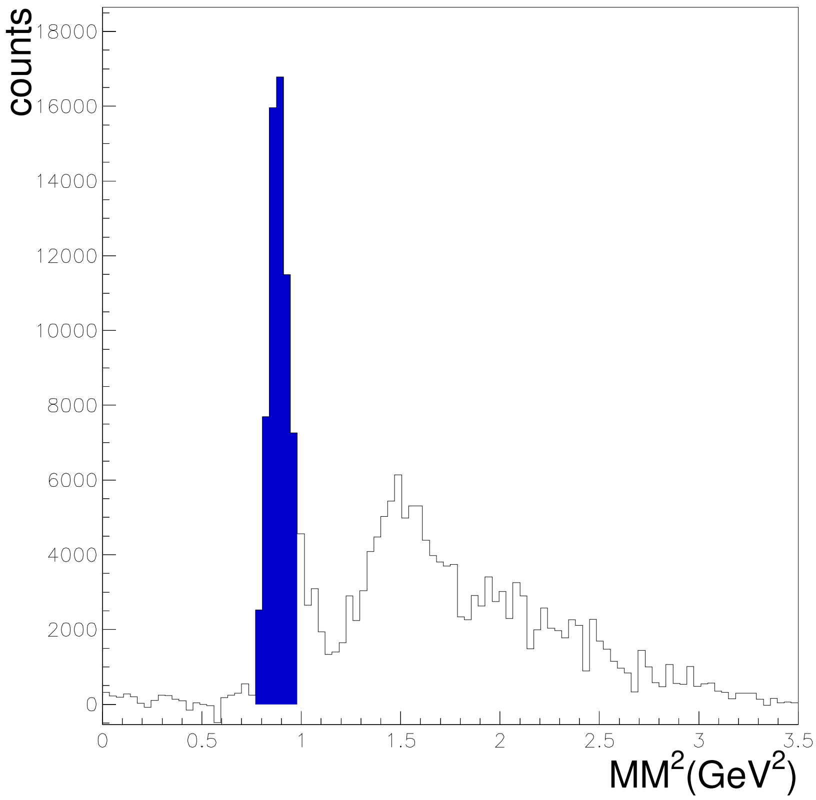

FIG. 37: MM^2 distribution after the background subtraction. A peak at the proton mass is observed and the $e\pi^-$ channel is selected by applying a cut around the proton peak (shaded area).

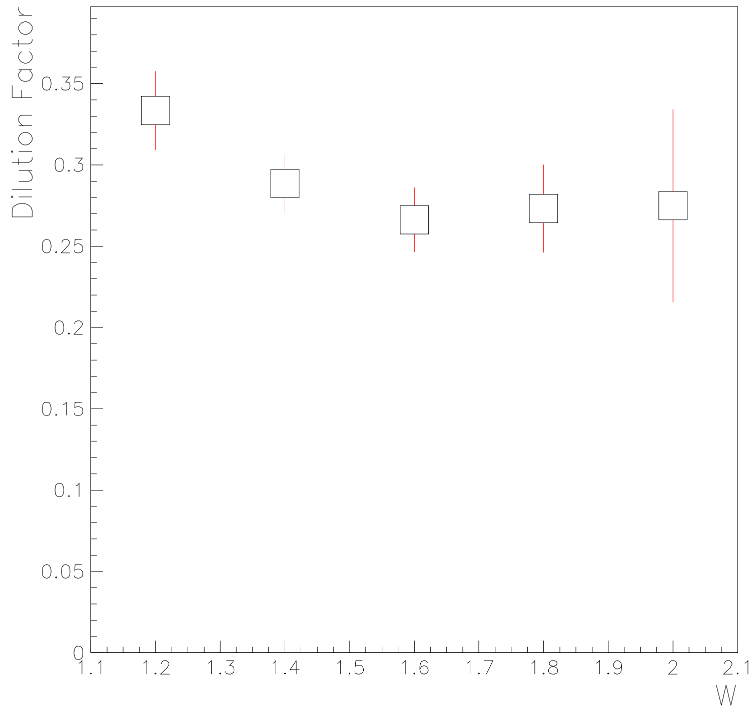

FIG. 38: Dilution factor as a function of W obtained from the data set with 2.565 GeV energy and 2250 A torus current. The same values are used for the other three data sets since no helium data are available for those data.

Nevertheless, data are available both for carbon and helium only at the 2.565 GeV energy and 2250 A torus current. Therefore, a reliable dilution factor can only be obtained for this data set. Fig. 38 indicates the results of such evaluation for five W bins. These values are used for the other three data sets.

4.8.5 Extraction of the Beam and Target Polarization (P_eP_t) from Elastic Scattering

The product of beam and target polarization P_eP_t appears in the denominator of the expression for the double spin asymmetry as indicated in eq. [61], and it is one of the main sources of systematic errors. Therefore, a precise determination of P_eP_t is required for an accurate measurement of the double spin asymmetry.

The beam polarization P_e was measured using a Møller polarimeter as mentioned in section 3.1. The typical beam polarization was $\sim 70\%$ with a few percent accuracy. The target polarization P_t, on the other hand, is measured using the NMR technique (see section 3.7.2). The nominal accuracy of that technique is $\sim 2\%$. However, for our experiment the NMR coils were placed outside the target walls. Therefore, those coils were mainly sensitive to the polarization close to the edge of the target cell. It was also observed that the beam on the target was mostly rastered in a small region around the target center. The interaction between the beam and the target material produces a local depolarization that cannot be detected by the NMR. Because the accuracy of the NMR technique is affected by these problems, an independent and more accurate method based on extracting the product P_eP_t from the known elastic asymmetry (A_{el}) was used.

In order to use this method, the dilution factor must be known since the measured asymmetry (A_{meas}) is related to the elastic asymmetry (A_{el}) by the equation

$$A_{meas} = (df) \cdot (P_eP_t) \cdot A_{el}. \tag{72}$$

The elastic asymmetry is defined as [19]

$$A_{el} = \sqrt{1-\epsilon^2}\cos\theta^*_\gamma \frac{A_1(\gamma^*)}{1+\epsilon R} + \sqrt{2\epsilon(1-\epsilon)}\sin\theta^*_\gamma \frac{A_2(\gamma^*)}{1+\epsilon R} \tag{73}$$

where

$$\epsilon = [1 + 2(1 + \frac{(E-E')^2}{Q^2})\tan^2(\frac{\theta}{2})]^{-1}, \tag{74}$$

θ^*_γ is the angle between the virtual photon direction and the target spin, $A_1(\gamma^*)$ and $A_2(\gamma^*)$ are the virtual photon asymmetries, and R is the ratio of longitudinal to transverse photoabsorption cross–section. In elastic scattering $A_1 = 1$ and R is defined as

$$R = (A_2)^2 = \frac{G_E^2}{\frac{(E-E')^2}{Q^2}G_M^2}, \tag{75}$$

where G_E and G_M are the electric and magnetic form factors. These factors are calculated for proton (G_E^p, and G_M^p) and neutron (G_E^n, and G_M^n) separately, using the following expressions[3]:

$$G_E^p = G^{dipole} \tag{76}$$

[3]A fit of the G_E^n world data was used (Ref. [70]).

TABLE VIII: Theoretical A_{el} values for elastic scattering off of the deuteron for various Q^2 bins.

Data	$< Q^2 >$ (GeV^2)	A_{el}
Outbending	0.15	0.071
	0.24	0.103
	0.34	0.138
Inbending	0.4	0.155
	0.64	0.229
	1.1	0.367

$$G_M^p = 2.79 G^{dipole} \tag{77}$$

$$G_E^n = 1.913 \frac{(E-E')^2}{Q^2} \frac{G^{dipole}}{1 + 5.6 \frac{(E-E')^2}{Q^2}} \tag{78}$$

$$G_M^n = -1.91 G^{dipole} \tag{79}$$

where

$$G^{dipole} = (1 + \frac{Q^2}{0.71 \text{ GeV}^2})^{-2}. \tag{80}$$

Finally, the elastic asymmetry is calculated for the deuteron by taking the cross–section weighted average of the elastic asymmetries for the proton and neutron. The results for various Q^2 bins are given in Table VIII.

The procedure for extracting this product is given here for one of the ND_3 data sets with 2.565 GeV energy and 2250 A torus current. The data are divided into three Q^2 bins: $0.3 < Q^2 < 0.5$, $0.5 < Q^2 < 0.9$ and $0.9 < Q^2 < 1.5$. The nitrogen background is subtracted by normalizing the carbon to the ND_3 for invariant mass $W = 0.6 - 0.8$ GeV (see Fig. 39). The elastic events are selected by applying a cut around the elastic peak ($0.86 < W < 1.02$) and the elastic asymmetry

$$A_{meas} = \frac{\frac{\text{FC}^-}{\text{FC}^+} N_{\downarrow\uparrow} - N_{\uparrow\uparrow}}{\frac{\text{FC}^-}{\text{FC}^+} N_{\downarrow\uparrow} + N_{\uparrow\uparrow}}. \tag{81}$$

is measured as a function of W for each Q^2 bin. FC^+ and FC^- in eq. [81] are the integrated beam charge for positive and negative helicity states, respectively. Table XV in Appendix B reports A_{meas} and the dilution factors for eight W and three Q^2 bins.

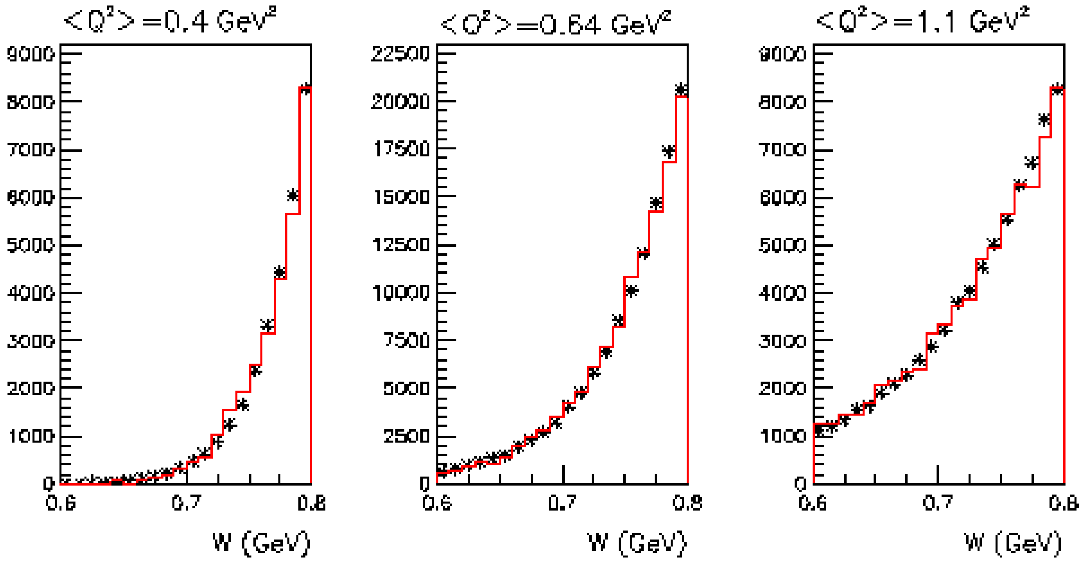

FIG. 39: W distribution for carbon (solid) normalized to the W spectrum for ND_3 (stars) in the W region $0.6-0.8$ GeV for three Q^2 bins.

By using eq. [72], A_{el} values from Table VIII, and A_{meas} and the dilution factors from Table XV (see also Table XVI for the 2.494 GeV inbending, Table XVII for the 2.562 GeV outbending, and Table XVIII for the 2.494 GeV outbending data sets) in Appendix B, the P_eP_t can be determined for eight W bins in each Q^2 region (Fig. 40). Finally, the product of the beam and target polarization for this data set can be evaluated by taking the average of the P_eP_t values at each Q^2.

This method is applied to each data set[4] and the results are reported in Table IX.

4.9 RADIATIVE CORRECTIONS

Electrons can radiate a real photon before or after they exchange a virtual photon with the nucleon. In these cases, the kinematical variables $(Q^2, W, \theta^*, \phi^*)$ describing the process can change. Therefore, corrections due to these radiative effects need to be estimated. A calculation using the MAID prediction with and without radiative effects shows negligible changes in A_{et} for π^- electro–production. Therefore, we did not correct our data for radiative effects.

[4] P_eP_t for the 2.494 GeV outbending data set could be evaluated only for $< Q^2 >= 0.3442$ since there is no data in the $W < 0.8$ GeV for smaller Q^2 bins.

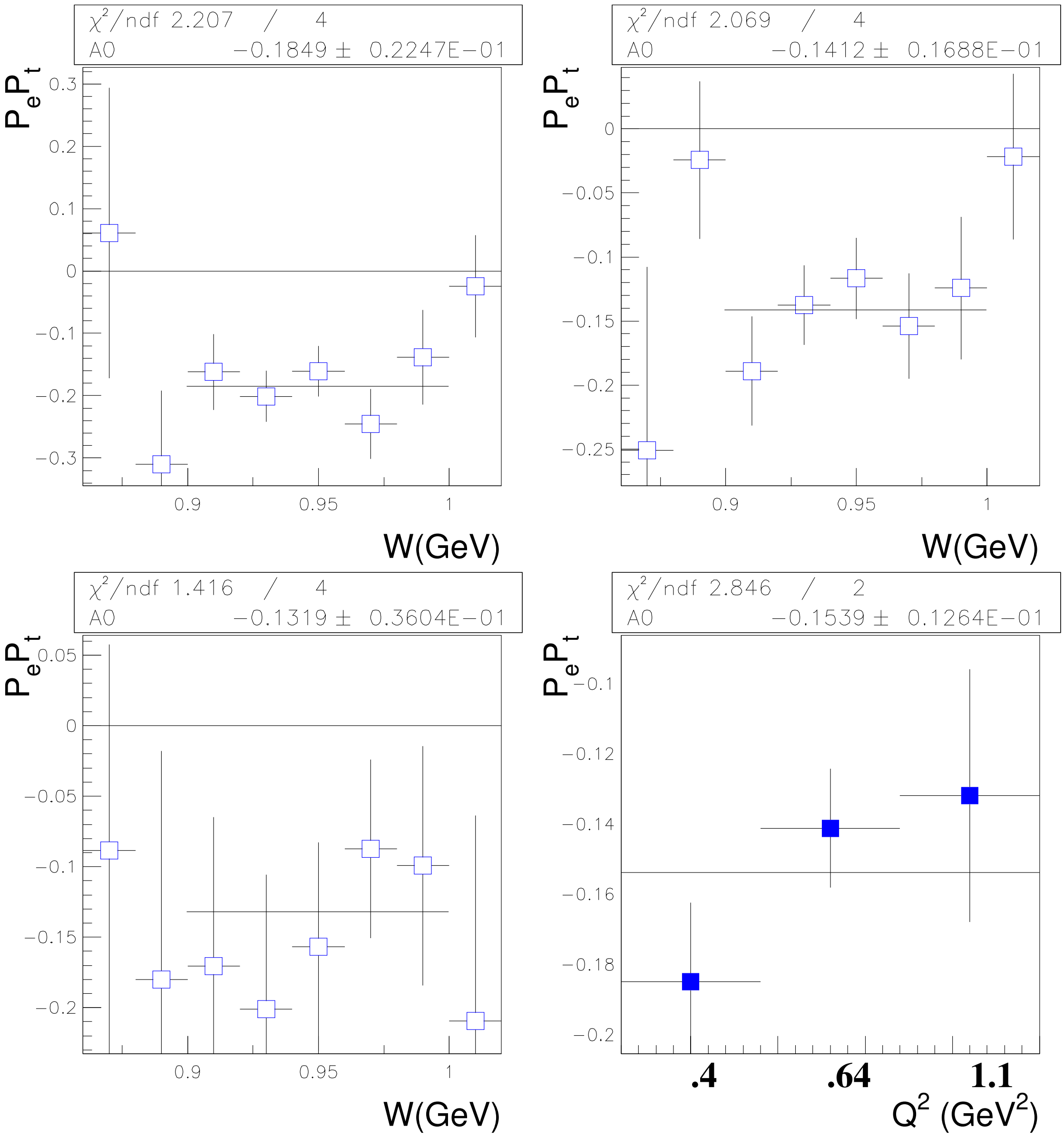

FIG. 40: Product of the beam and target polarization for eight W and three Q^2 bins (two upper plots and bottom–left plot) extracted from the data set with 2.565 GeV energy and 2250 A torus current. A linear fit is applied in the region $0.9 < W < 1$ to find the average P_eP_t values for each Q^2 bin. The bottom–right plot indicates the average P_eP_t value for that data set.

TABLE IX: Product of the beam and target polarization for each data.

Beam Energy	Torus Current	$< Q^2 >$	$P_e P_t$	$< P_e P_t >$
2.565	2250	0.40	-0.185 ± 0.022	-0.154 ± 0.013
		0.64	-0.141 ± 0.017	
		1.10	-0.132 ± 0.036	
2.494	2250	0.40	$+0.123 \pm 0.020$	$+0.1074 \pm 0.011$
		0.64	$+0.105 \pm 0.013$	
		1.10	$+0.085 \pm 0.029$	
2.562	-1500	0.1545	-0.238 ± 0.143	-0.18 ± 0.048
		0.2423	-0.197 ± 0.067	
		0.3442	-0.138 ± 0.08	
2.494	-1500	0.3442	$+0.088 \pm 0.042$	$+0.088 \pm 0.042$

The results of this analysis, extraction of A_{et} in π^- electro–production, as well as an evaluation of the systematic errors, are discussed in the next chapter.

CHAPTER 5

RESULTS

The main focus of this analysis, the details of which have been discussed previously, is extraction of the double spin asymmetry, as well as $(A_1 + \eta A_2)/(1 + \epsilon R)$, for the π^- channel in the resonance region. Four sets of data on the ND_3 target, of which two are outbending and two are inbending, have been analyzed. The $\pi^- p$ events have been accumulated in Q^2 and W bins. Due to the limited statistics, the data are integrated over the center–of–mass azimuthal angle ϕ^*. Results will be presented both integrated over all θ^* and for a range in cosθ^* from 1 to 0.17.

In the following sections, the angular distribution and the extracted asymmetries will be discussed. Evaluation of the systematic errors is described in the last section.

5.1 ANGULAR DISTRIBUTIONS

Fig. 41 indicates the ϕ^* (left) and θ^* (right) angular distributions for outbending (top) and inbending (bottom) runs. The scatter plots in Fig. 42 illustrate the θ^* versus ϕ^* coverage of the single π^- electro–production events for the outbending (top) and inbending (bottom) runs. In the following subsections, $\sigma_e + \sigma_{et}$ as a function of ϕ^*, and the double spin asymmetry as a function of θ^* are discussed.

5.1.1 $\sigma_e + \sigma_{et}$

Before extracting the double spin asymmetries, we have extracted the electron spin asymmetry A_e as a check on the data. This asymmetry is given by σ_e/σ_0, where σ_e has a simple sinusoidal sinϕ^* dependence (see eq. [25]). As indicated in eq. [59], A_e can be acquired by collecting data with different orientations of the beam and target spins. Since the deuteron data analyzed for this work have only one target spin orientation, it is not possible to extract A_e precisely. However, the available data allow one to obtain $\sigma_e + \sigma_{et}$, which is simply the difference between the number of counts for the anti–parallel and parallel beam and target spins. The double polarization cross–section σ_{et}, is a more complicated function of ϕ^* and can be written as

$$a + b\cos\phi^* + c\cos^2\phi^* + d\sin^2\phi^*, \tag{82}$$

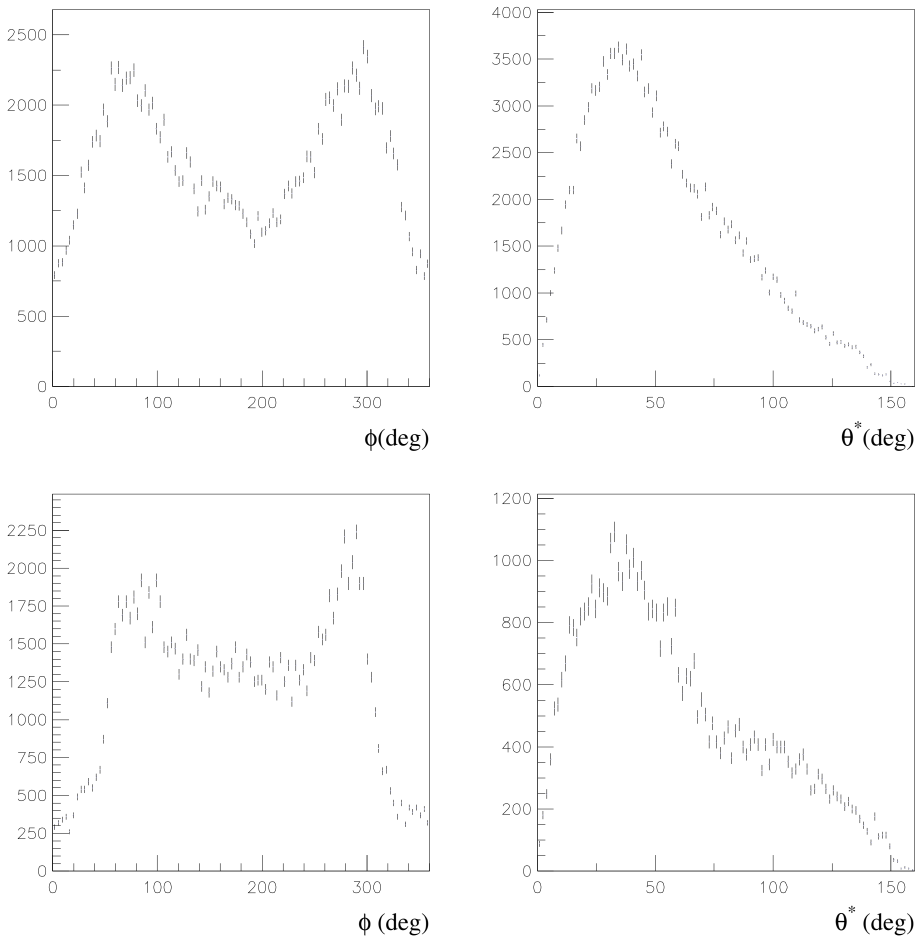

FIG. 41: ϕ^* (left) and θ^* (right) angular distributions of the pion in the center–of–mass system averaged over all W. The upper plots are obtained from the outbending runs with relatively low Q^2, while the bottom plots are from the inbending runs with a higher Q^2 range. The ϕ^* distribution is almost symmetric around 180 degrees.

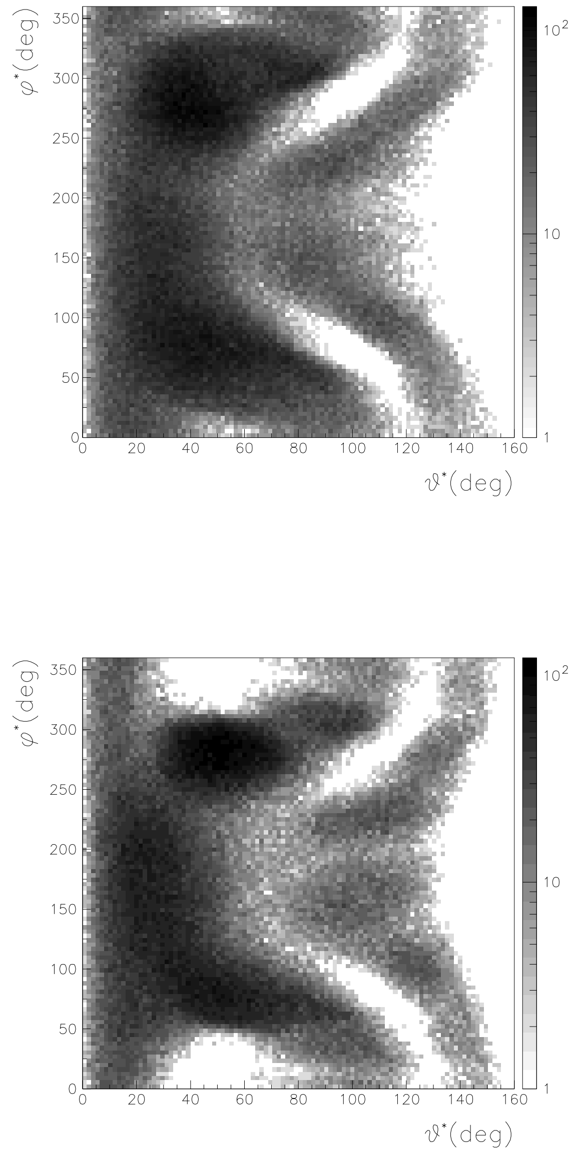

FIG. 42: ϕ^* versus θ^* angular distributions at the center–of–mass system obtained from the outbending (top) and the inbending (bottom) runs.

where a, b, c, and d include kinematic factors and response functions (see eq. [27]). The upper plot in Fig. 43 shows $\sigma_e + \sigma_{et}$ as a function of the azimuthal angle ϕ^* in arbitrary units. The data are fitted with the function $\sin\phi^*$ (solid line) and $a + b\cos\phi^* + c\cos^2\phi^* + d\sin^2\phi^* + e\sin\phi^*$ (dashed line). The data indicate a clear sinusoidal behaviour with only a small contribution from A_{et}. To measure A_{et} we integrate over ϕ^* (for non–zero acceptance regions) and the σ_e term averages to zero.

5.1.2 $A_{et}(\theta^*)$

The double spin asymmetry as a function of θ^* is shown for one set of data (bottom plot in Fig. 43). The response functions depend on θ^* and the detailed behaviour must be explained by models. However, it is clear that $A_{1/2}$ is dominant at forward angles. This can be understood by noting that the $\gamma_v N$ system is decaying into a spin–0 pion and a spin–1/2 nucleon. If the total angular momentum is 3/2 then the final state has non–zero orbital angular momentum and the angular distribution is suppressed at forward angles.

5.2 DOUBLE SPIN ASYMMETRY AND $(A_1 + \eta A_2)/(1 + \epsilon R)$

The first measurement of the double spin asymmetry A_{et} for the $\vec{e}\vec{n} \rightarrow e\pi^- p$ channel has been performed as the primary purpose of this work. The double spin asymmetry on the proton for the $\vec{e}\vec{p} \rightarrow e\pi^+ n$ channel has also been previously studied [68, 69].

A lower Q^2 region (0.05 GeV^2 $< Q^2 <$ 1.0 GeV^2) can be accessed by the outbending runs, whereas the inbending runs cover a higher Q^2 range (0.25 GeV^2 $< Q^2 <$ 1.5 GeV^2). Despite the fact that both data groups provide results in the region 0.3 GeV^2 $< Q^2 <$ 0.4 GeV^2, they cannot be combined due to the difference in the acceptance for each data group. Therefore, the data are divided into two Q^2 bins and a Q^2 cut of 0.08 GeV^2 $< Q^2 <$ 0.4 GeV^2 is applied to the outbending data, while a cut of 0.4 GeV^2 $< Q^2 <$ 1.2 GeV^2 is applied to the inbending data group as indicated with the shaded region on the upper plots in Fig. 44. The double spin asymmetry A_{et} as a function of W and integrated over θ^* and ϕ^* is then plotted for the two Q^2 regions mentioned above (bottom plots in Fig. 44).

Because these are the first measurement of the double spin asymmetry for the π^- channel, the results can only be compared with phenomenological and theoretical models. The lines on the bottom plots in Fig. 44 represent the predictions made by

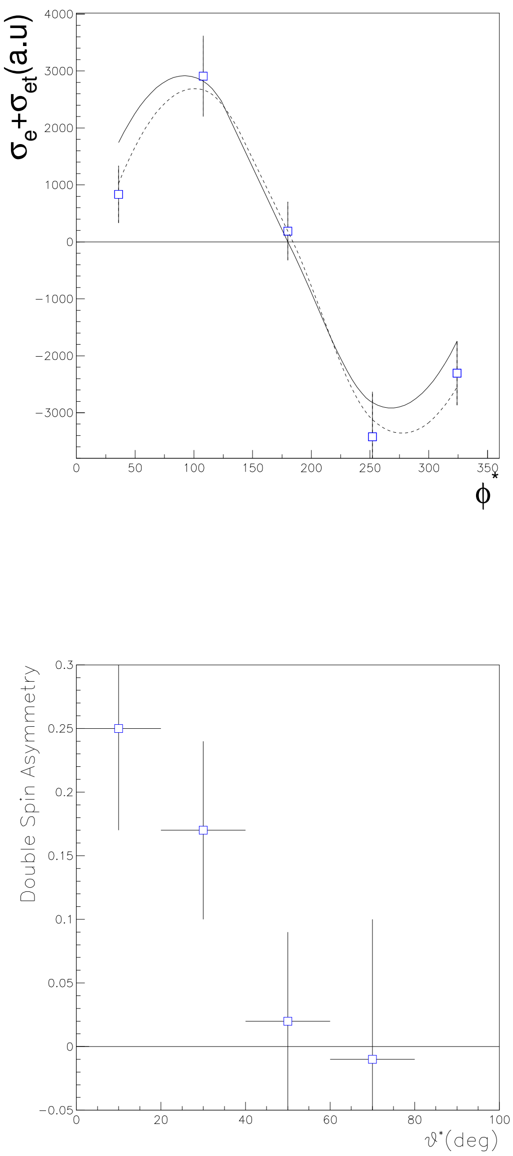

FIG. 43: $\sigma_e + \sigma_{et}$ as a function of ϕ^* in arbitrary units (top) and the double spin asymmetry as a function θ^* (bottom). The solid and dashed lines represent the functions $\sin\phi^*$ and $a + b\cos\phi^* + c\cos^2\phi^* + d\sin^2\phi^* + e\sin\phi^*$, respectively, fitted to the data. The data are averaged over all W and $0.4\ \mathrm{GeV}^2 < Q^2 < 1.2\ \mathrm{GeV}^2$.

MAID [11], which is a Unitary Isobar Model for pion photo- and electro–production on the nucleon covering a W range from the pion threshold up to 2 GeV (see section 2.1).

The data in the lower Q^2 region (bottom left plot in Fig. 44) show a trend towards zero asymmetry with increasing W. In contrast with the double spin asymmetry on the proton [68], the neutron data indicate a more negative behaviour in the $P_{33}(1232)$ and in the third resonance region at higher Q^2 (bottom right plot in Fig. 44). A reasonable agreement with the MAID prediction is observed except for the $P_{33}(1232)$ at low Q^2.

The asymmetry $(A_1 + \eta A_2)/(1 + \epsilon R)$ is extracted by dividing the double spin asymmetry by the kinematic factor $\sqrt{1-\epsilon^2}\ \cos\theta_\gamma$, where θ_γ is the angle between the virtual photon and the direction of the incoming electron, and ϵ is the virtual photon polarization defined as (see eq. [74]). The results, integrated over ϕ^*, are shown in Fig. 45 for the same two Q^2 bins. In the upper plots, the data have been integrated over all θ^* where acceptance is greater than zero and in the lower plots a narrower range in theta, $0.17 < \cos\theta^* < 1$, has been selected since there is a good kinematic coverage in that region as seen in Fig. 42. The solid and dashed lines represent the MAID prediction with and without the acceptance taken into account, respectively. In other words, in the solid line the calculation is integrated over the regions where the experiment has acceptance and in the dashed line the MAID prediction assumes a full acceptance. The small difference between these curves indicates the fact that a good kinematic coverage is provided by the CLAS for the π^- channel and the acceptance correction is small. The observed results have in general a good agreement with the MAID prediction, except in the delta region at low Q^2 where we have poor statistics.

The results have also been compared with the output of the *Amplitudes and Observables* program, AO [12], which was developed at JLab (Fig. 46). The solid and dashed lines respectively represent the AO predictions with and without the acceptance corrections while the data points are represented by the squares. AO also shows a good agreement with the data except for high W when the results are integrated over all θ^* for the higher Q^2 region (upper right plot in Fig. 46). Fig. 47 shows the observed asymmetries compared with the models MAID (solid line) and AO (dashed line).

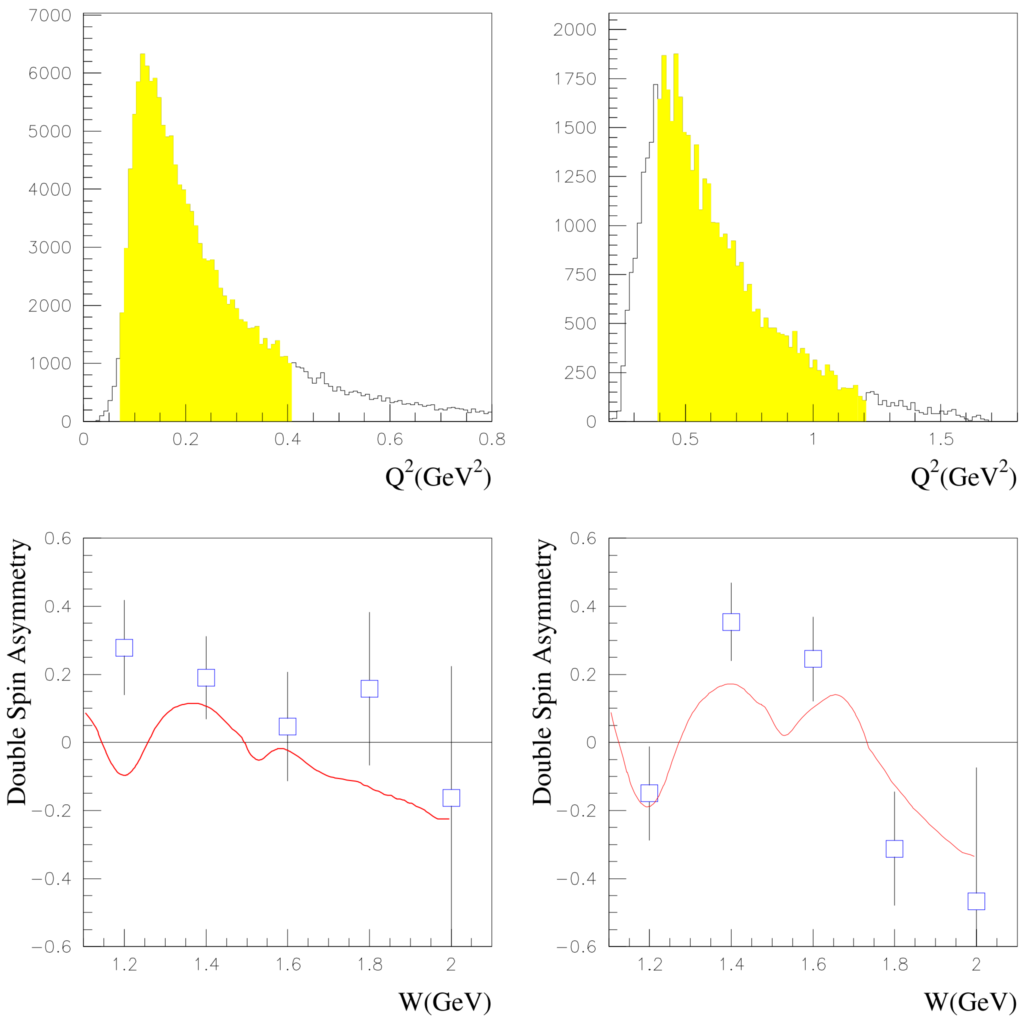

FIG. 44: Q^2 (top) and double spin asymmetry (bottom) for the outbending (left) and the inbending runs (right). The shaded region in the upper plots indicate the Q^2 range used to extract the double spin asymmetries in the bottom plots. The curves on the bottom plots represent the MAID prediction.

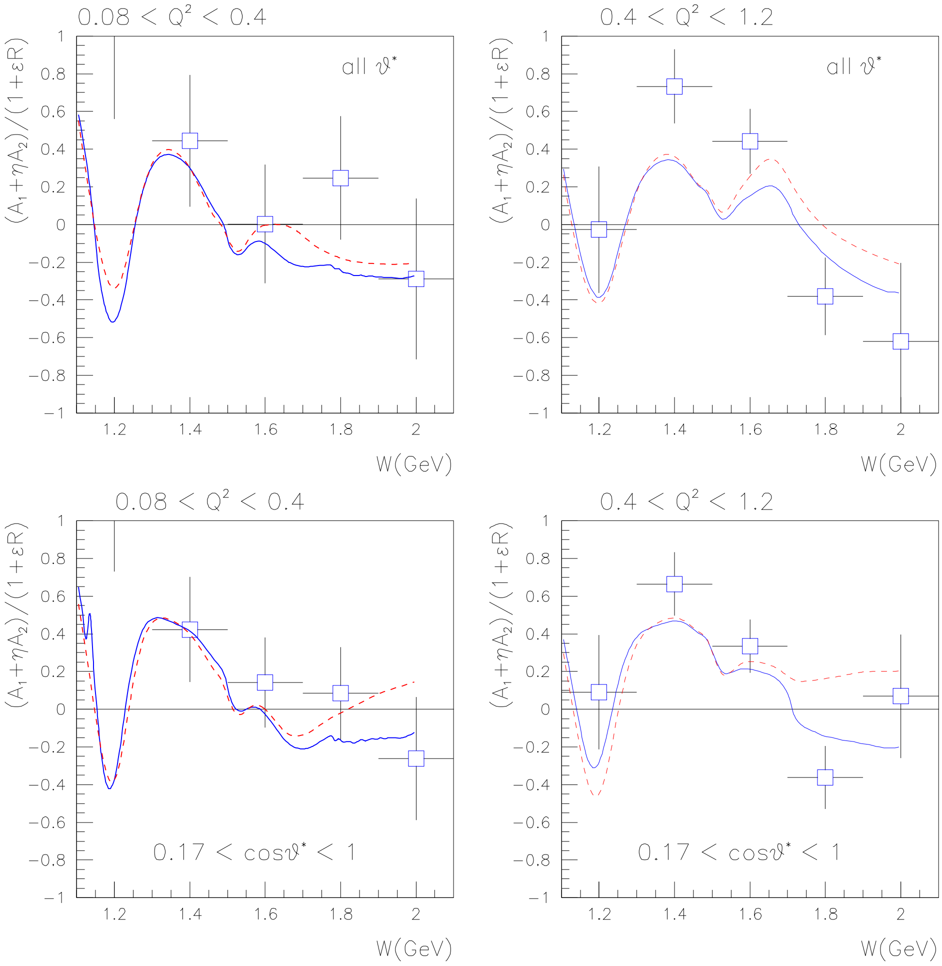

FIG. 45: The asymmetry $(A_1 + \eta A_2)/(1 + \epsilon R)$ as a function of the invariant mass W. The left and right plots at the top represent the asymmetry integrated over θ^* for 0.08 GeV$^2 < Q^2 < 0.4$ GeV^2 and 0.4 GeV$^2 < Q^2 < 1.2$ GeV^2, respectively. The plots at the bottom indicate the asymmetry with the additional cut $0.17 < \cos\theta^* < 1$. The MAID prediction with and without acceptance (see the text) is given by the solid and the dashed line, respectively.

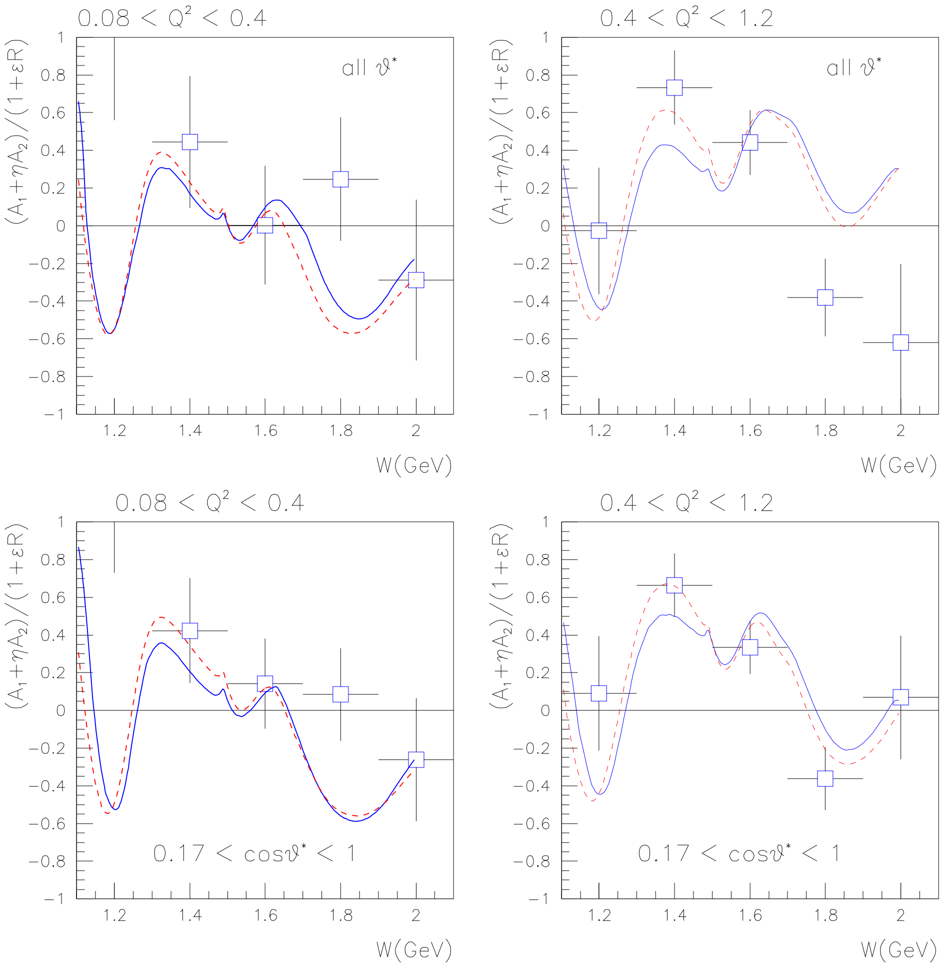

FIG. 46: Data are the same as Fig. 45. The AO prediction with and without acceptance (see the text) is given by the solid and the dashed line, respectively.

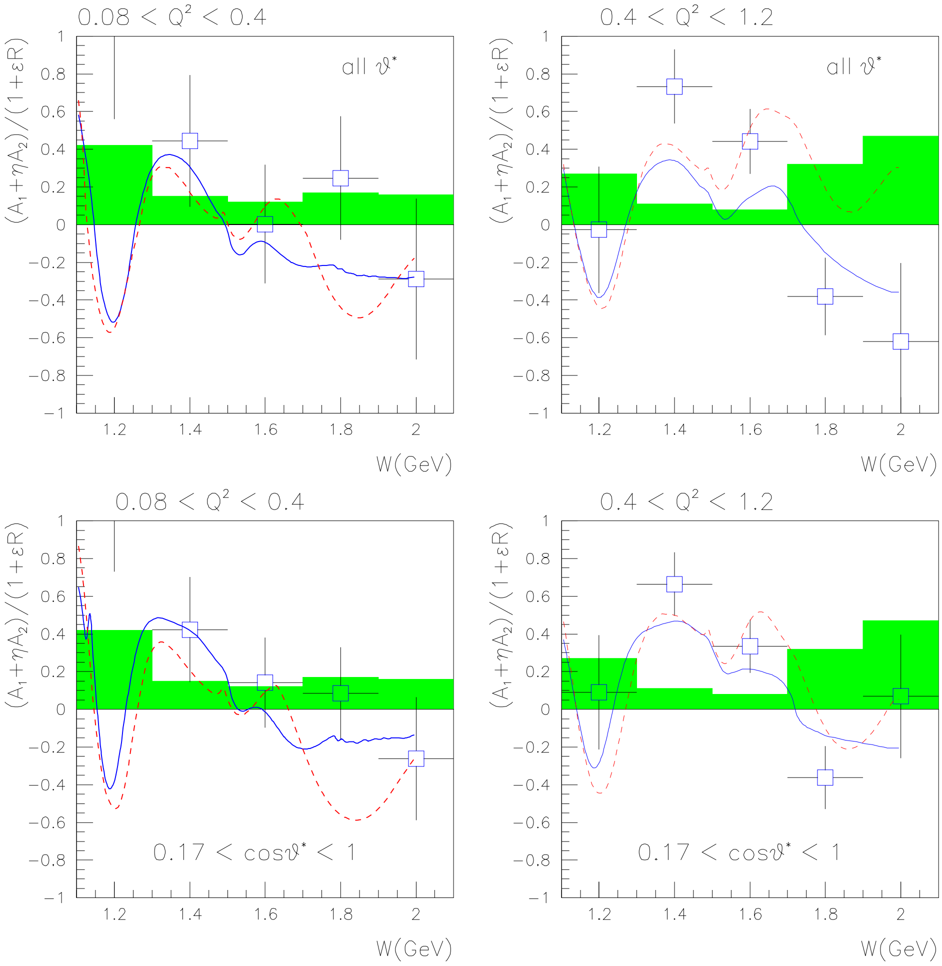

FIG. 47: Data are the same as Fig. 45 and Fig. 46 The MAID and AO predictions are given by the solid and the dashed line, respectively. The systematic errors are indicated with the shaded region.

5.3 SYSTEMATIC ERRORS

During the process of data taking and data analysis, various uncertainties that systematically shift the measured asymmetries from their true values can be introduced. Therefore, the investigation of those errors and the knowledge of their effects on the final asymmetries are important.

The primary systematic errors for this analysis, including the method for obtaining the dilution factor, the MM cut for channel selection, the effect of the fiducial cuts, and the evaluation of the product of the beam and target polarization are discussed in the remaining sections of this chapter. Other sources of systematic errors are estimated to be negligibly small in comparison with the statistical errors.

5.3.1 Channel Selection

The final asymmetries have been obtained using a cut 0.78 GeV^2 $< MM^2 <$ 0.95 GeV^2 to select the $e\pi^-$ channel as described in section 4.8.3. Because the tail of the multi–pion peak can contaminate the proton peak (see Fig. 37) and affect the final asymmetries, the channel selection is one of the main sources of systematic error for this analysis. The MM spectrum for the inbending data is shown for each W bin in Fig. 48, suggesting some contamination in the second, third and the fourth W bins.

In order to estimate the systematic error on the final asymmetry due to the selection of this channel, the asymmetry $(A_1 + \eta A_2)/(1 + \epsilon R)$ with the full MM^2 cut (0.78 GeV^2 $< MM^2 <$ 0.95 GeV^2) has been compared with the asymmetry obtained using the right half of the MM^2 cut (0.85 GeV^2 $< MM^2 <$ 0.95 GeV^2) mentioned above. The comparison yields negligible systematic uncertainty for the second and the third W bins, while the uncertainties are significant for the remaining bins (Fig. 49). The systematic error for each bin was estimated as the difference between the data points in Fig. 49. For the outbending data, the missing mass cut produces a less systematic shift in the asymmetry and so the systematic error was estimated as half of the difference between the final asymmetry and that produced by the right–hand side of the missing mass peak. Systematic errors are listed in Table X and Table XI.

5.3.2 Background Subtraction

As mentioned in section 4.8.2, data on the ^{12}C and empty (helium) targets were collected to estimate the background contribution to the ND_3 spectra. The helium

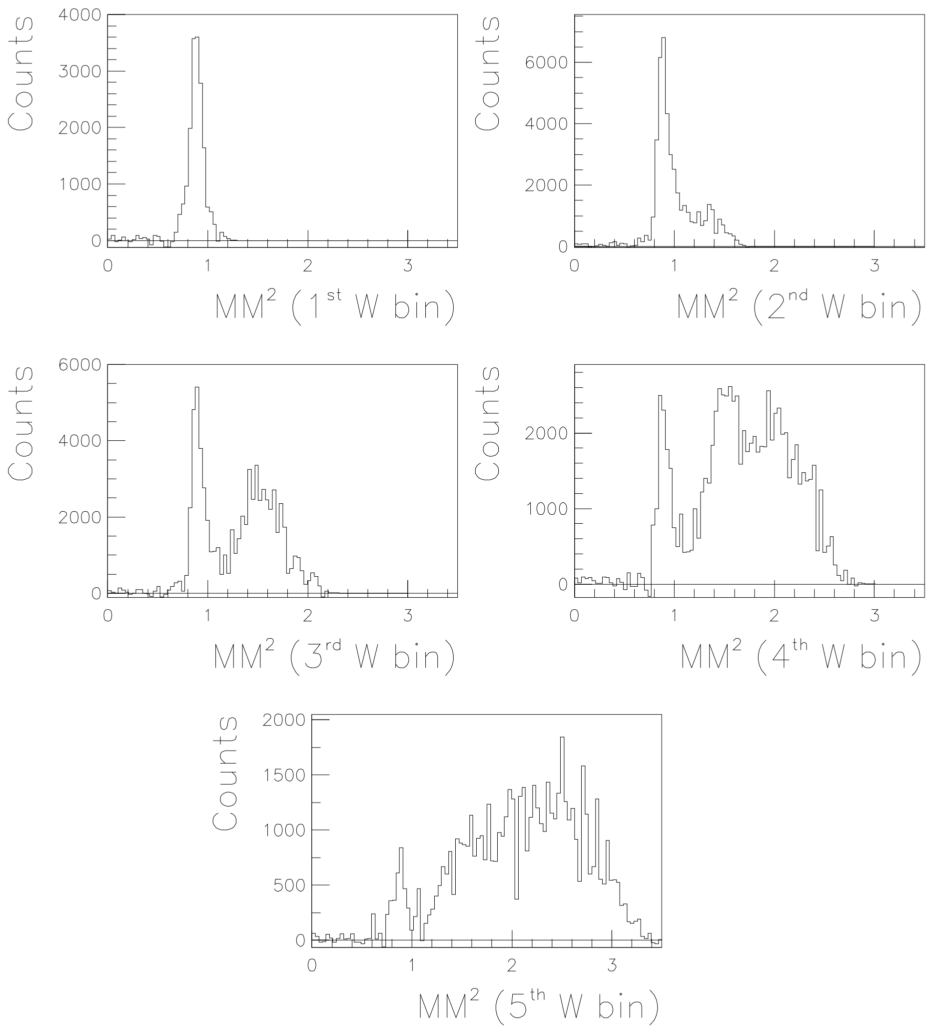

FIG. 48: Background subtracted MM^2 distribution for each W bin. An evidence of contamination is observed for the second, third and fourth W bins.

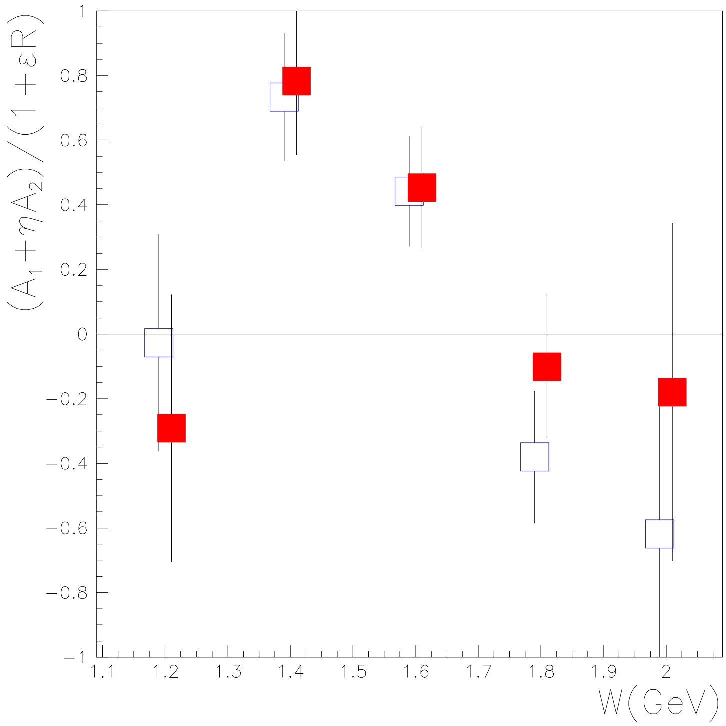

FIG. 49: Comparison of the $(A_1 + \eta A_2)/(1 + \epsilon R)$ as a function of W using the full MM^2 cut (empty squares) and the 0.85 GeV^2 $< MM^2 <$ 0.95 GeV^2 cut (filled squares) for the inbending data.

contribution has to be taken into account in order to have a proper background subtraction due to the different amount of helium in carbon and ND_3 along with the difference in the shape of the invariant mass distribution of both targets (see section 4.8.3).

Many systematic problems, such as the uncertainty in the ND_3 target thickness, and differences between the nitrogen and the carbon, can change the final asymmetry during the process of background subtraction. A way to estimate the systematic error originating from these problems is to extract the dilution factor without using the empty target data to account for the extra helium in the carbon target. The analysis has illustrated that the dilution factor increases when the extra helium contribution is ignored. The systematic uncertainty for each W bin was estimated by taking the percentage difference in these two dilution factors (an average of 6%). This analysis was only possible for the 2.565 GeV inbending data because the other data sets do not have empty target runs (see section 4.8.4). Therefore, a separate systematic error for the 2.494 GeV inbending data was not extracted and the systematic error derived above was used for the final inbending result.

As noted in section 4.8.4, the dilution factor determined for the 2.565 GeV inbending data was also used for the outbending runs. The systematic error for the outbending runs was estimated by adding an extra 3% to the errors determined for the inbending runs.

5.3.3 Fiducial Cuts

The electron and pion fiducial cuts are discussed in section 4.2. Two fiducial cuts, loose and tight, are available for the electrons. The loose version of those cuts is less strict than the tight one and throws away less electrons ($\sim 30\%$) than the tight version ($\sim 50\%$). Therefore, final asymmetries are obtained using the loose electron fiducial cuts to have better statistics.

In order to estimate the systematic uncertainty due to the application of the fiducial cuts, both loose and tight electron fiducial cuts were applied to the 2.565 GeV inbending data and the asymmetries $(A_1 + \eta A_2)/(1 + \epsilon R)$ are compared for both sets of cuts (Fig. 50). The observed change in the asymmetry is small compared to the large statistical errors, but the systematic error was estimated as 1/2 the difference in the asymmetry with loose and tight cuts. For the outbending data, the systematic error could not be studied since only loose electron fiducial cuts were developed for

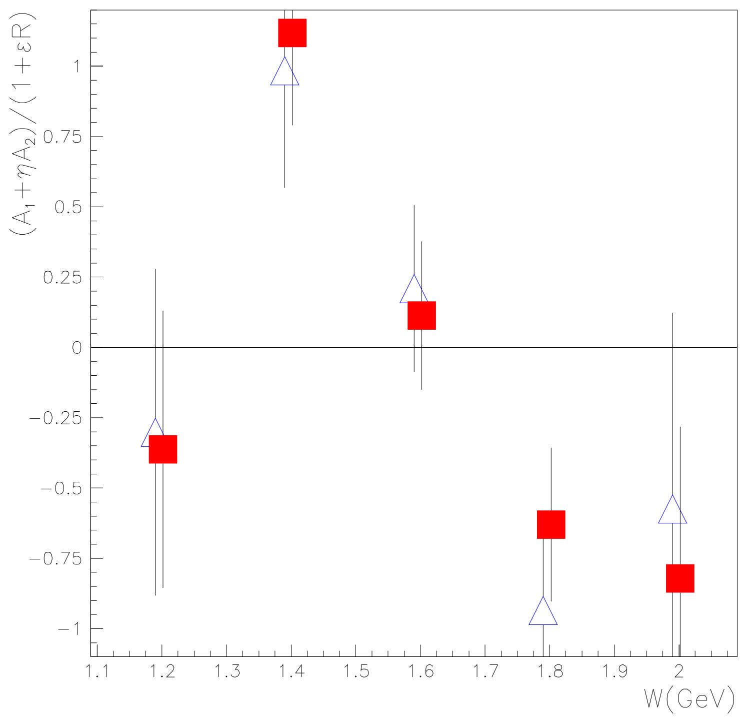

FIG. 50: Comparison of the $(A_1 + \eta A_2)/(1 + \epsilon R)$ as a function of W using the loose (filled squares) and tight fiducial cuts (triangles) for the 2.565 GeV inbending data set.

these data. The systematic errors due to the fiducial cuts for the outbending runs were estimated at 20% for all but the 1.6 GeV data point, which is close to zero, and was therefore assigned an error of 0.08 (the average of the inbending values).

5.3.4 Beam and Target Polarization

Asymmetry measurements are directly affected by the product of the beam and target polarization. Therefore, the uncertainty on this polarization product is directly transferred to the final asymmetry as a systematic error. As mentioned in the previous sections, the beam and target polarization are measured using a Møller polarimeter and the NMR technique, respectively. However, because of the reasons explained in section 4.8.5, an additional technique described in the same section is used to evaluate the product of the beam and target polarization. Results of this study for each data set are given in Table IX[1]. The systematic uncertainty due to P_eP_t was estimated by taking the percentage statistical error on this quantity and it was multiplied by the asymmetries in order to estimate the systematic uncertainty on the final asymmetry due to P_eP_t. The average systematic error is 0.03 for the inbending and 0.1 for the outbending runs.

5.3.5 Beam Charge Asymmetry

A careful measurement of asymmetries requires avoidance of any effect which can cause a false asymmetry in the final results. In the EG1 data, a false asymmetry can originate from the difference in the electron rates for the two electron helicity states of the beam. This false asymmetry of $\sim 0.3\%$ for the inbending runs can be seen for example in the inclusive asymmetry on the carbon data (see Ref. [68]). The reason for using the carbon data in order to observe any false asymmetry is because carbon is not polarizable and consequently the asymmetry should yield zero. In this work, the Faraday Cup readings have been used to identify any false asymmetry and this method yields a consistent result with the method mentioned in Ref. [68]. This false asymmetry is corrected by simply using the Faraday Cup counts in each helicity state to normalized the data (see eq. [81]).

For the inbending data, the Faraday Cup counts in each helicity state are high (around 25 in each bucket). Therefore, the statistical error on the correction factor

[1]Statistical error weighted average of P_eP_t is 0.127 ± 0.008 for the inbending and 0.127 ± 0.03 for the outbending runs.

TABLE X: $(A_1+\eta A_2)/(1+\epsilon R)$ and systematic errors for 5 W bins (inbending data).

$<W>$ (GeV)	$(A_1+\eta A_2)/$ $(1+\epsilon R)$	MM cut	P_eP_t	fid. cuts	backgr. sub.	total
1.2	-0.027 ± 0.336	0.27	0.002	0.03	0.002	0.27
1.4	$+0.733 \pm 0.197$	0.05	0.044	0.07	0.051	0.11
1.6	$+0.442 \pm 0.171$	0.01	0.027	0.05	0.022	0.08
1.8	-0.380 ± 0.205	0.28	0.028	0.15	0.023	0.32
2.0	-0.619 ± 0.416	0.44	0.037	0.13	0.080	0.47

$\frac{\mathrm{FC}^-}{\mathrm{FC}^+}$ is small and the systematic error on these data due to the beam charge asymmetry is estimated to be also very small. For the outbending runs, on the other hand, the Faraday Cup counts for each helicity state are quite low (around 5) and the statistical error on the correction factor is large. The beam charge asymmetry for the outbending ND_3 runs have been investigated and found to be (0.24±0.1)% for the earlier runs and (0.38±0.05)% for the later ones [71]. In order to evaluate the systematic error due to the beam charge asymmetry, the Faraday Cup correction factor has been recalculated using the beam charge asymmetries given above taking into account the statistical error (for instance, $(0.24-0.1)\% = 0.14\%$ and $(0.24+0.1)\% = 0.34\%$), yielding 1.0068 and 1.0028 for $\frac{\mathrm{FC}^-}{\mathrm{FC}^+}$. The asymmetry $(A_1+\eta A_2)/(1+\epsilon R)$ is obtained using both of these correction constants and the results are compared in Fig. 51. The systematic error for each W bin was estimated as 1/2 of the difference in the asymmetries given by the empty and the filled squares. It can be concluded that the systematic shift is small compared to the statistical errors.

A summary of the systematic errors discussed above are given in Table X and Table XI for the inbending and outbending data, respectively. It is clearly seen from Table X that the major systematic uncertainty comes from the MM cut especially for the first, fourth and the fifth W bin.

In the following chapter, a brief summary of the data analyzed for this work will be given and the results will be discussed.

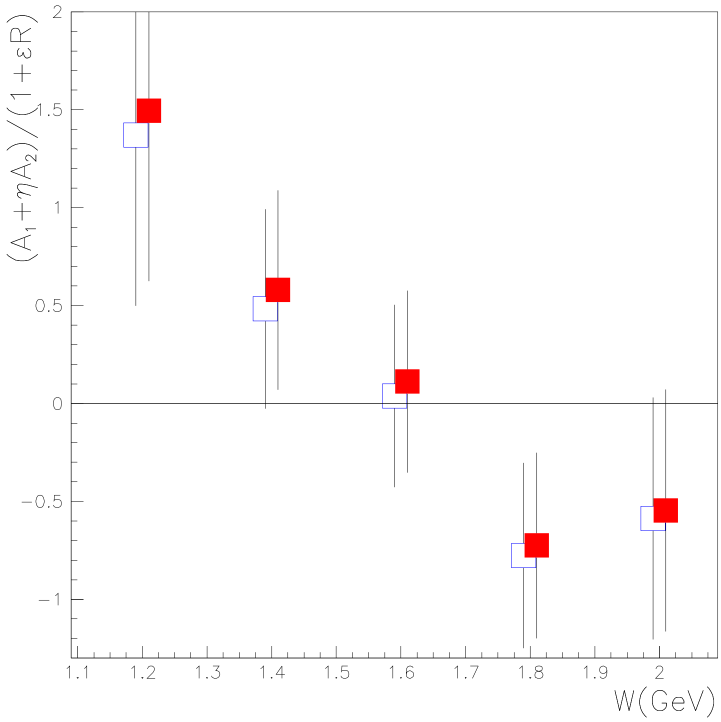

FIG. 51: Comparison of the $(A_1 + \eta A_2)/(1 + \epsilon R)$ for the Faraday Cup asymmetry 0.14% (empty squares) and 0.34% (full squares) on the 2.494 GeV outbending data. The systematic shift is small compared to the statistical errors.

TABLE XI: $(A_1 + \eta A_2)/(1 + \epsilon R)$ and systematic errors for 5 W bins (outbending data).

$< W >$ (GeV)	$(A_1 + \eta A_2)/$ $(1 + \epsilon R)$	MM cut	$P_e P_t$	fid. cuts	backgr. sub.	charge asym.	total
1.2	$+1.152 \pm 0.592$	0.20	0.265	0.23	0.0922	0.06	0.42
1.4	$+0.444 \pm 0.349$	0.01	0.102	0.09	0.0442	0.05	0.15
1.6	$+0.003 \pm 0.315$	0.08	0.001	0.08	0.0002	0.04	0.12
1.8	$+0.247 \pm 0.328$	0.15	0.058	0.05	0.0222	0.03	0.17
2.0	-0.288 ± 0.428	0.01	0.064	0.06	0.0461	0.13	0.16

CHAPTER 6

SUMMARY AND CONCLUSIONS

The primary goal of this work is the first measurement of the double spin asymmetry in π^- electro–production. The data have been collected in Hall B at Jefferson Lab during the EG1 run period using a polarized electron beam and a polarized ND_3 target. The polarized electron beam was polarized using a GaAs–cathode and the target was polarized at ~ 1 K in a 5 Tesla magnetic field using microwaves to enhance the polarization via Dynamic Nuclear Polarization. The nearly 4π CEBAF Large Acceptance Spectrometer (CLAS) was used for particle detection.

The EG1 experiment consists of two runs, EG1a and EG1b (also named EG2000 due to the year the data were collected). The results presented in the previous chapter were obtained by analyzing the data taken during the earlier run, EG1a. The data are available for ND_3 and carbon targets at a beam energy of 2.5 GeV and two different torus current settings 2250 and -1500 A providing a W range for inclusive electron scattering approximately from 0.8 GeV to 2.25 GeV. The negative torus polarity data set provides a lower Q^2 range than the positive polarity one. Results are presented in two Q^2 bins, 0.08 GeV^2 < Q^2 <0.4 GeV^2 and 0.4 GeV^2 < Q^2 <1.2 GeV^2. Data on a liquid helium target are also available for 2.5 GeV beam energy and 2250 A torus current which, together with the carbon, is used to subtract the background (nitrogen, helium and foils) from the ND_3 data. The reaction channel $\vec{e}\vec{d} \rightarrow e\pi^- pp$ is selected by detecting the scattered electron and the emitted pion, and using the missing mass technique, assuming that the target is a nucleon at rest. This channel is primarily sensitive to polarized neutrons in the target.

The asymmetry $(A_1+\eta A_2)/(1+\epsilon R)$ as a function of the invariant mass W has been extracted for two Q^2 bins. The results were integrated over the angular acceptance of the channel as well as for a narrower range in θ^* for which we have almost full ϕ^* coverage. The data have been compared to two phenomenological models, MAID and AO, whose predictions are based entirely on unpolarized data.

Despite the large uncertainties due to low statistics and poor deuteron polarization, the measured asymmetries are clearly non–zero, especially in the second resonance region. The asymmetries also illustrate a strong dependence on the invariant

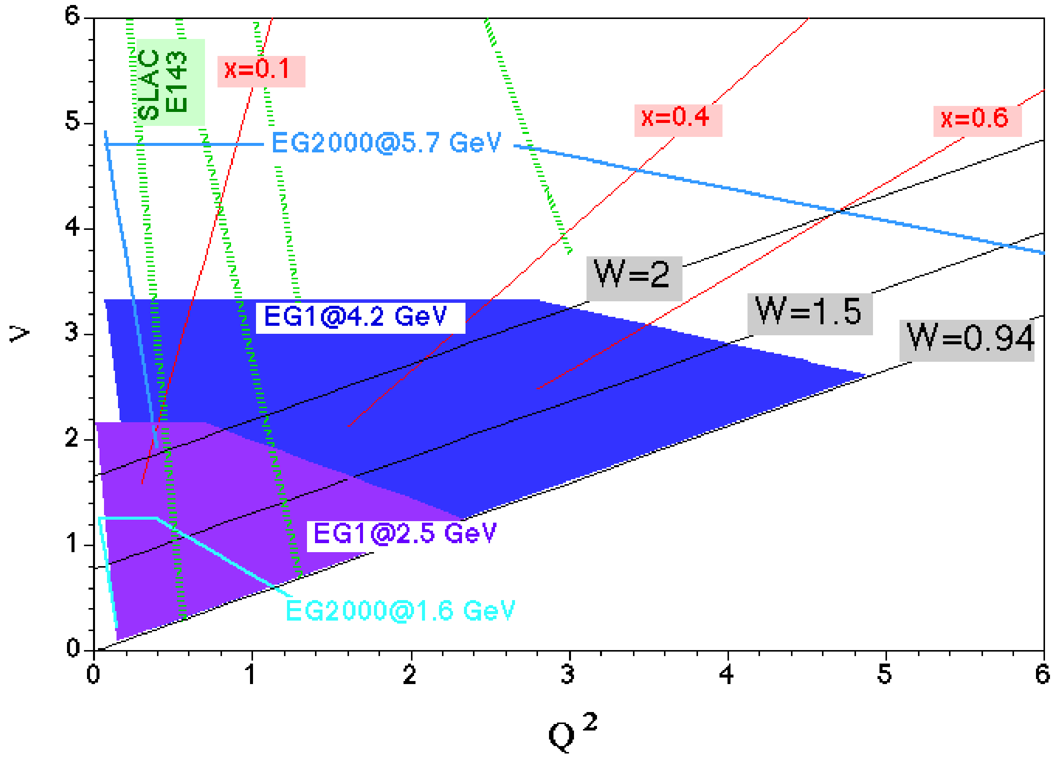

FIG. 52: The overall kinematical regions that are accessible with CLAS for the EG1 run period.

mass W, as well as the four–momentum transfer Q^2. The asymmetry in the second and the third resonance region is consistent with zero at low Q^2 but a non–zero asymmetry is clear at higher Q^2. Whereas the asymmetry as a function of W is mainly positive for the π^+ channel [68, 69], it changes sign from positive to negative at $W \sim 1.7$ GeV for the π^- channel. The results are in broad agreement with MAID and AO.

The presented results in the $\pi^- p$ channel and their comparison with model predictions give hope for a better understanding of the neutron resonances. Thanks to the increase in the amount of data and, more importantly, in the deuteron polarization, those resonances are expected to be studied in detail with the analysis of the EG2000 data, which will allow us to make a finer Q^2, W, and θ^* as well as ϕ^* bins. With these new data, it may also be possible to extract response functions and make a comparison with the π^+ channel. The kinematical regions accessible with CLAS for the EG2000 as well as the EG1a data are plotted in Fig. 52.

BIBLIOGRAPHY

[1] H. Yukawa, Proc. Phys. Math. Soc. Japan **17**, 48 (1935).

[2] C. M. G. Lattes *et al.*, Nature **159**, 694 (1947); **160**, 453 (1947).

[3] O. W. Greenberg, Am. J. Phys. **50**, 1074 (1982).

[4] O. W. Greenberg, Phys. Rev. Lett. **13**, 598 (1964).

[5] V. Burkert *et al.*, CEBAF proposal, PR–91–023.

[6] S. E. Kuhn *et al.*, CEBAF proposal, PR–93–009.

[7] R. Minehart *et al.*, CEBAF proposal, PR–93–036.

[8] D. Sober *et al.*, CEBAF proposal, PR–91–015.

[9] S. Weinberg, Phys. Lett. B **251**, 288 (1990); Nucl. Phys. **B363**, 3 (1991).

[10] C. Ordóñez and U. van Kolck, Phys. Lett. B **291**, 459 (1992).

[11] D. Drechsel, O. Hanstein, S. S. Kamalov and L. Tiator, Nucl. Phys. **A645**, 145 (1999).

[12] V. Burkert and Z. Li, Phys. Rev. D **47**, 46 (1993).

[13] W. T. Toner, *Lepton-hadron interactions, Proc. of the 4 th Int. Conf. on high energy collisions*, Oxford, (April 5–7, 1972).

[14] D. Drechsel and L. Tiator, J. Phys. G: Nucl. Part. Phys. **18**, 449 (1992).

[15] A. Bartl and W. Majerotto, Nucl. Phys. **B62**, 267 (1973).

[16] R. L. Walker, Phys. Rev. **182**, 1729 (1969).

[17] C. W. Akerlof *et al.*, Phys. Rev. Lett. **16**, 147 (1966); **163**, 1482 (1967).

[18] E. Amaldi, S. Fubini and G. Furlan, *Pion-Electroproduction, Electroproduction at Low Energy and Hadron Form Factors*, Springer-Verlag, Berlin Heidelberg, New York, (1979).

[19] S. E. Kuhn, *Nucleon Structure Functions: Experiments and Models.*

[20] T. W. Donnelly and A. S. Raskin, Ann. Phys. **169**, 247 (1986).

[21] A. S. Raskin and T. W. Donnelly, Ann. Phys. **191**, 78 (1989).

[22] W. Albrecht *et al.*, Nucl. Phys. **B25**, 1 (1970); **B27**, 615 (1971).

[23] R. Siddle *et al.*, Nucl. Phys. **B35**, 93 (1971).

[24] S. L. Glashow, Physica **96A**, 27 (1979).

[25] R. W. Lourie, *Workshop on Electron–Nucleon Scattering*, EIPC, Italy, (July 5–10, 1993).

[26] C. E. Carlson and J. L. Poor, Phys. Rev. D **38**, 2758 (1988).

[27] M. Warns, H. Schroeder, W. Pfeil and H. Rollnik, Z. Phys. C **45**, 627 (1990).

[28] S. A. Gogilidze, Y. S. Surovtsev and F. G. Tkebuchava, Sov. J. Nucl. Phys. **45**, 1085 (1987).

[29] J. G. Koerner, Z. Phys. C **33**, 529 (1987).

[30] R. C. E. Devenish and D. H. Lyth, Nucl. Phys. **B43**, 228 (1972).

[31] V. Burkert and R. Minehart, CEBAF proposal, PR–89–037/42.

[32] R. W. Lourie and S. Frullani, CEBAF proposal, PR–91–011.

[33] V. Burkert, *International Conference on the Structure of Baryons and Related Mesons*, Yale University, (June 1–4, 1992).

[34] R. Thompson *et al.*, Phys. Rev. Lett. **86**, 1702 (2001).

[35] V. Burkert, *Electro–production of Baryon Resonances above the* $\Delta(1232)$*, Topical Workshop on Excited Baryons*, (1988).

[36] L. A. Copley, G. Karl and E. Obryk, Phys. Lett. B **29**, 117 (1969).

[37] S. Capstick, Phys. Rev. D **46**, 2864 (1992).

[38] Zp. Li, V. Burkert and Zh. Li, Phys. Rev. D **46**, 70 (1992).

[39] R. Minehart, V. Burkert and M. Gai, CEBAF proposal, PR–89–038.

[40] S. Capstick, CEBAF preprint, CEBAF–TH–92–09 (1992).

[41] F. E. Close and F. J. Gilman, Phys. Lett. B **38**, 541 (1972).

[42] S. D. Ecklund and R. L. Walker, Phys. Rev. **159**, 1195 (1967).

[43] Particle Data Group, J. J. Hernandez *et al.*, Phys. Lett. B **239**, 1 (1990).

[44] S. Capstick, *Proceedings of the NSTAR2000 Workshop*, JLAB, (February 16–19, 2000).

[45] R. L. Crawford and W. T. Morton, Nucl. Phys. **B211**, 1 (1983).

[46] M. J. Alguard *et al.*, Phys. Rev. Lett. **37**, 1258 (1976); **37**, 1261 (1976).

[47] L. G. Levchuk, Nucl. Instr. and Meth. **A345**, 496 (1994).

[48] D. S. Carman *et al.*, Nucl. Instr. and Meth. **A419**, 315 (1998).

[49] M. D. Mestayer *et al.*, Nucl. Instr. and Meth. **A449**, 81 (2000).

[50] G. Adams *et al.*, Nucl. Instr. and Meth. **A465**, 414 (2001).

[51] M. Amarian *et al.*, Nucl. Instr. and Meth. **A460**, 460 (2001).

[52] M. Anghinolfi *et al.*, Nucl. Instr. and Meth. **A447**, 424 (1998).

[53] E. S. Smith *et al.*, Nucl. Instr. and Meth. **A432**, 265 (1999).

[54] V. Blobel *et al., The BOS System for CLAS detector: Dynamic Memory Management*, (November 27, 1995).

[55] A. Abragam *et al.*, Phys. Lett. **2**, 310 (1962).

[56] O. Chamberlain *et al.*, Phys. Lett. **7**, 293 (1963).

[57] D. G. Crabb and W. Meyer, Annu. Rev. Nucl. Part. Sci. **47**, 67 (1997).

[58] M. Borghini *et al.,* CERN Yellow Report **68–32**. (1968).

[59] D. G. Crabb, *Solid Polarized Targets: A Workshop Held at the Fall Meeting of the American Physical Society, Division of Nuclear Physics*, Virginia, (1994).

[60] G. R. Court *et al.*, Nucl. Instr. and Meth. **A324**, 433 (1993).

[61] M. Goldman, J. Magn. Res. **17**, 393 (1975).

[62] C. M. Dulya *et al.*, Nucl. Instr. and Meth. **A356**, 88 (1995).

[63] S. Stepanyan, *Simple Event Builder (SEB) in the Framework of RECSIS*, (1997).

[64] D. G. Crabb (private communication).

[65] S. E. Kuhn (private communication).

[66] T. Forest (private communication).

[67] G. E. Dodge (private communication).

[68] R. De Vita, Ph.D. thesis, INFN, Genova, (2000).

[69] R. De Vita *et al.*, Phys. Rev. Lett. **88**, 082001–1 (2002).

[70] S. E. Kuhn (private communication).

[71] S. E. Kuhn (private communication).

APPENDIX A

MULTIPOLE EXPANSION

The differential cross–section for pion electro–production in eq. [20] can also be written as

$$\frac{d\sigma}{d\Omega_\pi} = A + \epsilon B + \epsilon \mathrm{C}\sin^2\theta^*_\pi \cos 2\phi^*_\pi + \sqrt{\epsilon(1+\epsilon)}\mathrm{D}\sin\theta^*_\pi \cos\phi^*_\pi, \tag{83}$$

where A, B, C, and D are structure functions, depending on W, Q^2, and θ^* but not on ϕ^*. These functions can be expressed in terms of the amplitudes F_n

$$\begin{aligned}
A &= \frac{P_\pi}{\sqrt{Q^2}}\{[|F_1|^2 + |F_1+F_4|^2 + |F_2|^2 + |F_3+F_2|^2] \\
&\quad +\cos\theta^*[\mathcal{R}eF_3^*F_4 - 2\mathcal{R}eF_1^*F_2^*] \\
&\quad -\cos^2\theta^* \cdot \frac{1}{2}[|F_1+F_4|^2 - |F_1|^2 + |F_2+F_3|^2 - |F_2|^2 - \cos^3\theta^*\mathcal{R}eF_3^*F_4\}, \\
B &= \frac{P_\pi}{\sqrt{Q^2}}\frac{Q^2}{\nu^2}|F_5+F_6|^2, \\
C &= \frac{P_\pi}{\sqrt{Q^2}}\cos\theta^*\mathcal{R}eF_3^*F_4 + \{|F_1+F_4|^2 - |F_1|^2 + |F_2+F_3|^2 - |F_2|^2\}, \\
D &= \frac{P_\pi}{\sqrt{Q^2}}\frac{(Q^2)^{1/2}}{\nu}\{2\mathcal{R}e[F_5^*(F_1+F_4) + F_6^*(F_2+F_3)] + 2\cos\theta^*\mathcal{R}e(F_3F_5^* + F_4F_6^*)\}.
\end{aligned} \tag{84}$$

Electric, magnetic and longitudinal multipole amplitudes are indicated by $E_{l^\pm}$, $M_{l^\pm}$, and $L_{l^\pm}$, respectively. The subscripts $l^\pm$ represent the angular momentum l of the emitted pion and the total πN spin $j = |l \pm \frac{1}{2}|$. The invariant amplitudes F_n have the following multipole expansion in terms of the derivitives of the Legendre polynomials (P_l)

$$\begin{aligned}
F_1 &= \sum_0^\infty\{[lM_{1^+} + E_{1^+}]P'_{l+1} + [(l+1)M_{1^-} + E_{1^-}]P'_{l-1}\}, \\
F_2 &= \sum_1^\infty[(l+1)M_{1^+} + lM_{1^-}]P'_l, \\
F_3 &= \sum_1^\infty\{[(E_{1^+} - M_{1^+}]P''_{l+1} + [(E_{1^-} + M_{1^-}]P''_{l-1}\}, \\
F_4 &= \sum_2^\infty[(M_{1^+} - E_{1^+} - M_{1^-} - E_{1^-}]P''_l, \\
F_5 &= \sum_0^\infty[(l+1)L_{l^+}P'_{l+1} - lL_{l^-}P'_{l-1}],
\end{aligned} \tag{85}$$

$$F_6 = \sum_1^\infty [lL_{l^-} - (l+1)L_{l^+}]P_l'.$$

From the equations above one can see that E_0^-, E_1^-, M_0^+, M_0^- and L_0^- do not show up in the expressions. Therefore, they are not physical.

APPENDIX B

NUMBERS

TABLE XII: The cross section ratio σ_n/σ_p for various $< Q^2 >$ and W^2 values.

$< Q^2 >$ (GeV^2)	W^2 (GeV^2)	Z
0.76	1.56	0.85
0.77	1.82	0.76
0.78	2.10	0.88
0.78	2.40	0.89
0.79	2.72	0.70
0.75	3.06	0.79
0.73	3.42	0.80
0.68	3.80	0.79
0.59	4.20	0.82
0.49	4.62	0.85

TABLE XIII: The ND_3 target thickness for 10 W bins above the elastic peak.

$< W >$ (GeV)	ND_3 Target Thickness (cm)
1.25	0.613
1.35	0.569
1.45	0.574
1.55	0.585
1.65	0.585
1.75	0.589
1.85	0.589
1.95	0.592
2.05	0.594
2.15	0.570

TABLE XIV: List and characteristics of the materials in the beamline.

Description	Location	Material	Thickness
Crystat entrance window	-120.5	Al	71 μm
Crystat heat shield	-81.5	Al	10 μm
Banjo entrance window	-55.75	Al	71 μm
Upstream space between banjo and target entrance window	-55.625	LHe	0.25 cm
Target entrance window	-55.5	Al	25 μm
Target material	-55.0	NH_3, NH_3 C, LHe	1 cm
Target exit window	-54.5	Kapton	50 μm
Upstream space between target and banjo exit window	-54.375	Al	0.25 cm
Banjo exit window	-54.25	Al	71 μm
4 K shield	-46	Al	20 μm
Radiation shield	-36.0	Al	20 μm
Space blanket	-35.0	Al–Mylar-Cerex	12 sheets
OVC exit window	-30.6	Al	71 μm

TABLE XV: Dilution factors and measured $\vec{e}\vec{d}$ elastic asymmetries as a function of Q^2 and W for 2.565 GeV inbending data set.

$< Q^2 >$ (GeV^2)	$< W >$ (GeV)	A_{meas}	Dilution Factor
0.4	0.87	0.0008±0.0032	0.088±0.033
	0.89	-0.0076±0.0026	0.157±0.025
	0.91	-0.0061±0.0022	0.241±0.018
	0.93	-0.0098±0.0019	0.314±0.014
	0.95	-0.0075±0.0019	0.301±0.013
	0.97	-0.0088±0.0019	0.230±0.015
	0.99	-0.0037±0.0020	0.174±0.017
	1.01	-0.0006±0.0021	0.168±0.018
0.64	0.87	-0.0065±0.0028	0.113±0.042
	0.89	-0.0009±0.0025	0.178±0.031
	0.91	-0.0108±0.0022	0.250±0.023
	0.93	-0.0094±0.0020	0.298±0.018
	0.95	-0.0076±0.0020	0.282±0.016
	0.97	-0.0079±0.0021	0.225±0.016
	0.99	-0.0049±0.0021	0.171±0.018
	1.01	-0.0007±0.0022	0.148±0.021
1.1	0.87	-0.0056±0.0054	0.173±0.233
	0.89	-0.0147±0.0050	0.222±0.185
	0.91	-0.0166±0.0046	0.265±0.147
	0.93	-0.0207±0.0044	0.280±0.119
	0.95	-0.0152±0.0043	0.263±0.100
	0.97	-0.0707±0.0043	0.220±0.086
	0.99	-0.0061±0.0044	0.167±0.077
	1.01	-0.0102±0.0044	0.132±0.071

TABLE XVI: Dilution factors and measured $\vec{e}\vec{d}$ elastic asymmetries as a function of Q^2 and W for 2.494 GeV inbending data set.

$< Q^2 >$ (GeV^2)	$< W >$ (GeV)	A_{meas}	Dilution Factor
0.4	0.87	0.0026±0.0026	0.074±0.0411
	0.89	-0.0036±0.0022	0.143±0.0307
	0.91	-0.0019±0.0018	0.229±0.0225
	0.93	-0.0050±0.0016	0.291±0.0176
	0.95	-0.0069±0.0016	0.274±0.0168
	0.97	-0.0041±0.0016	0.194±0.0189
	0.99	-0.0031±0.0017	0.136±0.0215
	1.01	-0.0023±0.0018	0.134±0.0233
0.64	0.87	-0.0030±0.0024	0.125 ±0.0477
	0.89	-0.0044±0.0021	0.192 ±0.0358
	0.91	-0.0059±0.0019	0.263 ±0.0265
	0.93	-0.0066±0.0017	0.307 ±0.0205
	0.95	-0.0083±0.0017	0.292 ±0.0182
	0.97	-0.0059±0.0017	0.241 ±0.0186
	0.99	-0.0042±0.0018	0.189 ±0.0207
	1.01	-0.0039±0.0018	0.165 ±0.0235
1.1	0.87	-0.0022±0.0045	0.173±0.2743
	0.89	-0.0092±0.0042	0.222±0.2187
	0.91	-0.0087±0.0039	0.262±0.1736
	0.93	-0.0115±0.0037	0.280±0.1402
	0.95	-0.0093±0.0037	0.255±0.1187
	0.97	-0.0096±0.0037	0.220±0.1015
	0.99	-0.0018±0.0037	0.179±0.0888
	1.01	-0.0025±0.0038	0.137±0.0836

TABLE XVII: Dilution factors and measured $\vec{e}\vec{d}$ elastic asymmetries as a function of Q^2 and W for 2.562 GeV outbending data set.

$< Q^2 >$ (GeV^2)	$< W >$ (GeV)	A_{meas}	Dilution Factor
0.1545	0.87	-0.0056±0.0088	0.218±0.0116
	0.89	-0.0050±0.0074	0.256±0.0077
	0.91	-0.0046±0.0063	0.281±0.0054
	0.93	-0.0025±0.0057	0.327±0.0039
	0.95	-0.0022±0.0057	0.271±0.0038
	0.97	-0.0081±0.0058	0.196±0.0045
	0.99	-0.0078±0.0062	0.200±0.0053
	1.01	-0.0104±0.0065	0.304±0.0058
0.2423	0.87	-0.0011±0.0060	0.138 ±0.0156
	0.89	-0.0031±0.0048	0.185 ±0.0111
	0.91	-0.0101±0.0039	0.262 ±0.0077
	0.93	-0.0043±0.0035	0.304 ±0.0060
	0.95	-0.0052±0.0034	0.252 ±0.0062
	0.97	-0.0009±0.0036	0.175 ±0.0071
	0.99	-0.0027±0.0039	0.150 ±0.0081
	1.01	-0.0065±0.0042	0.195 ±0.0089
0.3442	0.87	-0.0056±0.0088	0.144±0.0212
	0.89	-0.0150±0.0074	0.184±0.0163
	0.91	-0.0046±0.0063	0.250±0.0123
	0.93	-0.0025±0.0057	0.283±0.0101
	0.95	-0.0022±0.0057	0.244±0.0102
	0.97	-0.0081±0.0058	0.190±0.0111
	0.99	-0.0078±0.0062	0.145±0.0127
	1.01	-0.0104±0.0065	0.171±0.0135

TABLE XVIII: Dilution factors and measured $\vec{e}\vec{d}$ elastic asymmetries as a function of Q^2 and W for 2.494 GeV outbending data set.

$< Q^2 >$ (GeV^2)	$< W >$ (GeV)	A_{meas}	Dilution Factor
0.3442	0.87	-0.00442±0.00274	0.187±0.017
	0.89	0.00318±0.00221	0.221±0.013
	0.91	-0.00024±0.00186	0.270±0.010
	0.93	0.00388±0.00171	0.254±0.010
	0.95	-0.00013±0.00174	0.152±0.011
	0.97	0.00317±0.00186	0.050±0.013
	0.99	0.00089±0.00200	0.006±0.050
	1.01	-0.00011±0.00216	0.060±0.015

TABLE XIX: Counts to extract $(A_1 + \eta A_2)/(1 + \epsilon R)$ for the inbending 2.565 GeV data set (Normalization constant $f = 10.32$ and $P_eP_t = -0.154 \pm 0.013$).

W (GeV)	$N^+/$ acc	$N^-/$ acc	$N_C/$ acc	$N_{He}/$ acc
1.2	38803	38975	5408	2520
1.4	70750	74484	10475	4853
1.6	56173	57199	8464	4235
1.8	25235	24437	3705	1801
2.0	5478	5155	781	286
$N^+/$ acc^2	$N^-/$ acc^2	$N_C/$ acc^2	$N_{He}/$ acc^2	$(A_1 + \eta A_2)/$ $(1 + \epsilon R)$
199593	200085	27624	12371	-0.0442±0.436
336550	354549	49728	20933	0.9991±0.257
239273	244149	35486	17609	0.2162±0.220
99703	96422	13946	6846	-0.5518±0.261
22386	20020	3231	1051	-0.8471±0.514

TABLE XX: Counts to extract $(A_1+\eta A_2)/(1+\epsilon R)$ for the inbending 2.494 GeV data set ($P_e P_t = 0.1074 \pm 0.011$).

W (GeV)	N^+/ acc	N^-/ acc	N^+/ acc^2	N^-/ acc^2	$(A_1+\eta A_2)/(1+\epsilon R)$
1.2	17964	18119	90216	89964	-0.0015±0.5269
1.4	27144	27469	124685	122873	0.353±0.3085
1.6	20344	19936	82783	81290	0.792±0.2733
1.8	8566	8955	32114	34861	-0.1055±0.3314
2.0	1600	1649	5851	6184	-0.188±0.7099

TABLE XXI: Counts to extract $(A_1+\eta A_2)/(1+\epsilon R)$ for the outbending 2.562 GeV data set ($P_e P_t = -0.18 \pm 0.048$).

W (GeV)	N^+/ acc	N^-/ acc	N^+/ acc^2	N^-/ acc^2	$(A_1+\eta A_2)/(1+\epsilon R)$
1.2	11388	11885	34562	36182	1.4003±0.8165
1.4	19522	19974	55393	57260	0.5435±0.4759
1.6	1250	12612	33444	33763	0.102 ±0.4270
1.8	6013	5767	15569	14874	-0.6778±0.4429
2.0	2043	1963	4972	4779	-0.4913±0.5558

TABLE XXII: Counts to extract $(A_1+\eta A_2)/(1+\epsilon R)$ for the outbending 2.494 GeV data set ($P_e P_t = 0.088 \pm 0.042$).

W (GeV)	N^+/ acc	N^-/ acc	N^+/ acc^2	N^-/ acc^2	$(A_1+\eta A_2)/(1+\epsilon R)$
1.2	41654	41480	124270	124040	0.8754±0.8604
1.4	65837	65978	184865	184308	0.3281±0.5153
1.6	41046	41491	108063	109254	-0.1151 ±0.4659
1.8	19571	18846	49915	48216	1.367±0.4872
2.0	5496	55383	13214	13241	0.0071±0.6700

VITA

Mehmet Bektasoglu
Department of Physics
Old Dominion University
Norfolk, VA 23529

Mehmet Bektasoglu (born in Bingol), from Istanbul, Turkey, graduated from Umraniye High School, in 1986. He graduated from the Physics Department of Yildiz Technical University, in 1993, and received a scholarship from the Turkish Ministry of Education to pursue his graduate education in the USA, in 1994. He was accepted by the Physics Department at Old Dominion University in Fall 1995, and received his Master's degree in Physics in May 1997. He collected his thesis data in Hall B of Thomas Jefferson National Accelerator Facility, in the Fall of 1998, and defended his thesis in March 2002. His recent publications are:

1. "*First Measurement of the Double Spin Asymmetry in $\vec{e}\vec{p} \to e'\pi^+ n$ in the Resonance Region*," R. De Vita *et al.,* (The CLAS Collaboration), Phys. Rev. Lett. **88**, 082001 (2002).
2. "*Q^2 Dependence of Quadrupole Strength in the $\gamma^* p \to \Delta^+(1232) \to p\pi^0$ Transition,*" K. Joo *et al.,* (The CLAS Collaboration), Phys. Rev. Lett. **88**, 12001 (2002).
3. "*Observation of Exclusive Deeply Virtual Compton Scattering in Polarized Electron Beam Asymmetry Measurements,*" S. Stepanyan *et al.,* (The CLAS Collaboration), Phys. Rev. Lett. **87**, 182002 (2001).
4. "*Photoproduction of the ρ^0 meson on the Proton at Large Momentum Transfer,*" M. Battaglieri *et al.,* (The CLAS Collaboration), Phys. Rev. Lett. **87**, 172002 (2001).
5. "*Electroproduction of the* $\Lambda(1520)$ *Hyperon,*" S. Barrow *et al.,* (The CLAS Collaboration), Phys. Rev. C **64**, 044601 (2001).
6. "*Exclusive electroproduction of ϕ mesons at 4.2 GeV,*" K. Lukashin *et al.,* (The CLAS Collaboration), Phys. Rev. C **63**, 065205-1 (2001).
7. "*$ep \to e'p\eta$ Reaction at and above the* $S_{11}(1535)$ *Baryon Resonance*," R. Thompson *et al.,* (The CLAS Collaboration), Phys. Rev. Lett. **86**, 1702 (2001).

Typeset using LaTeX.